Retrograde Transport of Golgi Enzymes by GOLPH3 Across Maturing *Cisternae* Regulates Glycan Assembly on Sphingolipids and Cell Growth

Riccardo Rizzo[1]*, Domenico Russo[1,#], Kazuo Kurokawa[2,#], Pranoy Sahu[1], Bernadette Lombardi[1], Domenico Supino[1], Mikhail Zhukovsky[1], Anthony Vocat[3], Prathyush Pothukuchi[1], Vidya Kunnathully[1], Laura Capolupo[3], Gaelle Boncompain[4], Carlo Vitagliano[5], Federica Zito Marino[5], Gabriella Aquino[5], Petra Henklein[6], Luigi Mandrich[1], Gerardo Botti[5], Henrik Clausen[7], Ulla Mandel[7], Toshiyuki Yamaji[8], Kentaro Hanada[8], Alfredo Budillon[5], Franck Perez[4], Seetharaman Parashuraman[1], Yusuf A Hannun[9], Akihiko Nakano[2], Giovanni D'Angelo[1,3*$] and Alberto Luini[1*$]

[1]*Institute of Biochemistry and Cell Biology National Research Council, Via P. Castellino 111, Naples, Italy.*
[2]*Live Cell Super-Resolution Imaging Research Team, RIKEN Center for Advanced Photonics, Saitama, 3510198, Japan.*
[3]*École Polytechnique Fédérale de Lausanne (EPFL), AI 1109, Station 19, CH-1015 Lausanne, Switzerland.*
[4]*Institute Curie – CNRS UMR1 44, Research Center, Paris, France.*
[5]*Istituto Nazionale Tumori G. Pascale, via Mariano Semmola, Naples, Italy.*
[6]*Universitätsmedizin Berlin Institut für Biochemie Charité CrossOver Charitéplatz 1 / Sitz: Virchowweg 610117 Berlin, Germany.*
[7]*University of Copenhagen, Faculty of Health Sciences, Centre for Glycomics, Department of Cellular and Molecular Medicine Nørre Alle 20, DK-2200 Copenhagen N, Denmark.*
[8]*Department of Biochemistry & Cell Biology National Institute of Infectious Diseases 1-23-1 Toyama, Shinjuku-ku, Tokyo, Japan.*
[9]*Stony Brook University Medical Center, Stony Brook 11794-8430, New York, United States.*

[#]These authors contributed equally

[$]These authors contributed equally

*Correspondence: a.luini@ibp.cnr.it, r.rizzo@ibp.cnr.it, giovanni.dangelo@epfl.ch

Abstract:

We have investigated how glycans, ubiquitous polysaccharides endowed with major biological functions, are assembled by glyco-enzymes on cargo proteins/ lipids during their transport through the Golgi complex. We have manipulated glyco-enzymes retrotransport, a core process in intra-Golgi trafficking, through controlled alterations of the levels of GOLPH3, a coatomer adaptor that drives the retrograde movement of glyco-enzymes and shows oncogenic properties in humans, and examined glycan assembly. We find that: a) GOLPH3 is part of the cisternal maturation mechanism, yet it specifically binds and sorts for recycling a subset of enzymes involved in glycan assembly on sphingolipids, while other enzymes recycle independently of GOLPH3. This indicates that cisternal maturation is an ensemble of enzyme-recycling modules; b) GOLPH3 increases the levels of its client enzymes via a regulated-degradation mechanism based on delaying their escape from the Golgi into the lysosomes; and, c) by changing the levels of key enzymes, GOLPH3 alters the glycan patterns assembled on sphingolipids, to produce more proliferation-inducing glycosphingolipid metabolites. These findings unravel organizing principles of intra-Golgi traffic and of glycan assembly that might have general applicability and broad pathophysiological implications, and outline a novel mechanism for GOLPH3-induced proliferation based on glycosphingolipid biosynthesis.

Introduction:

A major unsolved question at the intersection between the fields of glycobiology and intracellular membrane transport is how glycans are assembled on their protein and lipid scaffolds during traffic through the Golgi complex. Glycans (ubiquitous polymers of covalently linked sugars) represent a significant fraction of the body weight, influence basic cellular activities including adhesion, motility, signaling, and differentiation (*1-3*) and play major roles in human diseases including cancer (*4-6*). It is thus important for both biology and medicine to understand the mechanisms of glycan assembly, or glycosylation.

Golgi glycosylation results from multiple reactions catalyzed in orderly sequences by sugar-transferring enzymes, or glyco-enzymes, (glycosyltransferases and glycosidases) that act on protein/ lipid substrates in the lumen of Golgi *cisternae* (*5, 7*). Glycosylation is a non-templated process that depends on a constellation of factors [see Parashuraman *et al*. for a recent review (*8*)], two of which play central roles. One is the catalytic properties and the expression levels of glyco-enzymes and of accessory proteins including sugar and ion transporters (*8, 9*). The other is the Golgi traffic machinery that controls the intra-Golgi dynamics, and hence the order and frequency of the encounters of enzymes with cargo substrates within the Golgi *cisternae* that function as reaction chambers (*8, 10*). Glycobiology has made enormous progress in the analysis of the transcription of glyco-enzymes and of its effects on glycan structure and function (*1*). In contrast, the transport mechanisms that control glyco-enzyme and cargo dynamics in the Golgi remain poorly understood, hindering our comprehension of the principles of glycome assembly. It is now necessary to clarify the role of Golgi transport in glycosylation by exploiting the available knowledge on the organization of intra-Golgi trafficking.

The Golgi comprises 3 to 5 stacked *cisternae* (*cis*, medial and *trans*) that contain numerous glyco-enzymes (about 200 are encoded in the mammalian genome) distributed in a *cis-trans* order that roughly reflects the sequences of the glycan assembly reactions (*5*). Transport through the *cisternae* relies on multiple mechanisms, including formation of transport vesicles, (*11*) inter-cisternal continuities, (*12, 13*) and enzyme/ cargo partitioning between lipid phases (*14*). In addition, it depends on a specific traffic configuration, called cisternal progression-maturation, now accepted to be a major mode of intra-Golgi transport (*15-17*). Cisternal maturation operates as follows: secretory cargo reaches the Golgi from the endoplasmic reticulum (ER) within membranous carriers that fuse to form new *cisternae* at the *cis* Golgi face and then gradually change composition ('mature') through retrotransport of glyco-enzymes via coatomer protein complex I (COPI) coated vesicles, effectively 'converting' into medial and *trans cisternae*. Meanwhile, cargoes remain in the lumen of *cisternae*, which finally disassemble at the trans Golgi Network (TGN) into post-Golgi carriers. Repetition of this process generates an anterograde flow of cargo-containing membranes towards various cellular destinations,

which is accompanied by, and synchronized with, a retrograde flow of Golgi enzymes that maintains the compositional homeostasis of the progressing *cisternae*. In this context, cargo is sequentially intercepted by glyco-enzymes for glycan assembly.

The molecular machinery driving cisternal maturation is partially understood. Potential components include the COPI coat (*18, 19*) fission and fusion factors (*20*), vesicle tethers (*21, 22*), membrane recruiting factors (*23*), regulatory GTPases and accessory proteins (*24-26*), and adapters that sort enzymes into nascent COPI vesicles (*27-30*). Among these factors, however, only a few (e.g., the COPI budding machinery and Rab GTPases) have been formally shown to be involved in cisternal maturation (*19, 31*).

To analyze how Golgi traffic impacts glycosylation, we have manipulated the retrotransport of the glyco-enzymes by altering the levels of GOLPH3, a well-characterized COPI adaptor that mediates enzyme recycling (*27, 28, 32, 33*). The role of GOLPH3 in enzyme recycling was first demonstrated in yeast by Banfield and Burd and their colleagues (*27, 28*) and later proposed to be conserved in other organisms including mammals (*32-36*). The GOLPH3 yeast homologue (Vps74p) binds to *trans* Golgi membranes in a phosphatidylinositol-4-phosphate [PtdIns(4)*P*] dependent manner and interacts with a specific motif in the cytosolic tail of a group of Golgi enzymes (Vps74p clients) as well as with the COPI coatomer (*27-30, 37, 38*). This results in the incorporation of Vps74p clients into COPI recycling vesicles and in their retrograde transport within the secretory pathway (*27*). Importantly, the *GOLPH3* gene is amplified in human solid tumors and GOLPH3 stimulates mitogenic signaling and cell proliferation, acting as an oncogene (*39*). GOLPH3, therefore, offers the opportunity to explore the links between glyco-enzyme dynamics, glycan processing and associated biological functions, in this case cell proliferation.

We find that a) GOLPH3 binds and retrotransports a subset of *trans*-Golgi enzymes (GOLPH3 clients) involved in the assembly of glycans on sphingolipids, i.e., in glycosphingolipid (GSL) synthesis, by acting as an integral component of the cisternal maturation mechanism. Other *trans*-Golgi enzymes are recycled independently of GOLPH3, indicating that cisternal maturation is an ensemble of recycling enzymatic modules. b) GOLPH3 increases the levels of its clients via a degradation-mediated mechanism based on delaying their escape from the Golgi into the lysosomes. c) By changing the levels of these enzymes that occupy key positions both in the common axis and at the branchpoint between GSL synthetic pathways, GOLPH3 alters the patterns of glycans assembled on sphingolipids. This reprograms the GSL synthetic module to produce growth-inducing glycosphingolipid, which results in excessive cell proliferation. Importantly, clinical data suggest that this mechanism operates in tumors from human patients.

These findings unravel organizing principles of intra-Golgi traffic and of Golgi-dependent glycan assembly that are probably applicable to other glycosylation pathways and thus may help to delineate a general program to unravel the regulation of glycan assembly by the Golgi transport mechanisms. Moreover, they have broad pathophysiological and medical implications as they outline a novel mechanism of action for GOLPH3-induced proliferation based on GSL biosynthesis.

Results:

GOLPH3 binds a set of enzymes of the glycosphingolipid biosynthetic pathway at their cytosolic tails

We first sought to identify mammalian glyco-enzymes that bind GOLPH3. The yeast GOLPH3 homologue Vps74p binds the consensus sequence F/L-L/I/V-x-x-R/K in the cytosolic tails of yeast enzymes (*27*). Since mammalian GOLPH3 can partially replace Vps74p in yeast (*27*), we searched for mammalian enzymes bearing a similar motif in their cytosolic tails. The three direct mammalian GOLPH3 clients [i.e., ST6GAL1 (*32*), PomGNT1 (*35*); and GCNT1 (*34*)] lack the full yeast motif but bear a similar sequence in their tails where the first hydrophobic amino acid is not present and the second is consistently a leucine (i.e., L-X-X-R/K, for brevity here referred to as **LxxR**) (**Figure S1A**). We looked for the LxxR sequence in the whole repertoire of human type II transmembrane Golgi glyco-enzymes and found it in 48 tails. Among these, the enzymes of the GSL biosynthetic pathway are the most represented (with 19 enzymes, accounting for 40% of the entire GSL pathway) followed by the proteoglycan synthetic enzymes and by a small group of O-glycosylation and N-glycosylation enzymes (**Figure S1A**).

In a parallel approach we overexpressed GOLPH3 (GOLPH3 OE) in HeLa cells and used a panel of lectins to detect changes in specific glycan patterns by cytofluorimetry. As shown in **Figure S1B**, GOLPH3 OE had marginal effects both on the binding of lectins that recognize different aspects of O- and N-linked glycans and on glycosaminoglycan production (**Figure S1C**) while it substantially increased the binding of Shiga toxin 1a B subunit (ShTxB) to the HeLa cell surface. Since ShTxB specifically binds to Gal-a1,4-Gal-b1,4-Glc trisaccharide in the context of the globo-series GSL Gb3 (*40*), its increased binding indicates augmented Gb3 levels at the cell surface.

Prompted by these convergent indications, we tested whether the LxxR motif mediates the binding of GSL enzymes to GOLPH3 using biotinylated peptides corresponding to their cytosolic tails in co-precipitation experiments (**Figure1A**). We found that tail peptides devoid of the LxxR motif (i.e., those of the GSL synthetic enzyme Lc3 Synthase [Lc3S; *B3GNT5*]; as well of GalT1 [*B4GALT1*]) did not interact with GOLPH3 either from cell lysates or as a recombinant purified protein. The LxxR-bearing tails gave instead mixed results. The tails of lactosyceramide synthase (LCS; *B4GALT5*), Gb3 synthase (Gb3S; *A4GALT*) and GD3 synthase (GD3S; *ST8SIA1*) co-precipitated GOLPH3 efficiently, instead, other two LxxR-containing enzymes, i.e., GM3

synthase (GM3S; *ST3GAL5*) and GM2/GM2 synthase (GA2/GM2S; *B4GALNT1*) (**Figure 1A**) did not. These data suggest that the LxxR motif is probably involved in a direct interaction with GOLPH3, but it might require additional components for efficient binding.

To identify the full GOLPH3 binding motif, we focused on LCS (the best binder in the above co-precipitation assays that we also confirm to co-immunoprecipitate GOLPH3 when expressed as a full-length protein in HeLa cells) (**Figure 1A** and **Figure S1D**). We determined the binding parameters of recombinant GOLPH3 to LCS tail by isothermal titration calorimetry (ITC) (*41*) and found a binding signature compatible with an enthalpy driven interaction, suggesting that LCS tail binds GOLPH3 via electrostatic attraction and/ or hydrogen bonding (**Figure 1B**). LCS tail contains six charged residues (arginines) distributed in two clusters, one that overlaps with the LxxR while the other is located 4 residues upstream this motif. We mutated the LCS tail at these two regions and tested the binding of the mutant tails to GOLPH3 (**Figure 1C** and **Figure 1D**) in pull down and ITC experiments. Mutations in the LxxR motif inhibited, and mutations in the upstream charged stretch abolished GOLPH3 binding, indicating that GOLPH3 requires both the regions in the LCS tail for efficient binding.

We next tested whether this dual motif in LCS tail functions as a Golgi-retention signal, by expressing in Hela cells a chimeric protein comprising the LCS cytosolic tails at the C-terminus of the transmembrane domain of sucrose isomaltase (SI), a type 2 integral plasma membrane protein, fused with GFP at the N-terminus (*29*). Since this construct does not have Golgi retention signals in its transmembrane and luminal domains, its Golgi retention could be ascribed exclusively to the enzyme tail (*29*). Wild type LCS tail efficiently retained the SI construct at the Golgi, whereas mutating either the LxxR or the upstream motif resulted in loss of Golgi retention (**Figure 1E**) indicating that the dual GOLPH3 binding motif in the LCS acts as a Golgi retention signal. Finally, we re-examined the cytosolic tails found by us or others to interact with GOLPH3 and noticed that they all exhibited at least one positive charge 2-5 aa upstream of the LxxR motif (i.e., [+]-$x_{(2-5)}$-LxxR). We then searched for all of the mammalian glyco-enzymes containing the [+]-$x_{(2-5)}$-LxxR dual motif and found that 22 bear it (**Figure S1E**), of which 9 belong to the GSL synthetic pathway (making GSL glyco-enzymes the most prevalent group) (**Figure S1E-F**).

These results, together with literature data, suggest that GOLPH3 binds the cytosolic tails of glyco-enzymes that contain a specific binding motif (i.e., the [+]-$x_{(2-5)}$-LxxR) and that the [+]-$x_{(2-5)}$-LxxR is necessary and sufficient to mediate Golgi retention. The [+]-$x_{(2-5)}$-LxxR is prevalent among GSL metabolic enzymes (**Figure S1A**) and the lectin binding experiment indicate that GOLPH3 affects GSL metabolism. Moreover, GSLs have demonstrated roles in regulating cell growth, thus in the rest of this study we focus on the GSL synthetic enzymes, although we do not exclude that other [+]-$x_{(2-5)}$-LxxR bearing enzymes might have a role in the biological effects of GOLPH3.

GOLPH3 retains its client enzymes in the Golgi by acting as a component of the cisternal maturation machinery

GOLPH3 can retain its clients in the Golgi either by recycling them in the process of the cisternal maturation, or, alternatively, by 'salvaging' enzymes that occasionally escape the stack through a mechanism similar to that of the KDEL receptor in retrieving escaped ER chaperones back to the ER (*42*). To distinguish between the two alternatives, which entail different consequences, we focused on a key feature of cisternal maturation, namely, the fact that Golgi enzymes must recycle in synchrony with the forward progression of cargo containing *cisternae* to maintain the compositional homeostasis of the Golgi compartments. We thus designed experiments to verify whether or not GOLPH3 operates in accord with this principle of synchrony, using both mammalian and yeast cells.

For experiments in mammalian cells, we examined the trafficking of the GOLPH3 client LCS, both by itself and compared to that of the cargo reporter Vesicular Stomatitis Virus G glycoprotein (VSV-G) in the presence or absence of GOLPH3. VSV-G is a well-characterized cargo reporter that traverses the Golgi at the same rate as procollagen by cisternal maturation (*43*). If GOLPH3 is a component of the cisternal maturation machinery, i.e., if it is responsible for the recycling of LCS coupled to the progression of the Golgi *cisternae*, its ablation will result in LCS not being recycled in synchrony with cisternal progression, and in it moving to the TGN at the rate of cisternal progression as defined by VSV-G. In contrast, if GOLPH3 drives a salvage mechanism, its ablation will cause a slow LCS leakage to the TGN, out of synchrony with VSV-G transport.

These experiments require the synchronization of LCS transport through the Golgi compartments. To this aim, we used a bi-cistronic LCS-GFP /KDEL-hook encoding plasmid (LCS-GFP_RUSH; see **Methods** for a detailed description) (*44*), that can be arrested and accumulated in the ER and then released from the ER synchronously by adding a suitable ligand (*44*); and to synchronize VSV-G for comparison experiments, we exploited a ts045-VSVG mutant that can be accumulated in the ER at 40 C and then released from the ER by shifting the temperature to 32 C (*45*) (see **Methods** for details). To monitor traffic through the Golgi, we took advantage of the nocodazole-induced ministacks system that affords a reliable visualization of the Golgi sub-compartments by light microscopy and of the line scanning technique for quantification (*46, 47*). The *cis*-Golgi and the TGN were identified by GM130 and TGN46 staining, respectively, in immuno-fluorescence (IF) experiments.

Using this system, we first characterized the progression across the Golgi of LCS-GFP_RUSH by itself. In control cells, LCS-GFP_RUSH moved from cis to *trans*-Golgi in less than 20 min and then remained in the *trans*-Golgi, without reaching the TGN for up to 2 hours, as expected. Instead, in GOLPH3-KD cells, LCS traversed the Golgi and reached the TGN in less than 20 min, a rate typical of cargo transport by cisternal maturation (*43*) (**Figure 2A**). Cryo-immuno-electron

microscopy (Cryo-IEM) confirmed that in control cells LCS progresses from *cis* to medial and then *trans cisterna* in about 10 min (**Figure 2B-D**). Moreover, it showed that, during progression form the *cis* to the *trans cisternae* (first 10 min) LCS is excluded from peri-Golgi vesicles, while, after reaching the *trans cisterna*, where it is retained, it efficiently enters these vesicles (**Figure 2D-E**). This is consistent with a model where LCS is retained in the *trans cisterna* by recycling backward via COPI vesicles. In GOLPH3-KD cells, instead, LCS was not retained in the *trans cisterna* and reached the TGN in 20 min, in agreement with the IF data; moreover, it was never detected in peri-Golgi vesicles (**Figure 2E**). As a control we examined the localization of GalT1, a trans-Golgi enzyme that does not bind GOLPH3, in cells transfected with the LCS-GFP_RUSH construct. Both in the presence and in the absence of GOLPH3, GalT1 remained unperturbed in the *trans cisterna*. This, together with further evidence provided below, supports the selectivity of the GOLPH3 depletion treatment on LCS trafficking (**Figure S2A**).

Next, we co-expressed and co-synchronized LCS-GFP_RUSH and VSV-G and monitored the progression of these proteins through the stack in the same cells. In control cells, LCS-GFP_RUSH and VSV-G entered and moved through the *cis/medial* Golgi compartments together; however, LCS-GFP_RUSH was retained in the *trans*-Golgi, while VSV-G crossed the Golgi and reached the TGN in 20 min (**Figure 2F**). Instead, in GOLPH3-KD cells, LCS-GFP_RUSH lost completely its property to be retained in the *trans*-Golgi and reached the TGN together with VSV-G (**Figure 2F**), again indicating that the Golgi retention of LCS requires GOLPH3.

We also examined the effect of GOLPH3 OE or GOLPH3 KD on the intra-Golgi distribution of LCS-HA at steady state. As shown in **Figure S2B**, in control cells, LCS-HA displayed a clear concentration at the *trans*-Golgi, with lower levels at TGN and in medial and *cis cisternae* and was detectable in peri-Golgi vesicles, which were also stained for GOLPH3 (**Figure S2C**). GOLPH3 OE resulted in a relative decrease of LCS-HA in *trans cisternae* and TGN and an increase in medial and *cis cisternae*, i.e., in a shift to earlier compartments, and a marked increase in peri-Golgi vesicles. On the contrary, GOLPH3 KD resulted in low LCS-HA levels in the Golgi stack and in the absence of LCS-HA from vesicles (**FigureS2C**), suggesting that LCS leaves the stack in the absence of GOLPH3 (see below). These data are consistent with GOLPH3 controlling the Golgi distribution of LCS by promoting its *trans*-to-*cis* retrograde transport via COPI vesicles. They also indicate that retention of LCS in the *trans cisterna* depends exclusively on GOLPH3, and that GOLPH3 recycles LCS in synchrony with cisternal progression, a feature diagnostic of a role of GOLPH3 in traffic by cisternal maturation.

For experiments in yeast, we monitored Mnn9p, a client of the GOLPH3 yeast homologue Vps74p ((*27*)). Banfield and coworkers have shown that Vps74p mediates the Golgi retention of a discrete group of Golgi resident *cis* enzymes (*27*) and that in *vps74*Δ yeast cells these enzymes are missorted to the vacuole, where they are degraded (*27*). We first characterized the cellular location of one of these enzymes, Mnn9p (chosen because of its relative abundance) in wild type (WT) and in *vps74*Δ yeast cells (**Figure S3A**). In WT cells, Mnn9p was

visualized in the *cis*-Golgi, as expected, while in *vps74*Δ was found also in the vacuole and in the *trans*-Golgi (as marked by Sys1p), presumably ascribable to loss of Golgi retention of this protein and passage through this organelle *en route* to the vacuole (**Figure S3A**). After 60 min of protein synthesis inhibition, Mnn9p was still present the Golgi in WT cell, plausibly due to its constant recycling, while it was completely lost in *vps74*Δ cells (**Figure S3B**). Thus, as just shown for LCS and GOLPH3, the retention and polarized localization of Mnn9p at the Golgi depends on Vps74p.

We then examined Mnn9p transport by visualizing cisternal conversion *in vivo*, using Sys1p as a *trans*-Golgi marker (*16, 19*). In WT cells, Mnn9p left the maturing *cis cisterna* as soon as it started acquiring the *trans* marker Sys1p in a process that took ~ 1 min to be completed, as reported previously for many maturing enzymes (*16, 17*). On the contrary, in *vps74*Δ cells, Mnn9p remained in the *cisterna* until it was filled with the Sys1p *trans* marker, and then left it, presumably for the vacuole (**Figure 3A**). To verify that Mnn9p leaves the *trans* cisterna to reach the vacuole, we set up a method to visually synchronize a wave of Mnn9p through the secretory pathway using the superfolder-GFP tag (Mnn9p-sfGFP) ((*48*)). We photobleached Mnn9p-sfGFP and monitored the newly synthesized (and rapidly folded) Mnn9p-sfGFP as it progressed through the secretory pathway. In WT cells newly synthesized Mnn9p-sfGFP was quickly transported (2-4 min) to the Golgi and then retained there for the duration of the experiment, (i.e., up to 30 min), while in *vps74*Δ cells Mnn9p-sfGFP reached the Golgi complex but was not retained there and proceeded to the vacuole in 5 min (**Figure 3B**). Notably the observed traffic effects are not due to differences in the Mnn9p-sfGFP synthetic rates between the two yeast strains (**Figure S3C**), and the transport rate of Mnn9p-sfGFP to the vacuole in *vps74*Δ cells is similar to that of a vacuolar cargo protein (Vph1p-sfGFP) (**Figure S3C**).

Altogether, the results in both mammalian and yeast cells indicate that GOLPH3 (and Vps74p) are responsible for retention of their client enzymes in the Golgi by acting as integral components of the cisternal maturation mechanism.

GOLPH3 increases the levels of its clients by delaying their transport to the degradative lysosomal compartment

Prompted by these results, we examined the effects of manipulating the GOLPH3 levels on the overall distribution and cellular fate of its GSL metabolic client enzymes, with a focus on LCS. For these and other experiments in this study, we used both HeLa cells and primary human fibroblasts (PHFs). We first characterized the impact of GOLPH3 OE and KD on endogenous LCS by IF. As shown in **Figure 4A** in PHFs, endogenous LCS localized in the Golgi, as expected. Somewhat unexpectedly, the effect of GOLPH3 OE and GOLPH3 KD was to substantially increase and decrease the Golgi levels of LCS, respectively. In HeLa cells, GOLPH3 OE had a similar effect as in PHFs (**Figure 4B**), however, it was impossible to measure the effects of

GOLPH3 KD on endogenous LCS because of the very low expression levels of this enzyme in this cell line. We thus performed equivalent experiments measuring HA-tagged LCS expressed by adenoviral vectors. We found that GOLPH3 KD has very similar effects to those seen on the endogenous enzyme in PHFs, (i.e., it reduced LCS-HA at the Golgi); moreover, GOLPH3 OE, in addition to increasing the overall LCS-HA levels, partially redistributed it to the ER (**Figure 4C**). Western blotting experiments performed in these conditions confirmed that, similarly to what observed by IF in PHFs, GOLPH3 OE increased, and GOLPH3 KD decreased, LCS-HA protein levels in HeLa cells (**Figure 4D**).

The effects of GOLPH3 on LCS levels could be either due to changes in LCS expression or to variations in the LCS protein turnover. The data with the LCS-HA construct speak against a transcriptional effect; nonetheless, we tested the effect of GOLPH3 OE or KD on the mRNA levels of *B4GALT5* (encoding LCS) and found no significant alteration, confirming that GOLPH3 does not affect LCS transcription (**Figure S4A**) and hence suggesting that it affects LCS degradation. To analyze this possibility, we studied the effects of GOLPH3 on the trafficking of LCS-GFP_RUSH through the secretory pathway. A synchronized transport wave of LCS-GFP_RUSH was monitored by video microscopy in both GOLPH3-KD and GOLPH3-OE cells (**Figure 4E** and **Movie S1**). GOLPH3 did not affect the transport LCS-GFP_RUSH from the ER to the Golgi. Instead, GOLPH3 markedly impacted the residence time of LCS-GFP_RUSH at the Golgi. In control cells, LCS-GFP_RUSH persisted in the Golgi region for ~ 2.5 hours before dissipating into punctate cytosolic structures that could be counter-stained with the lysosomal marker LAMP1 (**Figure S4B**), and then disappeared. In GOLPH3-KD cells LCS-GFP_RUSH left the Golgi rapidly to colonize the LAMP1 positive structures within less than 1 hour (we note that this Golgi residence time is compatible with the 20 min transit time from *cis* to *trans cisternae* reported in **Figure 2**, since the Golgi perinuclear region monitored in these experiments includes the ER-Golgi intermediate compartment (ERGIC) (REF) and TGN compartments). In GOLPH3-OE cells, instead, LCS-GFP_RUSH remained at the Golgi for up to 10 hours (longest recording time) and never made it to LAMP1 positive puncta (**Figure 4E, S4B** and **Movie S1**).

These data, combined with the results in **Figure 2**, indicate that a) in control cells, LCS, after rapidly reaching the *trans cisterna*, (**Figure 2B-D**) slowly escapes to the lysosomes, and b) GOLPH3 delays this LCS relocation to the lysosomes, with an efficiency proportional to its expression levels, most likely by retrotransporting LCS against the progression of the Golgi *cisternae*. Noting that arrival to the lysosomes should lead to LCS degradation, we evaluated the LCS-GFP_RUSH protein levels by Western Blotting during synchronized transport. We observed that: in control cells the LCS-GFP_RUSH protein starts to decline after being glycosylated at the Golgi, with a half-life of ~ 2-3 hours, compatible with the LCS residence time in the Golgi; in GOLPH3-KD cells this decline is faster (half-life < 1 hour): and in GOLPH3 OE cells the decline is extremely slow, or not detectable, even 8 hours after release from the ER (**Figure 4F, G**). Control experiments were performed with the non-GOLPH3 client GalT1 in its GalT1-GFP_RUSH form. Interestingly GalT1-GFP_RUSH shows a much longer half-life than LCS-

GFP_RUSH under control conditions and no difference was observed under GOLPH3 OE or KD (**Figure S4C**).

Experiments were also conducted on LCS-HA at steady state with the lysosomal degradation inhibitor bafilomycin (*49*), and confirmed the role of GOLPH3 in LCS degradation: a) in GOLPH3 KD cells LCS massively accumulated in the lysosomes in the presence of bafilomycin, b) in GOLPH3 OE cells LCS never appeared in the lysosomes even after bafilomycin treatment (**Figure 4H**); and c) in control cells the phenotype was intermediate, with most of the LCS protein in the Golgi but also with detectable levels associated with lysosomes in the presence of bafilomycin. Similar experiments were performed measuring endogenous LCS in PHFs, with similar results (not shown). When the LCS-HA was assessed by Western blotting it was found to be markedly increased by bafilomycin in GOLPH3 KD cells, indicating that LCS is substantially degraded by lysosomes; and to be increased by bafilomycin to a lesser extent in control cells, and to be unaffected by bafilomycin in GOLPH3-OE cells (**Figure 4I**). Thus, GOLPH3 regulates Golgi to lysosomes relocation and degradation of LCS also under conditions of steady-state traffic.

Finally, we examined whether GOLPH3 affects the levels and traffic behaviors of other client enzymes. We found that the localization of the GOLPH3 clients Gb3S, and GD3S (see **Figure 1A**; but also of GM3S; see **Discussion**) to be impacted by GOLPH3, with effects very similar to those observed with LCS. Specifically, we observed decreased levels and redistribution to cytosolic puncta of these enzymes in GOLPH3 KD and increased levels and relocation to the ER in GOLPH3 OE (**Figure 4J, K** and **S4D**). Moreover, when the localization of the these glyco-enzymes was examined in cells treated with bafilomycin, they were found to accumulate in LAMP1 positive structures in GOLPH3 KD (**Figure S4E**). In contrast, enzymes not bearing the GOLPH3 binding motif (i.e., GalT1; sphingomyelin synthase 1 [SMS1]; glucosylceramide synthase [GCS]; LC3S; GM2S and GM1 synthase [GM1S]) were insensitive to GOLPH3 KD or OE (**Figure S4F**).

These data confirm that GOLPH3 is responsible for regulating the Golgi retention, lysosomal degradation, and thus, ultimately, the cellular levels of specific glyco-enzymes of the GSL metabolic pathway. The retention of GOLPH3 clients in the Golgi *trans cisterna* appears to be sub-optimal, both in PHFs and in HeLa cells, so that, under physiological conditions, they leak out of the Golgi for the lysosomes, where they are degraded. Under conditions of GOLPH3 OE, Golgi retention is more effective, leading to reduced degradation rates, while GOLPH3 KD causes the opposite effects by allowing fast passage of the enzymes to the lysosomes. As a result, GOLPH3 OE markedly increases, and GOLPH3 KD decreases, the levels of LCS and of other GOLPH3 clients.

By altering the levels of its clients, GOLPH3 alters the assembly of glycans on sphingolipids.

We next examined whether and how the effects of GOLPH3 on its GSL client enzymes affect GSL metabolism. GSLs are glycosylated derivatives of ceramide (Cer) (*50*). After synthesis in the ER, Cer is either carried to the TGN by the lipid transfer protein CERT, where it is converted to sphingomyelin (SM), or it moves by vesicular transport to the *cis* Golgi, where it is glycosylated to produce glucosylceramide (GlcCer) (*51*). GlcCer then reaches the trans-Golgi either via the lipid transfer protein FAPP2 or by vesicular transport (*52, 53*) and it is further glycosylated to lactosylceramide (LacCer) by the GOLPH3 client LCS. LacCer is a key branch-point metabolite that feeds into each of the main four complex GSL metabolic pathways (i.e., the globo, ganglio, lacto and asialo series; **Figure S1A**) (*50, 54*).

We overexpressed or depleted GOLPH3 in both HeLa cells and PHFs and examined GSL metabolites by targeted mass spectrometry. In HeLa cells GOLPH3 KD induced an increase of Cer and GlcCer, and a strong decrease of Gb3 levels (**Figure 5A, B**), while GOLPH3 OE reduced the levels of Cer (in particular of the bioactive C16:0 Cer (*55, 56*) and increased the levels of Gb3, which is synthesized downstream of LacCer, though not those of LacCer itself (**Figure 5A-B**). In PHFs, GOLPH3 KD increased Cer and GlcCer, and GOLPH3 OE increased LacCer levels (**Figure S5A**). Importantly, whole lipidome analysis of GOLPH3 KD and OE HeLa cells did not show significant changes in other segments of lipid metabolism (**Figure S5B**).

We also tested the effects of GOLPH3 on PM GSLs composition by assessing the binding to HeLa cells of the toxins ShTxB and Cholera Toxin B fragment (ChTxB) that recognize Gb3 and GM1, respectively, by cytofluorimetry. Under control conditions, ShTxB stained most of the cells, while ChTxB stained only a small fraction (~ 5%) of the cells in agreement with previous reports (*57*). In GOLPH3 KD cells, staining by both the toxins was nearly abolished, indicating that GOLPH3 is required for both GM1 and Gb3 synthesis. GOLPH3 OE specifically stimulated ShTxB (Gb3) binding but had no detectable effect on ChTxB (GM1) binding (**Figure 5C**). This is possibly because the increased Gb3S induced by GOLPH3 competes with GM3S for LacCer consumption.

Finally, we assessed the effects of GOLPH3 on the GSL synthetic flux by [^{3}H]-sphingosine pulse-chase experiments in both HeLa cells and PHFs (see **Methods** for details). As shown in **Figure 5D** and **Figure S5C,** in both HeLa cells and in PHFs, GOLPH3 KD inhibited the production of the complex GSLs Gb3 and GM3 (a direct GM1 precursor) while GOLPH3 OE specifically stimulated the production of Gb3 at the expense of precursors Cer and GlcCer, in line with the mass spectrometry and cytofluorimetic data. The synthesis of SM was only modestly affected by GOLPH3-KD or GOLPH3 OE, while metabolites of the lacto and asialo series were not detected in these cell lines in agreement with previous reports (*52, 58*) (**Figure 5D** and **Figure S5C**).

The effects of GOLPH3 on GSL metabolism are compatible with the observed increase in the levels of the GSL pathway enzymes LCS and Gb3S that promote the synthesis of Gb3 at the expense of metabolites upstream of LCS, i.e., Cer and GlcCer. Some cell-type specific

differences (i.e., the effects on overall LacCer levels) can be explained with the help of the scheme in **Figure S5D**, which shows how the levels of LacCer depend on the balance between its synthesis by LCS and its conversion by Gb3S (both controlled by GOLPH3) where this balance is different in different cell lines. Along similar lines, the large increase in Gb3S levels induced by GOLPH3 probably competes with GM3S for LacCer usage, thus favoring Gb3 over GM3 production. In all, what remains constant across cell types and experimental conditions is the increase in flux from the metabolic pool upstream of LCS (Cer and GlcCer) to the metabolite pool downstream of LCS (LacCer and Gb3), indicating that LCS has a pivotal role in the effects of GOLPH3 on GSL metabolism.

We thus asked whether manipulating the levels of LCS is sufficient to recapitulate the metabolic changes induced by GOLPH3. To this end, we overexpressed or depleted LCS in HeLa cells and assessed the effects of these treatments on GSL metabolites. As shown in **Figure S5D**, LCS KD increased Cer and GlcCer species, similar to the effects of GOLPH3 KD, and LCS OE reduced the levels of specific Cer species, again similar to the effects of GOLPH3 OE. Differently from GOLPH3 OE was that LCS OE substantially increased the levels of LacCer, consistent with the fact that under these conditions there was no increase in the levels of Gb3S, which consumes LacCer. Regardless, the increased production of LacCer induced by LCS OE was sufficient to boost (though not to the same extent as with GOLPH3 OE) the production of Gb3 as assessed by ShTxB staining in cytofluorimetric experiments (**Figure S5E**). Thus, LCS OE and KD qualitatively phenocopied the effects on GSL metabolism of GOLPH3 OE and KD, respectively.

LCS and Gb3s mediate the GOLPH3 effects on mitogenic signaling and cell growth

GOLPH3 exerts stimulatory effects on tumor growth and on mitogenic signaling pathways (*59-62*), including PI3K, Akt, mTOR and p21/ WAF. Moreover, these pathways have been shown to be involved in the pro-growth action of GOLPH3 (*39, 62*). As shown here, GOLPH3 affects GSL metabolism, which is also known to influence cell mitogenic signaling and cell proliferation (*63-66*). We thus, analyzed the links between the effects of GOLPH3 on the GSL metabolic enzymes and on mitogenic signaling and growth.

We first asked whether the effects of GOLPH3 on the levels of LCS and Gb3S mediate the GOLPH3-induced mitogenic signaling and cell growth. As shown in **Figure 6A** and **S6A**, the overexpression of LCS in HeLa cells or PHFs had comparable stimulatory effects to those of GOLPH3 OE on Akt and mTOR signaling (i.e., they increased phosphorylation of Akt [at Ser308 and Ser473], and of both p70s6k and 4E-BP1), and decreased the expression of p21/ WAF. Conversely, the depletion of either LCS or GOLPH3 depressed the Akt-mTor pathway and enhanced the expression of p21/ WAF in both HeLa cells and PHFs. We note that, while some of the effects were quantitatively different in the two lines, the overall phosphorylation patterns were similar in Hela and PHFs. Moreover, both GOLPH3 and LCS KD inhibited HeLa cell

proliferation and anchorage independent growth as judged by growth assays in adherence and in soft agar (**Figure 6B, C**) and GOLPH3 and LCS OE both stimulated anchorage independent growth (**Figure 6C**).

Next, we examined whether LCS (and more in general GSL synthesis) is necessary for GOLPH3-induced mitogenic signaling and cell proliferation. To this end, we used GCS and LCS KO HeLa cells produced by the TALEN technology (*67*) and examined the effects of GOLPH3 OE in both GCS and LCS KO cells. GOLPH3 OE was unable to induce activation of Akt/mTOR signaling (both in GCS and LCS KO) cells and to stimulate anchorage-independent growth in LCS-KO cells (**Figure 6E** and **6E**). The production of complex GSL in GCS and LCS KO cells were strongly depressed, as expected (**Figure S6B**). LCS OE in LCS KO cells reestablished GSL production (**Figure S6B**) and promoted growth (**Figure 6D**). Notably, LCS KO cells, though unresponsive to GOLPH3 OE could be induced to grow by the expression of an unrelated oncogene i.e., Ras-Val12 (*68*) (**Figure S6C**), indicating that active GSL metabolism is essential for GOLPH3 dependent growth, but not for growth in general.

Finally, we considered that both GOLPH3 and LCS OE stimulate the production of Gb3, and that and asked whether LacCer needs to be converted into Gb3 to activate mitogenic signaling. To test this possibility, we depleted Gb3S, and monitored the signaling response to GOLPH3 OE. Depletion of Gb3S strongly depressed mitogenic signaling and anchorage-independent growth in a way that could not be rescued by GOLPH3 OE (**Figure S6D, E**), indicating that the synthesis of globosides is necessary for GOLPH3 dependent signaling and cell growth. Notably, since LCS OE phenocopies the effects of GOLPH3 OE on both GSL metabolism and on cell growth, the basal activity of Gb3S is sufficient, at least in HeLa cells and PHFs, to exploit the LCS dependent increase in LacCer to stimulate mitogenic signals and growth. The KD of the initiating enzymes of the other series (ganglio, lacto and asialo) had barely detectable and non-reproducible effects on GOLPH3 OE- induced mitogenic signaling (Not shown).

After synthesis in the Golgi, globosides are rapidly exposed on the cell surface where they exert modulatory actions on PM receptors including integrins and receptors of the tyrosine kinase family (RTKs), especially at focal adhesions (*69*). If globosides mediate the effects of GOLPH3 by activating a PM receptor, the effects of GOLPH3 and LCS OE on signaling should manifest themselves at the cell surface. This is expected to result in increased PtdIns(3,4,5)P_3 production downstream RTKs and PtdIns-3 Kinase (PI3K) activation. To test this possibility, we used the PtdIns(3,4,5)P_3 sensor PH-Akt-GFP and found that both GOLPH3 and LCS OE induced the recruitment of PH-Akt-GFP at the PM in serum starved cells (**Figure 6F-J** and **Movie S2**) while other PM phosphoinositides [i.e., PtdIns(4)P, and PtdIns(4,5)P_2 as detected by PH-ORP5-GFP (*70*), and PH-PLCδ-GFP (*71*) respectively], were not affected by GOLPH3 or LCS OE (**Figure S6H**). Insulin administration further activated PI3K at the PM, in an additive but non-synergic fashion with GOLPH3 or LCS OE (**Figure 6I-J**). The PI3K inhibitors wortmannin or GDC-0941 [REFs] inhibited completely the GOLPH3 or LCS OE dependent PtdIns(3,4,5)P_3 production at the PM

(**Figure S6G**) as well as, importantly, all the Akt and mTOR phosphorylation signals (**Figure S6K**), suggesting that sustained PtdIns(3,4,5)P_3 production at the PM is responsible for the activation of the Akt-mTor pathway in both GOLPH3 and LCS-OE cells (**Figure S6L**).

The GOLPH3-dependent increase of the LCS levels plays a role in human cancers

Finally, we asked whether the GSL-dependent mechanism of action of GOLPH3 OE in the induction of cell proliferation applies to cancer cell lines and tissue exhibiting *GOLPH3* amplification. To test this, we first examined two prostatic cancer cell lines, LNCaP and DU145, only the latter of which shows *GOLPH3* genomic amplification (according to the cBioportal database [http://www.cbioportal.org ; (*72*)]. The DU145 line, indeed showed higher levels of GOLPH3, but also of endogenous LCS and related complex GSLs (among which Gb3) compared to LNCaP cells (**Figure S7A, B**). Importantly, DU145 also displayed stronger basal phosphorylation of the mTOR substrates p70S6K and p4E-BP1 (**Figure S7B**). When we depleted LCS (or GOLPH3) in either the DU145 or in the LNCaP cell line (**Figure S7C**), growth of the DU145 cells was potently inhibited, while LNCaP cells were only marginally affected, as judged by the soft agar colony formation assay (**Figure 6F)**. Thus, *GOLPH3* amplification correlates with GOLPH3 overexpression and increased LCS protein levels; moreover, cells where *GOLPH3* is amplified specifically depend on LCS for growth.

We then analyzed actual human tumors. The *GOLPH3* gene has been originally reported to be amplified in different tumor types, with a particularly high frequency (56%) in non-small cell lung cancer (NSCLC) (*39*), and database searches for GOLPH3 copy number variations (CNVs) in large cohorts of lung cancer patients return (when using stringent definition criteria) significant, though lower, amplification frequencies (~10%) (cBioportal) (**Figure S7D**). The GOLPH3 protein levels have been reported by many studies to be higher than in healthy lung tissue in > 70% of in tumor biopsies from NSCLC patients, and to correlate with poor survival (*73, 74*). Using a tissue microarray (TMA) prepared from 72 surgical specimens from NSCLC patients (22 females and 50 males with median age at surgery of 63.5 years) (**Figure 7A**), we examined the correlation between the levels of GOLPH3 and those of LCS. To this end, we analyzed *GOLPH3* CNVs by fluorescence in situ hybridization (FISH) (**Figure 7B**) and GOLPH3 and LCS protein levels by immunohistochemistry (IHC) (**Figure 7C, D**). As shown in **Figure 6B** and **C** and in **Table S1**, ~12% and ~40% of the analyzed samples had a *GOLPH3* CN > 6 (amplification) and 4 respectively, and > 60% of the analyzed samples displayed moderate to high GOLPH3 protein expression levels, in line with previous reports. When we examined the LCS protein we found that cancer samples with high GOLPH3 protein levels showed also high LCS protein levels (~65% of cases; Figure 6C, D), while only ~20% of the GOLPH3 weak or negative samples had moderate to high LCS expression levels (**Figure 6C, D** and **Table S1**) Overall, we observe a significant (χ^2 p-val < 0.0001) correlation between GOLPH3 and LCS

protein levels, suggesting that the mechanisms by which GOLPH3 controls LCS levels is likely to operate in human patients.

Discussion:

In this study, we have analyzed the mechanistic links between intra-Golgi transport dynamics, glycan assembly and cellular functions, by manipulating the cargo recycling adapter GOLPH3. Our main findings are that: a) GOLPH3 selectively binds and retrotransports a subset of *trans*-Golgi enzymes involved in the assembly of glycans on sphingolipids. GOLPH3 operates as a component of the cisternal maturation mechanism, which requires the recycling of all Golgi enzymes, yet most *trans*-enzymes recycle independently of GOLPH3, indicating that cisternal maturation is an ensemble of recycling enzymatic modules. b) GOLPH3 controls the levels of its clients through a regulated-degradation mechanism based on accelerating their retrotransport and delaying their escape from the Golgi into the lysosomes and their lysosomal degradation. c) By targeting key enzymes of the GSL synthetic pathway, positioned both in the common axis and at the branchpoint between complex GSL series, GOLPH3 OE alters the patterns of glycans assembly on sphingolipids, effectively reprogramming metabolism to produce growth-promoting GSLs. Thus, when GOLPH3 is overexpressed, the levels of the oncosuppressor Cer decrease, while complex GSLs, and in particular the globosides, which are positive modulators of RTKs and integrin receptors at the PM, resulting in excessive growth (*75*). Results coherent with this scheme have been obtained in multiple cancer and primary cell lines (i.e., HeLa, Du145, LNCaP and PHFs), moreover, clinical data suggest that the same mechanism operates in actual human tumors.

Our findings represent a first glimpse into the mechanisms by which intra-Golgi transport regulates glycan assembly and associated biological functions. The mechanistic principles underlying GOLPH3 action, namely, the potentiation of its clients over competing enzymes, and hence the production of certain glycans over others, may apply to other glycosylation pathways. The current findings therefore help to outline a program for the analysis of the role of the Golgi in glycosylation based on the identification and analysis of: the Golgi enzyme adapters and of the biosynthetic modules they control, the mechanisms of regulation of these adapters, the types of interplay between different adapter/glycosylation pathways systems. Importantly, our data also outline a novel mechanism of action for GOLPH3-induced proliferation based on GSL biosynthesis that can be exploited for pharmacological intervention in GOLPH3-dependent tumors.

These and other salient aspects of our findings are discussed below.

GOLPH3 binds and retains in the Golgi a selected group of enzymes of the GSL biosynthetic pathway; yet, it is an integral component of the cisternal maturation mechanism.

An unexpected feature in the mechanism of action of GOLPH3 is its ability to bind a consensus sequence in the cytosolic tail of glyco-enzymes belonging to the GSL synthetic pathway, and hence, to control GSL metabolism. Compared to yeast, the GOLPH3 mammalian consensus lost a hydrophobic residue upstream of LxxR and acquired a second component with one or more positively charged residues in the same region. (*27*) This divergence is of unknown meaning, but might relate to the appearance of new modulatory mechanisms in evolution whereby Vps74p does not bind physically, but it interacts genetically with components of the yeast GSL synthetic system (*76*). While an intact GOLPH3 binding consensus appears to be necessary and sufficient for localization of the enzymes analyzed in this study, another portion of the glyco-enzymes, i.e., the transmembrane domain (TMD) has a role in Golgi retention that depends on the length and composition of this domain. (*77, 78*). The TMD is likely to cooperate with the GOLPH3-dependent sorting for incorporation of enzymes in COPI vesicles, on the basis of the degree of compatibility between the length of the TMD and the vesicle membrane thickness and composition (*77, 79*). Moreover, the TMD mediates glyco-enzymes homo and hetero-dimerization with consequences on their localization (*80, 81*). This could be relevant for EXT1 and EXT2 that are GOLPH3 clients and form a heterodimer ((*33*)) whereby only EXT2 tail bears the [+]-$x_{(2-5)}$-LxxR motif (see **Figure S1E**). Along similar lines GM3S, that behaves like a GOLPH3 client but apparently does not bind GOLPH3, has been shown to be part of a multi-enzymatic complex with LCS and GD3S (*82*) (both of which are direct GOLPH3 interactors, see **Figure 1A**).

Beyond the mechanistic aspects of GOLPH3 binding, of broad relevance is the fact that GOLPH3 mediates the recycling of a selected group of enzymes of the GSL synthetic pathway, yet it acts as an integral component of cisternal maturation, as judged by the principle of synchrony between cargo progression and enzyme retrotransport (**Figure 2**). Cisternal maturation has so far been considered a constitutive process aimed merely at maintaining the constancy of the enzymatic composition of *cisternae* progressing through the stack via the synchronous recycling of all the Golgi residents (*83, 84*). Thus, the finding that GOLPH3 selectively controls the components of one specific enzymatic pathway without affecting other glyco-enzymes calls for a change of the concept of cisternal maturation, now to be seen as an ensemble of different enzymatic modules recycling presumably via specialized adapters. A recent report that five O-glycosylation enzymes are retained in the *cis*-Golgi through binding to the COPI zeta and delta subunits (*29*), as well as the original report about binding of Vps74p to some but not all yeast enzymes (*27*) are consistent with this scheme, although evidence that these enzymes behave in accord with the synchrony principle required for cisternal maturation remains to be provided.

An implication of this revised maturation model is that entire glyco-enzyme modules, or glycosylation pathways, might be controlled through the regulation of the activity of relevant adapters. Accordingly, specific signaling kinase cascades have been shown to affect overall glycosylation patterns (*85*). Furthermore, GOLPH3 is regulated at another level via its controlled recruitment to Golgi membranes through interaction with PtdIns(4)*P* (*37*), which also recruits CERT and FAPP2 to Golgi membranes to determine the directional non-vesicular transfer of Cer and GlcCer to the *trans* Golgi (*51, 52, 54*). Several investigators, including ourselves, have reported that the PtdIns(4)*P* content of Golgi membranes is subject to sharp regulation and that fluctuations in PtdIns(4)*P* levels impact GOLPH3, CERT, and FAPP2 localization and function (*86-88*), implying that the PtdIns(4)*P* Golgi content coordinately influences GSL synthetic enzyme localization and protein levels along with the local provision of GSL precursors. While this suggests that the PtdIns(4)*P*-GOLPH3 systems impacts proliferation via the control of the GSL enzymatic module, other modules might be subjected to similar dysregulation, leading to disease, and the cisternal maturation mechanism in general might be relevant in multiple physiological and pathological conditions.

GOLPH3 increases the levels of its GSL client enzymes through a regulated-degradation mechanism.

GOLPH3 redistributes its clients retrogradely in the biosynthetic pathway. It is generally thought that Golgi transport might affect glycan assembly through relocation of enzymes into ectopic *cisternae* where they interfere with local glycosylation by competing for critical substrates. This might be the case of the N-glycosylation pathway where Mgat3 and Fut8 can compete with Mgat5, changing the structure and function of the glycans produced (*89-91*). Along these lines, Bard and colleagues have recently shown the functional importance of the relocation of GalNac-Ts from the Golgi to the ER in cancer (*92*).

GOLPH3, however, appears to exerts its effects by regulating the levels, rather the distribution, of its clients, as confirmed by the observation that LCS OE phenocopies GOLPH3 OE. This effect is determined by a degradation-based regulatory process. Degradation-based mechanisms have been used repeatedly in nature to control the levels of functionally crucial proteins. Among these, well characterized are the cases of p53 and β-catenin (*93, 94*), both of which are kept constitutively low by targeted ubiquitination and proteasomal degradation, but can be increased rapidly through signal-triggered inhibition of degradation (*93, 94*).

In the case of the GOLPH3 clients, regulation by degradation is mechanistically different. It relies on the fact that GOLPH3-dependent recycling that keeps GOLPH3 clients at the *trans*-Golgi, operates at a suboptimal rate. Thus, a fraction of the GOLPH3 clients fails to be recycled and continuously leaves the stack for the lysosomes where it is degraded. This, at least for LCS, results in a half-life of ≈ 2 hours (shorter than for most cellular proteins). This relatively rapid decay determines the extent of the GOLPH3-dependent regulation: when GOLPH3 is overexpressed, as observed in many tumors, LCS recycles more efficiently and does not reach

the lysosomes. As a result, it is degraded less and its levels increase markedly. Conversely, when GOLPH3 is depleted, LCS is degraded rapidly. Thus, GOLPH3 acts as a rheostat that controls the flow of its clients to the lysosomes, thereby regulating their levels. Notably, the basal turnover of glyco-enzymes may vary across cell lines and conditions; however, observations consistent with the above degradation-based mechanism have been obtained in several cell lines as well as in cancer samples from human patients. Thus, while glycosylation changes, a frequent observation in cancer cells, have been so far interpreted as being due to changed glycogenes expression, (*9*), regulated-degradation processes like the one described here should now be considered.

The GOLPH3-induced increase of selected GSL enzymes changes the pattern of glycan assembly on sphingolipids, and thus reprograms the GSL metabolic pathways to potentiate mitogenic signaling.

How do the increased levels of some GSL enzymes translate into mitogenic signaling? This can be explained by the selectivity of action of GOLPH3 and by the position of GOLPH3 clients in the GSL synthetic pathway. The GOLPH3 effect on LCS and of Gb3S is critical in this regard. LCS is part of the common axis of the GSL pathway, and consumes GlcCer (and, indirectly, its precursor Cer) to generate LacCer. LacCer is a branchpoint metabolite that feeds into all of the complex GSL metabolic pathways (globo, ganglio, lacto and asialo). Thus, Gb3S, once enhanced by GOLPH3, competes successfully for LacCer with the other complex GSL metabolic pathways (ganglio, lacto and asialo), directing GSL metabolism towards production of globosides. The fact that in HeLa cells the globo pathway is prevalent increases the dominance of the role of globosides in the action of GOLPH3, but the scenario might be different in other cell lines (see below).

In all, GOLPH3 OE results in production of growth-promoting globosides at the expense of the oncosuppressor Cer (see **Figure S5D**), effectively reprogramming the GSL metabolic pathway to induce cell proliferation. Globosides reside at the PM where they cluster in GSL rich-domains, often at focal adhesions (*69*). There, according to numerous reports, they exert activatory effects on PM integrin and RTK receptors, which in turn activate the PI3K-Akt-mTOR signaling pathways (*64, 65, 69, 75, 95-97*), and growth. Among the globosides, potential activatory candidates include Gb3 itself, Gb4, and sialoGb5, which have been shown to form complexes with specific RTKs or integrins and enhance the signaling mediated by these receptors (*64, 69, 95*). Thus, the observation that GOLPH3 and LCS OE potentiate PI3K activity at the PM, and that this is required for the GOLPH3 dependent stimulation of the Akt and mTOR cascade, is consistent with the available literature on globosides in signaling. Thus, our results suggest that GOLPH3 OE and LCS OE promote cell proliferation by enhancing the GSL metabolic flux from Cer and GlcCer towards the globosides, possibly stimulating RTKs at the PM where their identification in our model cells is beyond the scope of the study. Notably, the concomitant consumption of C16:0 Cer, might be a contributing factor to the pro-growth effects of GOLPH3 and LCS OE.

The mitogenic mechanism of action of GOLPH3 is likely to vary across cell and tumor types. While the globosides are the main players in our cell lines, other GSL series may be prevalent in other cells and tissues. In particular, enzymes of the ganglio and lacto pathways are GOLPH3 clients and might mediate the proliferative effects of GOLPH3 under various conditions. Gangliosides modulate many receptor responses (*98*), and one of the proven GOLPH3 clients is GD3S, which converts GM3, a negative modulator of the EGF and RTK receptors (*99, 100*), into GD3, which stimulates the same receptors (*101, 102*); A group of putative GOLPH3 clients of the lacto pathway are involved in the synthesis of Lewis antigens implicated in the development of different tumor types (*103, 104*). Other potential GOLPH3 clients involved in proteoglycan synthesis and in N- or O-glycosylation are likely to play a role in the actions of GOLPH3. Among the latter, ST6GALT1 has been proposed to mediate the effect of GOLPH3 on cell migration. In addition, GOLPH3 has been shown to act also through its effects on cargo export from the TGN and/ or through effects on the DNA damage response (*37, 87, 88, 105, 106*). Thus, while the effects of GOLPH3 on GSL metabolism play a central role in cell proliferation in our model cells, the mechanism of action of GOLPH3 is likely complex and to some extent dependent on the cell type and tissue examined.

GOLPH3 affects LCS levels in human cancers.

GOLPH3 has been proposed to act as an oncogene due to amplification, increased mRNA expression, and protein overproduction (*39*), in a number of reports and in a variety of human cancers (*107*). Thus, whether GOLPH3 exerts its pathogenic role in human patients through the mechanism of action unraveled in this study is of medical relevance. Here we provide evidence that: a) human tumors that overexpress GOLPH3 also upregulate LCS, suggesting that the shift in GSL metabolism that promotes mitogenic signaling in experimental cells occurs also in human cancers, b) cancer cell lines with *GOLPH3* amplification strongly express LCS, and their growth in soft agar is sensitive to LCS ablation, while tumor lines that depend on other oncogenes are much less sensitive; c) LCS itself shows oncogenic features (*108, 109*). Since the GSL metabolic enzymes are druggable (*110*), these findings suggest that pharmacologic inhibitors of LCS and of other the GOLPH3 enzyme clients may be developed into drugs for the treatment of GOLPH3 dependent tumors.

Acknoledgments

We thank Antonella De Matteis, Francesca Carlomagno, Lina Obeid and Daniela Corda for valuable discussions. We thank Nina Dathan for help with cloning and construct preparation. We thank Francesco Russo for Bioinformatic support. We thank Pasquale Barba for technical assistance and the FACS Facility of the Institute of Genetics and Biophysics (IGB-CNR, Naples). We thank Gabriele Turacchio for EM technical assistance and the Bioimaging Facility of the Institute of Protein Biochemistry. R.R. acknowledges financial support from Fondazione Italiana per la Ricerca sul Cancro (FIRC Fellowship 15111). A.L. acknowledges financial support from

the Italian Cystic Fibrosis Research Foundation (Project #6), AIRC (Projects IG 15767 and IG 20786), MIUR (Project ''FaReBio di Qualita`''), the Italian Node of Euro-Bioimaging (Preparatory Phase II – INFRADEV), TERABIO, and the CNR (PON Project 01/00117 and Projects 01-00862 and a3-00025). G.D.A. acknowledges financial support from Jebsen Foundation and from the Swiss National Science Foundation (SNSF) (grant number, 310030_184926).

Authors contributions

RR developed the idea, conducted most of the experiments and wrote the manuscript; DR participated in the development of the idea and conducted the experiments on signalling and peptide binding; KK conducted the experiments with yeast cells; PS, Conducted the GalT1-RUSH experiment and contributed to cell signaling and proliferation experimets ; BL was involved in the setup of the RUSH synchronization protocol of LCS-GFP-_RUSH and EM assesment of GOLPH3 distribution; DS assisted RR in conducting the experiments in an initial phase of the project; MZ conducted bioinformatics analysis of Golgi enzymes tails; AV Conducted the ITC experiments; PP Conducted the radioactive GAG secretion assay; VK, assisted RR in conducting the experiments the final phase of the project; LC conducted MALDI-MS and lipidomics measurements; GB and FP generated RUSH constructs, FZM, GA, and CV conducted in TMA experiment; PH Generated biotinylated peptides; LM expressed and purified recombinant GOLPH3; GB and AB analysed and interpreted the TMA data; HC and UM generated and provided LCS antibody; TY and KH generated and provided the GCS and LCS KO HeLa cells; SP, contributed to conception and design, analysis and interpretation of data and contributed to write the manuscript; YAH helped with analysis and interpretation of lipids MS data and contributed to write the manuscript; AN was Involved in data analysis and interpretation of yeast experiments; GDA developed the idea, designed and supervised the entire project, and wrote the manuscript; AL developed the idea, designed and supervised the entire project, and wrote the manuscript.

Competing interests

The authors declare that no competing of financial interests

References:

1. A. Varki, P. Gagneux, in *Essentials of Glycobiology,* rd *et al.*, Eds. (Cold Spring Harbor (NY), 2015), pp. 77-88.
2. P. Stanley, What Have We Learned from Glycosyltransferase Knockouts in Mice? *J Mol Biol* **428**, 3166-3182 (2016).
3. R. D. Cummings, "Stuck on sugars - how carbohydrates regulate cell adhesion, recognition, and signaling". *Glycoconj J* **36**, 241-257 (2019).
4. S. R. Stowell, T. Ju, R. D. Cummings, Protein glycosylation in cancer. *Annu Rev Pathol* **10**, 473-510 (2015).
5. P. Stanley, Golgi glycosylation. *Cold Spring Harb Perspect Biol* **3**, (2011).
6. S. S. Pinho, C. A. Reis, Glycosylation in cancer: mechanisms and clinical implications. *Nat Rev Cancer* **15**, 540-555 (2015).

7. K. J. Colley, A. Varki, T. Kinoshita, in *Essentials of Glycobiology,* rd *et al.*, Eds. (Cold Spring Harbor (NY), 2015), pp. 41-49.
8. P. Pothukuchi *et al.*, Translation of genome to glycome: role of the Golgi apparatus. *FEBS Lett*, (2019).
9. F. Dall'Olio, M. Trinchera, Epigenetic Bases of Aberrant Glycosylation in Cancer. *Int J Mol Sci* **18**, (2017).
10. F. Bard, J. Chia, Cracking the Glycome Encoder: Signaling, Trafficking, and Glycosylation. *Trends Cell Biol* **26**, 379-388 (2016).
11. J. E. Rothman, F. T. Wieland, Protein sorting by transport vesicles. *Science* **272**, 227-234 (1996).
12. A. Trucco *et al.*, Secretory traffic triggers the formation of tubular continuities across Golgi sub-compartments. *Nat Cell Biol* **6**, 1071-1081 (2004).
13. S. R. Pfeffer, How the Golgi works: a cisternal progenitor model. *Proc Natl Acad Sci U S A* **107**, 19614-19618 (2010).
14. G. H. Patterson *et al.*, Transport through the Golgi apparatus by rapid partitioning within a two-phase membrane system. *Cell* **133**, 1055-1067 (2008).
15. S. Emr *et al.*, Journeys through the Golgi--taking stock in a new era. *J Cell Biol* **187**, 449-453 (2009).
16. K. Matsuura-Tokita, M. Takeuchi, A. Ichihara, K. Mikuriya, A. Nakano, Live imaging of yeast Golgi cisternal maturation. *Nature* **441**, 1007-1010 (2006).
17. E. Losev *et al.*, Golgi maturation visualized in living yeast. *Nature* **441**, 1002-1006 (2006).
18. V. Malhotra, T. Serafini, L. Orci, J. C. Shepherd, J. E. Rothman, Purification of a novel class of coated vesicles mediating biosynthetic protein transport through the Golgi stack. *Cell* **58**, 329-336 (1989).
19. M. Ishii, Y. Suda, K. Kurokawa, A. Nakano, COPI is essential for Golgi cisternal maturation and dynamics. *J Cell Sci* **129**, 3251-3261 (2016).
20. J. S. Bonifacino, B. S. Glick, The mechanisms of vesicle budding and fusion. *Cell* **116**, 153-166 (2004).
21. R. Willett, D. Ungar, V. Lupashin, The Golgi puppet master: COG complex at center stage of membrane trafficking interactions. *Histochem Cell Biol* **140**, 271-283 (2013).
22. M. Wong, S. Munro, Membrane trafficking. The specificity of vesicle traffic to the Golgi is encoded in the golgin coiled-coil proteins. *Science* **346**, 1256898 (2014).
23. T. M. Witkos *et al.*, GORAB scaffolds COPI at the trans-Golgi for efficient enzyme recycling and correct protein glycosylation. *Nat Commun* **10**, 127 (2019).
24. E. Papanikou, B. S. Glick, Golgi compartmentation and identity. *Curr Opin Cell Biol* **29**, 74-81 (2014).
25. B. Goud, S. Liu, B. Storrie, Rab proteins as major determinants of the Golgi complex structure. *Small GTPases* **9**, 66-75 (2018).
26. C. L. Jackson, S. Bouvet, Arfs at a glance. *J Cell Sci* **127**, 4103-4109 (2014).
27. L. Tu, W. C. Tai, L. Chen, D. K. Banfield, Signal-mediated dynamic retention of glycosyltransferases in the Golgi. *Science* **321**, 404-407 (2008).
28. K. R. Schmitz *et al.*, Golgi localization of glycosyltransferases requires a Vps74p oligomer. *Dev Cell* **14**, 523-534 (2008).
29. L. Liu, B. Doray, S. Kornfeld, Recycling of Golgi glycosyltransferases requires direct binding to coatomer. *Proc Natl Acad Sci U S A* **115**, 8984-8989 (2018).
30. J. C. Casler, E. Papanikou, J. J. Barrero, B. S. Glick, Maturation-driven transport and AP-1-dependent recycling of a secretory cargo in the Golgi. *J Cell Biol* **218**, 1582-1601 (2019).
31. J. J. Kim, Z. Lipatova, U. Majumdar, N. Segev, Regulation of Golgi Cisternal Progression by Ypt/Rab GTPases. *Dev Cell* **36**, 440-452 (2016).
32. E. S. Eckert *et al.*, Golgi phosphoprotein 3 triggers signal-mediated incorporation of glycosyltransferases into coatomer-coated (COPI) vesicles. *J Biol Chem* **289**, 31319-31329 (2014).
33. W. L. Chang *et al.*, The Drosophila GOLPH3 homolog regulates the biosynthesis of heparan sulfate proteoglycans by modulating the retrograde trafficking of exostosins. *Development* **140**, 2798-2807 (2013).
34. M. F. Ali, V. B. Chachadi, A. Petrosyan, P. W. Cheng, Golgi phosphoprotein 3 determines cell binding properties under dynamic flow by controlling Golgi localization of core 2 N-acetylglucosaminyltransferase 1. *J Biol Chem* **287**, 39564-39577 (2012).
35. N. A. Pereira, H. X. Pu, H. Goh, Z. Song, Golgi phosphoprotein 3 mediates the Golgi localization and function of protein O-linked mannose beta-1,2-N-acetlyglucosaminyltransferase 1. *J Biol Chem* **289**, 14762-14770 (2014).
36. T. Isaji *et al.*, An oncogenic protein Golgi phosphoprotein 3 up-regulates cell migration via sialylation. *J Biol Chem* **289**, 20694-20705 (2014).
37. H. C. Dippold *et al.*, GOLPH3 bridges phosphatidylinositol-4- phosphate and actomyosin to stretch and shape the Golgi to promote budding. *Cell* **139**, 337-351 (2009).

38. C. S. Wood *et al.*, PtdIns4P recognition by Vps74/GOLPH3 links PtdIns 4-kinase signaling to retrograde Golgi trafficking. *J Cell Biol* **187**, 967-975 (2009).
39. K. L. Scott *et al.*, GOLPH3 modulates mTOR signalling and rapamycin sensitivity in cancer. *Nature* **459**, 1085-1090 (2009).
40. M. Jacewicz, H. Clausen, E. Nudelman, A. Donohue-Rolfe, G. T. Keusch, Pathogenesis of shigella diarrhea. XI. Isolation of a shigella toxin-binding glycolipid from rabbit jejunum and HeLa cells and its identification as globotriaosylceramide. *J Exp Med* **163**, 1391-1404 (1986).
41. M. M. Pierce, C. S. Raman, B. T. Nall, Isothermal titration calorimetry of protein-protein interactions. *Methods* **19**, 213-221 (1999).
42. S. Munro, H. R. Pelham, A C-terminal signal prevents secretion of luminal ER proteins. *Cell* **48**, 899-907 (1987).
43. A. A. Mironov *et al.*, Small cargo proteins and large aggregates can traverse the Golgi by a common mechanism without leaving the lumen of cisternae. *J Cell Biol* **155**, 1225-1238 (2001).
44. G. Boncompain *et al.*, Synchronization of secretory protein traffic in populations of cells. *Nat Methods* **9**, 493-498 (2012).
45. T. J. Schnitzer, C. Dickson, R. A. Weiss, Morphological and biochemical characterization of viral particles produced by the tsO45 mutant of vesicular stomatitis virus at restrictive temperature. *J Virol* **29**, 185-195 (1979).
46. R. Rizzo *et al.*, The dynamics of engineered resident proteins in the mammalian Golgi complex relies on cisternal maturation. *J Cell Biol* **201**, 1027-1036 (2013).
47. S. Y. Dejgaard, A. Murshid, K. M. Dee, J. F. Presley, Confocal microscopy-based linescan methodologies for intra-Golgi localization of proteins. *J Histochem Cytochem* **55**, 709-719 (2007).
48. J. D. Pedelacq, S. Cabantous, T. Tran, T. C. Terwilliger, G. S. Waldo, Engineering and characterization of a superfolder green fluorescent protein. *Nat Biotechnol* **24**, 79-88 (2006).
49. T. Yoshimori, A. Yamamoto, Y. Moriyama, M. Futai, Y. Tashiro, Bafilomycin A1, a specific inhibitor of vacuolar-type H(+)-ATPase, inhibits acidification and protein degradation in lysosomes of cultured cells. *J Biol Chem* **266**, 17707-17712 (1991).
50. A. H. Merrill, Jr., Sphingolipid and glycosphingolipid metabolic pathways in the era of sphingolipidomics. *Chem Rev* **111**, 6387-6422 (2011).
51. K. Hanada *et al.*, Molecular machinery for non-vesicular trafficking of ceramide. *Nature* **426**, 803-809 (2003).
52. G. D'Angelo *et al.*, Glycosphingolipid synthesis requires FAPP2 transfer of glucosylceramide. *Nature* **449**, 62-67 (2007).
53. G. D'Angelo *et al.*, Vesicular and non-vesicular transport feed distinct glycosylation pathways in the Golgi. *Nature* **501**, 116-120 (2013).
54. G. D'Angelo, S. Capasso, L. Sticco, D. Russo, Glycosphingolipids: synthesis and functions. *FEBS J* **280**, 6338-6353 (2013).
55. B. Fekry *et al.*, C16-ceramide is a natural regulatory ligand of p53 in cellular stress response. *Nat Commun* **9**, 4149 (2018).
56. B. J. Kroesen *et al.*, Induction of apoptosis through B-cell receptor cross-linking occurs via de novo generated C16-ceramide and involves mitochondria. *J Biol Chem* **276**, 13606-13614 (2001).
57. D. Russo *et al.*, Glycosphingolipid metabolic reprogramming drives neural differentiation. *EMBO J* **37**, (2018).
58. D. Halter *et al.*, Pre- and post-Golgi translocation of glucosylceramide in glycosphingolipid synthesis. *J Cell Biol* **179**, 101-115 (2007).
59. K. L. Scott, L. Chin, Signaling from the Golgi: mechanisms and models for Golgi phosphoprotein 3-mediated oncogenesis. *Clin Cancer Res* **16**, 2229-2234 (2010).
60. J. Sun *et al.*, GOLPH3 induces epithelial-mesenchymal transition via Wnt/beta-catenin signaling pathway in epithelial ovarian cancer. *Cancer Med* **6**, 834-844 (2017).
61. C. Z. Qiu *et al.*, Correlation of GOLPH3 Gene with Wnt Signaling Pathway in Human Colon Cancer Cells. *J Cancer* **7**, 928-934 (2016).
62. Z. Zeng *et al.*, Overexpression of GOLPH3 promotes proliferation and tumorigenicity in breast cancer via suppression of the FOXO1 transcription factor. *Clin Cancer Res* **18**, 4059-4069 (2012).
63. D. Russo, S. Parashuraman, G. D'Angelo, Glycosphingolipid-Protein Interaction in Signal Transduction. *Int J Mol Sci* **17**, (2016).
64. P. K. Chuang *et al.*, Signaling pathway of globo-series glycosphingolipids and beta1,3-galactosyltransferase V (beta3GalT5) in breast cancer. *Proc Natl Acad Sci U S A* **116**, 3518-3523 (2019).

65. K. Furukawa *et al.*, New era of research on cancer-associated glycosphingolipids. *Cancer Sci* **110**, 1544-1551 (2019).
66. Y. Guri *et al.*, mTORC2 Promotes Tumorigenesis via Lipid Synthesis. *Cancer Cell* **32**, 807-823 e812 (2017).
67. T. Yamaji, K. Hanada, Establishment of HeLa cell mutants deficient in sphingolipid-related genes using TALENs. *PLoS One* **9**, e88124 (2014).
68. R. W. Sweet *et al.*, The product of ras is a GTPase and the T24 oncogenic mutant is deficient in this activity. *Nature* **311**, 273-275 (1984).
69. W. F. Steelant *et al.*, Monosialyl-Gb5 organized with cSrc and FAK in GEM of human breast carcinoma MCF-7 cells defines their invasive properties. *FEBS Lett* **531**, 93-98 (2002).
70. J. Chung *et al.*, INTRACELLULAR TRANSPORT. PI4P/phosphatidylserine countertransport at ORP5- and ORP8-mediated ER-plasma membrane contacts. *Science* **349**, 428-432 (2015).
71. M. A. Lemmon, K. M. Ferguson, R. O'Brien, P. B. Sigler, J. Schlessinger, Specific and high-affinity binding of inositol phosphates to an isolated pleckstrin homology domain. *Proc Natl Acad Sci U S A* **92**, 10472-10476 (1995).
72. J. Gao *et al.*, Integrative analysis of complex cancer genomics and clinical profiles using the cBioPortal. *Sci Signal* **6**, pl1 (2013).
73. W. Tang *et al.*, Overexpression of GOLPH3 is associated with poor survival in Non-small-cell lung cancer. *Am J Transl Res* **8**, 1756-1762 (2016).
74. S. Tang, R. Yang, X. Zhou, H. Pan, J. Liu, Expression of GOLPH3 in patients with non-small cell lung cancer and xenografts models. *Oncol Lett* **15**, 7555-7562 (2018).
75. S. I. Hakomori Si, The glycosynapse. *Proc Natl Acad Sci U S A* **99**, 225-232 (2002).
76. C. S. Wood *et al.*, Local control of phosphatidylinositol 4-phosphate signaling in the Golgi apparatus by Vps74 and Sac1 phosphoinositide phosphatase. *Mol Biol Cell* **23**, 2527-2536 (2012).
77. H. J. Sharpe, T. J. Stevens, S. Munro, A comprehensive comparison of transmembrane domains reveals organelle-specific properties. *Cell* **142**, 158-169 (2010).
78. S. Munro, An investigation of the role of transmembrane domains in Golgi protein retention. *EMBO J* **14**, 4695-4704 (1995).
79. F. X. Contreras *et al.*, Molecular recognition of a single sphingolipid species by a protein's transmembrane domain. *Nature* **481**, 525-529 (2012).
80. T. Nilsson, P. Slusarewicz, M. H. Hoe, G. Warren, Kin recognition. A model for the retention of Golgi enzymes. *FEBS Lett* **330**, 1-4 (1993).
81. D. K. Banfield, Mechanisms of protein retention in the Golgi. *Cold Spring Harb Perspect Biol* **3**, a005264 (2011).
82. W. Spessott, P. M. Crespo, J. L. Daniotti, H. J. Maccioni, Glycosyltransferase complexes improve glycolipid synthesis. *FEBS Lett* **586**, 2346-2350 (2012).
83. B. S. Glick, A. Luini, Models for Golgi traffic: a critical assessment. *Cold Spring Harb Perspect Biol* **3**, a005215 (2011).
84. A. Nakano, A. Luini, Passage through the Golgi. *Curr Opin Cell Biol* **22**, 471-478 (2010).
85. J. Chia *et al.*, RNAi screening reveals a large signaling network controlling the Golgi apparatus in human cells. *Mol Syst Biol* **8**, 629 (2012).
86. S. Capasso *et al.*, Sphingolipid metabolic flow controls phosphoinositide turnover at the trans-Golgi network. *EMBO J* **36**, 1736-1754 (2017).
87. N. Halberg *et al.*, PITPNC1 Recruits RAB1B to the Golgi Network to Drive Malignant Secretion. *Cancer Cell* **29**, 339-353 (2016).
88. Z. Xie, S. K. Hur, L. Zhao, C. S. Abrams, V. A. Bankaitis, A Golgi Lipid Signaling Pathway Controls Apical Golgi Distribution and Cell Polarity during Neurogenesis. *Dev Cell* **44**, 725-740 e724 (2018).
89. G. D. Longmore, H. Schachter, Product-identification and substrate-specificity studies of the GDP-L-fucose:2-acetamido-2-deoxy-beta-D-glucoside (FUC goes to Asn-linked GlcNAc) 6-alpha-L-fucosyltransferase in a Golgi-rich fraction from porcine liver. *Carbohydr Res* **100**, 365-392 (1982).
90. E. A. Partridge *et al.*, Regulation of cytokine receptors by Golgi N-glycan processing and endocytosis. *Science* **306**, 120-124 (2004).
91. K. S. Lau *et al.*, Complex N-glycan number and degree of branching cooperate to regulate cell proliferation and differentiation. *Cell* **129**, 123-134 (2007).
92. A. T. Nguyen *et al.*, Organelle Specific O-Glycosylation Drives MMP14 Activation, Tumor Growth, and Metastasis. *Cancer Cell* **32**, 639-653 e636 (2017).
93. H. H. Jang, Regulation of Protein Degradation by Proteasomes in Cancer. *J Cancer Prev* **23**, 153-161 (2018).

94. A. Varshavsky, Regulated protein degradation. *Trends Biochem Sci* **30**, 283-286 (2005).
95. S. Y. Park, C. Y. Kwak, J. A. Shayman, J. H. Kim, Globoside promotes activation of ERK by interaction with the epidermal growth factor receptor. *Biochim Biophys Acta* **1820**, 1141-1148 (2012).
96. M. S. Wegner *et al.*, UDP-glucose ceramide glucosyltransferase activates AKT, promoted proliferation, and doxorubicin resistance in breast cancer cells. *Cell Mol Life Sci* **75**, 3393-3410 (2018).
97. Y. Ohkawa *et al.*, Ganglioside GD3 enhances adhesion signals and augments malignant properties of melanoma cells by recruiting integrins to glycolipid-enriched microdomains. *J Biol Chem* **285**, 27213-27223 (2010).
98. S. Julien, M. Bobowski, A. Steenackers, X. Le Bourhis, P. Delannoy, How Do Gangliosides Regulate RTKs Signaling? *Cells* **2**, 751-767 (2013).
99. E. G. Bremer, J. Schlessinger, S. Hakomori, Ganglioside-mediated modulation of cell growth. Specific effects of GM3 on tyrosine phosphorylation of the epidermal growth factor receptor. *J Biol Chem* **261**, 2434-2440 (1986).
100. U. Coskun, M. Grzybek, D. Drechsel, K. Simons, Regulation of human EGF receptor by lipids. *Proc Natl Acad Sci U S A* **108**, 9044-9048 (2011).
101. Y. J. Liang *et al.*, Interaction of glycosphingolipids GD3 and GD2 with growth factor receptors maintains breast cancer stem cell phenotype. *Oncotarget* **8**, 47454-47473 (2017).
102. J. Wang, R. K. Yu, Interaction of ganglioside GD3 with an EGF receptor sustains the self-renewal ability of mouse neural stem cells in vitro. *Proc Natl Acad Sci U S A* **110**, 19137-19142 (2013).
103. S. Hakomori, Aberrant glycosylation in tumors and tumor-associated carbohydrate antigens. *Adv Cancer Res* **52**, 257-331 (1989).
104. S. Hakomori, Y. Zhang, Glycosphingolipid antigens and cancer therapy. *Chem Biol* **4**, 97-104 (1997).
105. S. E. Farber-Katz *et al.*, DNA damage triggers Golgi dispersal via DNA-PK and GOLPH3. *Cell* **156**, 413-427 (2014).
106. J. Rahajeng *et al.*, Efficient Golgi Forward Trafficking Requires GOLPH3-Driven, PI4P-Dependent Membrane Curvature. *Dev Cell*, (2019).
107. R. S. Kuna, S. J. Field, GOLPH3: a Golgi phosphatidylinositol(4)phosphate effector that directs vesicle trafficking and drives cancer. *J Lipid Res* **60**, 269-275 (2019).
108. K. Shirane *et al.*, Gene expression levels of beta4-galactosyltransferase 5 correlate with the tumorigenic potentials of B16-F10 mouse melanoma cells. *Glycobiology* **24**, 532-541 (2014).
109. T. Sato, K. Furukawa, [Regulation of human beta-1,4-galactosyltransferase V gene expression in cancer cells]. *Yakugaku Zasshi* **132**, 691-697 (2012).
110. D. Canals, Y. A. Hannun, Novel chemotherapeutic drugs in sphingolipid cancer research. *Handb Exp Pharmacol*, 211-238 (2013).
111. U. K. Laemmli, Cleavage of structural proteins during the assembly of the head of bacteriophage T4. *Nature* **227**, 680-685 (1970).
112. K. Kurokawa *et al.*, Visualization of secretory cargo transport within the Golgi apparatus. *J Cell Biol* **218**, 1602-1618 (2019).
113. K. Kurokawa, M. Okamoto, A. Nakano, Contact of cis-Golgi with ER exit sites executes cargo capture and delivery from the ER. *Nat Commun* **5**, 3653 (2014).
114. J. Bielawski, Z. M. Szulc, Y. A. Hannun, A. Bielawska, Simultaneous quantitative analysis of bioactive sphingolipids by high-performance liquid chromatography-tandem mass spectrometry. *Methods* **39**, 82-91 (2006).
115. R. S. Sikorski, P. Hieter, A system of shuttle vectors and yeast host strains designed for efficient manipulation of DNA in Saccharomyces cerevisiae. *Genetics* **122**, 19-27 (1989).

Figure Legends:

Figure 1. GOLPH3 interacts with the cytosolic tails of selected GSL synthetic enzymes

(A) Pull-down experiments involving biotinylated peptides of glyco-enzymes cytosolic tails from HeLa cells lysates (top blot) or purified His-tagged GOLPH3 protein (bottom blot). The N-terminal cytosolic tail of the involved glyco-enzymes is shown on top of the blot (LxxR motif in red, biotin at the C-terminus). Immunoblotting shows affinity-captured GOLPH3 (endogenous and recombinant). (B) ITC profile for biotinylated LCS and GalT1 cytosolic tails with recombinant GOLPH3. (C) Pull-down experiments of biotinylated LCS WT and LCS mutant cytosolic tails from HeLa cells lysates (top blot) or purified His-tagged GOLPH3 protein (bottom blot). The N-terminal cytosolic tail of LCS WT and LCS mutants (mut. 1, 2) is shown on top of the blot (mutation in blue, LxxR motif in red, biotin at the C-terminus). (D) ITC profiles for biotinylated LCS WT and LCS mutants 2 cytosolic tails with recombinant GOLPH3. (E) HeLa cells expressing luminal GFP chimeras of sucrose-isomaltase (SI, green) containing the WT and mutant N-terminal cytosolic tails of LCS, were fixed and labeled for surface localized GFP (red). Cells expressing RARR-SI and LxxR/K-SI proteins shown PM staining. Quantification is reported on the right. Bar, 20 µm. (n indicated in the graph; mean ± SEM; ***p <0.001.

Figure 2. GOLPH3 drives the intra-Golgi recycling of LCS

(A) HeLa cells mock treated or GOLPH3-KD were transiently transfected with LCS-GFP_RUSH and subjected to the synchronization protocol described in **Methods**. Cells were then subjected to IF: LCS-GFP_RUSH (green), GM130 (red), and TGN46 (blue). Bar 1 µm. Quantification (right graph) by computational coalescence of line scans was carried out by normalized line scan analysis (normalization of the distances was performed considering the GM130 peak as 0, and the TGN46 peak as 1). The n indicated in the graph refers to the number of Golgi stacks analysed in each condition. (B) HeLa cells were transfected with LCS-GFP_RUSH, subjected to the synchronization protocol (see **Methods**), fixed and processed for cryoimmunolabeling with an anti-GFP antibody (15-nm gold particles) and anti-GM130 antibody (10-nm gold particles, black arrowheads) peri-Golgi vesicles containing LCS-GFP_RUSH are marked by red arrowheads. Bar 150 nm. (C, D) Quantification of the distribution of LCS-GFP_RUSH as measured by Frequency Distribution Analysis (C) and linear density (LD, in D). (n indicated in the graph; data are means ± SEM). (E) HeLa cells expressing LCS-GFP_RUSH mock or GOLPH3-KD were treated and stained as in (B). Black arrowheads indicate GM130; peri-Golgi vesicles containing LCS-GFP_RUSH are marked by red arrowheads. Quantification of LCS-GFP_RUSH distribution (right graph, linear density, LD) across the stack and in peri-Golgi vesicles. (n indicated in the graph, data are means ± SEM; *p <0.05**; p < 0.01 ; ***p <0.001). Bar 150 nm. (F) Mock and GOLPH3-KD HeLa cells co-expressing LCS-GFP_RUSH and VSV-G were subjected to the synchronization protocol described in **Methods**. Cells were then subjected to

IF: LCS-GFP-RUSH or VSV-G (green), GM130 (blue), and TGN46 (red). Quantification of the experiment was carried out by normalized line scan analysis (normalization of the distances was performed considering the GM130 peak as 0, and the TGN46 peak as 1). n indicated in the graph refers to the number of Golgi stacks analysed in each condition, individual data points and means ± SEM are shown, ***p < 0.001; ns, not significant), Bar 1 µm.

Figure 3. Vps74p recycles Mnn9p in the process of cisternal maturation

Wild-type (upper) and *vps74Δ* (lower) yeast cells expressing Mnn9-mCherry (red, Vps74p client) and Sys1-GFP (green, *trans*-Golgi marker) were observed. Representative 3D images are shown on the left. Bars, 1 µm. Middle panels show 4D (3D time-lapse) images of selected *cisternae* (boxed areas in the left panels) in wild type (upper) and *vps74Δ* (lower) yeast cells. Right graphs show relative fluorescence intensity changes of Mnn9-mCherry (red) and Sys1-GFP (green) of 11 selected cisternae in wild-type (upper) and 10 selected cisternae in *vps74*Δ (lower) yeast cells. Thick lines in the graphs show representative fluorescence intensity changes. (B) Wild-type (left) and *vps74Δ* (right) yeast cells expressing Mnn9-sfGFP (green, Vps74p client) and Vph1-mCherry (red, vacuole marker) were observed. Representative 3D images before photo-bleach are shown on the left. Bars, 10 µm. 3D images of selected cells (boxed area in the left) before (pre-bleach) and after (0min and 5 min) photobleaching Mnn9-sfGFP are shown on the right. Upper panels show merged 3D images of Mnn9-sfGFP and Vph1-mcherry. Lower panels indicate Mnn9-sfGFP localization. Fluorescence signals of Mnn9-sfGFP after photobleaching are emphasized. Outer dotted circles indicate the edges of cells. Inner dotted lines indicate vacuolar regions.

Figure 4 GOLPH3 regulates the lysosomal degradation of its clients

(A) Primary Human Fibroblasts (PHF) GOLPH3 OE, (left) or KD, (right) were fixed and processed for IF: Endogenous LCS (green), GOLPH3 (red), TGN46 or DAPI (blue). Asterisks indicate cells overexpressing or interfered for GOLPH3. Dashed lines depict cells with endogenous levels of LCS. Bar, 20 µm. Quantification of the amount of endogenous LCS (right graph) at the Golgi; data are means ± SEM; ***p <0.001). (B) HeLa GOLPH3 OE were fixed and processed for IF: Endogenous LCS (green), GOLPH3 (red), TGN46 (blue). Asterisks indicate cells overexpressing GOLPH3. Dashed lines depict cells with endogenous levels of LCS. Bar, 20 µm. Quantification of the amount of endogenous LCS (right graph) at the Golgi (data are means ± SEM; ***p <0.001). (C) GOLPH3 OE or KD HeLa cells expressing LCS-HA were fixed and processed for IF: HA (green), GOLPH3 (red). (D) Western blot of cells treated as in (C). (E) Assessment of LCS-GFP_RUSH synchronized transport in GOLPH3 OE or KD HeLa cells. Micrographs show cells at the indicated trafficking time points. Bar, 20 µm. (F) Western blot of cells treated as in (E) (n = 3). (G) Densitometric quantification of the amount of LCS-GFP-RUSH (Golgi mature band) over the time, starting from 2 hours chase, is plotted (n = 3, mean ± SD). (H) GOLPH3 OE or KD HeLa cells expressing LCS-HA were treated with bafilomycin A1 (BafA1, 10 nM) for 16 hr, fixed, and processed for IF labeling: LCS (green), LAMP1 (red), and DAPI (blue). Arrowheads indicate LCS

and LAMP1 co-localization. Bar, 20 µm. (I) Western blot of cells treated as in (H). Densitometric quantification (top panel) of the blot is plotted (n = 3, mean ± SD). (J) GOLPH3 OE or KD HeLa cells expressing the indicated HA-tagged glyco-enzymes were fixed and processed for IF. Bar, 20 µm. (K) Number of glyco-enzymes-HA positive spots per cell in GOLPH3-KD cells (upper panel) and percentage of cells with glyco-enzymes-HA in the ER in GOLPH3-OE cells (lower panel) are plotted. (n indicated in the graph; data are means ± SEM; ***p <0.001).

Figure 5. GOLPH3 controls GSL synthesis

(A) Effects of GOLPH3 KD or OE on sphingolipid levels as assessed by LC/MS of HeLa cells (n=3). The dotted red box highlights the effects on C16:0 Cer. (B) Effects of GOLPH3 GOLPH3 KD or OE on Gb3 as assessed by MALDI-MS. The Image is representative of 3 independent experiments (C) GOLPH3 KD or OE HeLa cells were processed for ShtxB an ChtxB staining followed by flow cytometry analysis. Representative flow cytometry distributions and the relative scatter plots are shown for each condition. (D) Effects of GOLPH3 KD or OE on glycosphingolipid synthetic flux as assessed by [^{3}H]-sphingosine pulse (2 hours) and chase (indicated times), lipid extraction and HPTLC separation and radioactive counting. (data are means ± SD; *p <0.05, **p <0.01, ***p <0.001.

Figure 6. GOLPH3 impacts growth signaling through LCS

(A) Cell lysates from HeLa cells KD or OE either GOLPH3 or LCS were processed for SDS-PAGE and Western blotting with antibodies aimed at evaluating the activation status of the mTOR pathway. Data are representative of at least 3 independent experiments (B) Clonogenic assay of HeLa cells in adherence. 250 HeLa cells KD for either GOLPH3 or LCS were allowed to form colonies for 10 days. Afterward, colonies were fixed and stained. (C) Soft agar colony formation assay of HeLa cells KD or OE either GOLPH3 or LCS. Colonies were stained and quantified. (n indicated in the graph; mean ± SEM; *p <0.05, ***p <0.001). (D) Protein lysates from parental HeLa (left), GCS-KO (middle), and LCS-KO (right) GOLPH3-OE HeLa cells were processed for SDS-PAGE and Western blotting with the indicated antibodies. Data are representative of at least 3 independent experiments (E) Soft agar colony formation assay of parental and LCS-KO HeLa cells expressing GFP (CTRL), LCS-HA or GOLPH3. Colony number was quantified (right graph). (n indicated in the graph; mean ± SEM; ***p <0.001). (F) Quantification of soft agar colony formation assay of LNCaP and DU145 prostatic cancer cell lines treated with increasing concentrations of siRNA targeting GOLPH3 or LCS. (n indicated in the graph; mean ± SEM; ***p <0.001)

Figure 7. GOLPH3 and LCS protein levels correlate in NSCLC tissue samples

Surgical specimens were collected from 72 non-small cells lung cancer (NSCLC) patients. In (A) age at surgery and sex distribution of the patients are reported. Data are depicted as a box plot. (B) Copy number (CN) variations in *GOLPH3* gene were assessed in cancer tissue section by DNA FISH as described in Methods and are expressed as a pie chart. (C) Cancer tissue sections were processed for IHC using antibodies against endogenous GOLPH3 and LCS. The

IHC intensity of the staining for each section and for both the tested proteins was classified according to the criteria described in **Methods**. A contingency table for the GOLPH3 and LCS staining is reported. (D) Representative images of NSCLC sections stained for GOLPH3 and LCS.

Figure 1

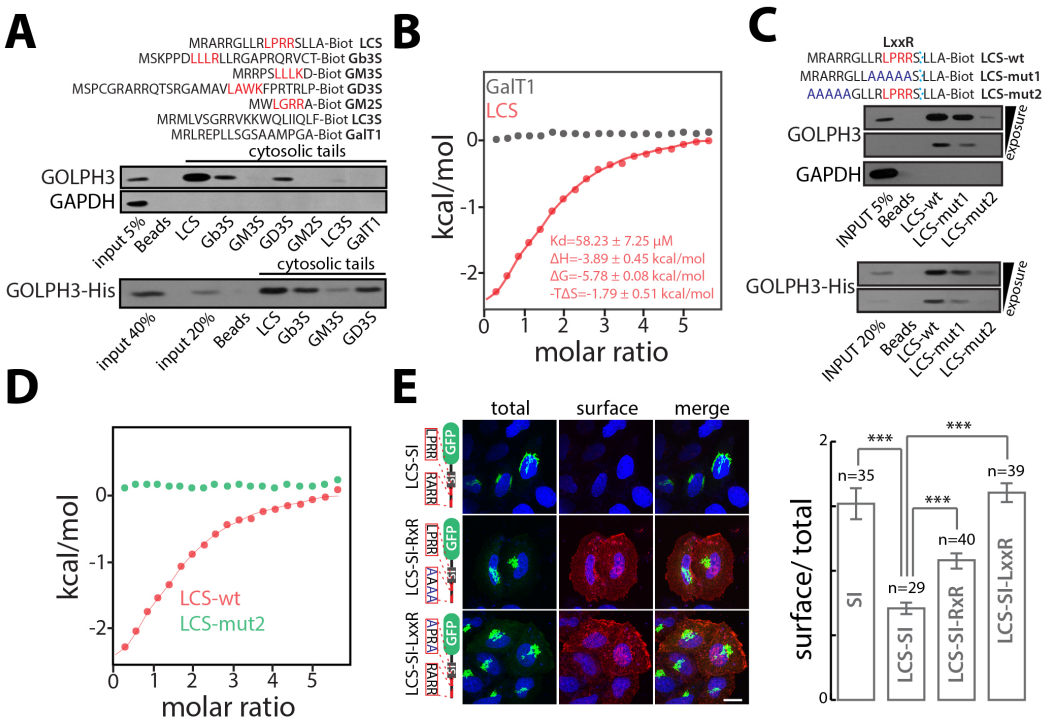
A
MRARRGLLRLPRRSLLA-Biot LCS
MSKPPDLLLRLLRGAPRQRVCT-Biot Gb3S
MRRPSLLLKD-Biot GM3S
MSPCGRARRQTSRGAMAVLAWKFPRTRLP-Biot GD3S
MWLGRRA-Biot GM2S
MRMLVSGRRVKKWQLIIQLF-Biot LC3S
MRLREPLLSGSAAMPGA-Biot GalT1
cytosolic tails
GOLPH3
GAPDH
input 5%
Beads
LCS
Gb3S
GM3S
GD3S
GM2S
LC3S
GalT1
cytosolic tails
GOLPH3-His
input 40%
input 20%
Beads
LCS
Gb3S
GM3S
GD3S
B
GalT1
LCS
kcal/mol
molar ratio
Kd=58.23 ± 7.25 μM
ΔH=-3.89 ± 0.45 kcal/mol
ΔG=-5.78 ± 0.08 kcal/mol
-TΔS=-1.79 ± 0.51 kcal/mol
C
LxxR
MRARRGLLRLPRRSLLA-Biot LCS-wt
MRARRGLLAAAAASLLA-Biot LCS-mut1
AAAAAGLLRLPRRSLLA-Biot LCS-mut2
GOLPH3
GAPDH
exposure
INPUT 5%
Beads
LCS-wt
LCS-mut1
LCS-mut2
GOLPH3-His
exposure
INPUT 20%
Beads
LCS-wt
LCS-mut1
LCS-mut2
D
kcal/mol
molar ratio
LCS-wt
LCS-mut2
E
total
surface
merge
LCS-SI
LCS-SI-RxR
LCS-SI-LxxR
GFP
surface/ total
n=35
n=29
n=40
n=39
***
***
***
SI
LCS-SI
LCS-SI-RxR
LCS-SI-LxxR

Figure 2

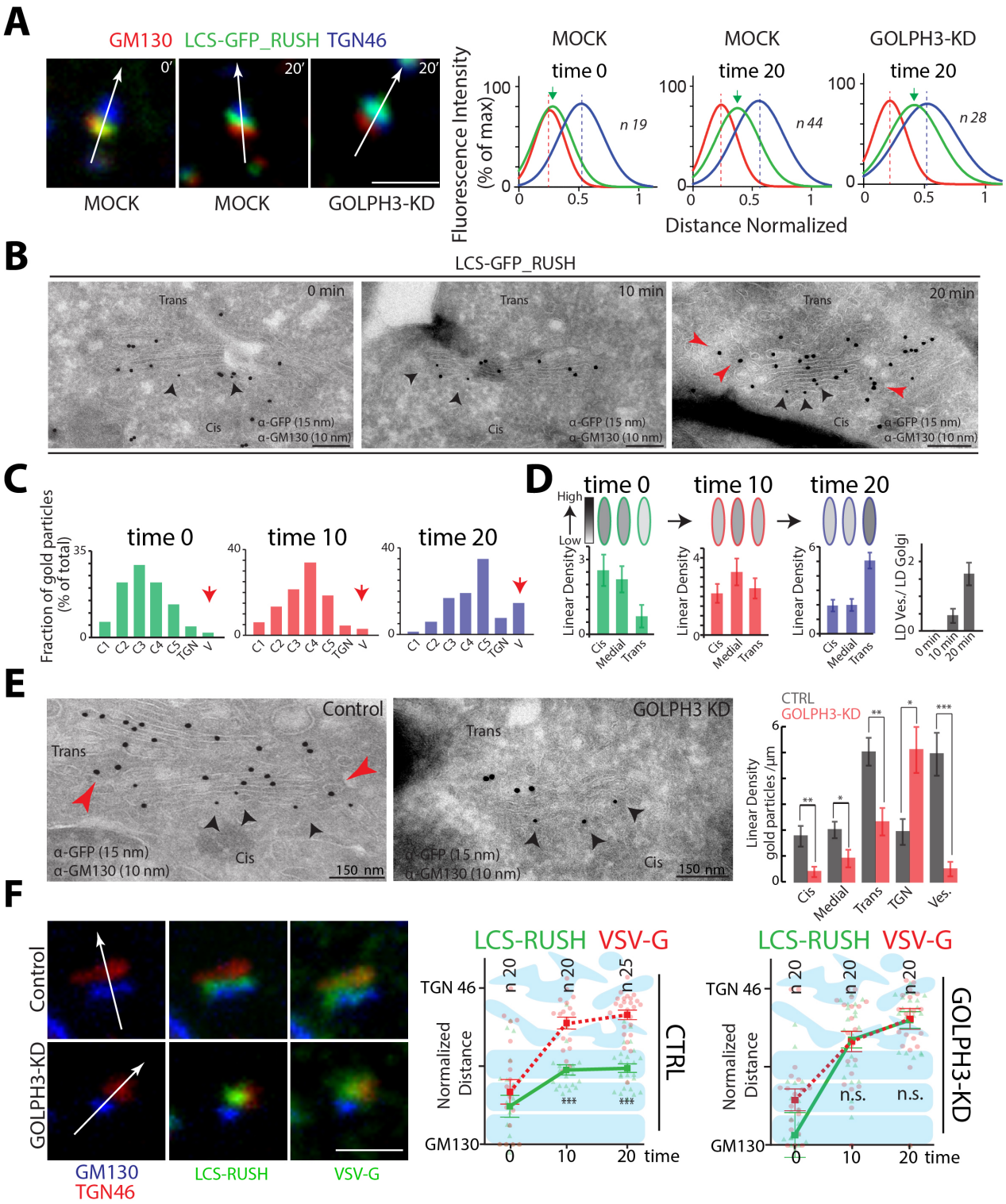
A
GM130 LCS-GFP_RUSH TGN46
0′
20′
20′
MOCK
MOCK
GOLPH3-KD
MOCK time 0
MOCK time 20
GOLPH3-KD time 20
Fluorescence Intensity (% of max)
n 19
n 44
n 28
Distance Normalized
B
LCS-GFP_RUSH
0 min
10 min
20 min
Trans
Cis
α-GFP (15 nm)
α-GM130 (10 nm)
C
Fraction of gold particles (% of total)
time 0
time 10
time 20
C1 C2 C3 C4 C5 TGN V
D
time 0
time 10
time 20
High
Low
Linear Density
Cis Medial Trans
LD Ves./ LD Golgi
0 min 10 min 20 min
E
Control
GOLPH3 KD
Trans
Cis
α-GFP (15 nm)
α-GM130 (10 nm)
150 nm
CTRL
GOLPH3-KD
Linear Density gold particles /µm
Cis Medial Trans TGN Ves.
F
Control
GOLPH3-KD
GM130
TGN46
LCS-RUSH
VSV-G
LCS-RUSH VSV-G
TGN 46
GM130
Normalized Distance
n 20
n 20
n 25
CTRL
n 20
n 20
n 20
GOLPH3-KD
n.s.
n.s.
0 10 20 time

Figure 3

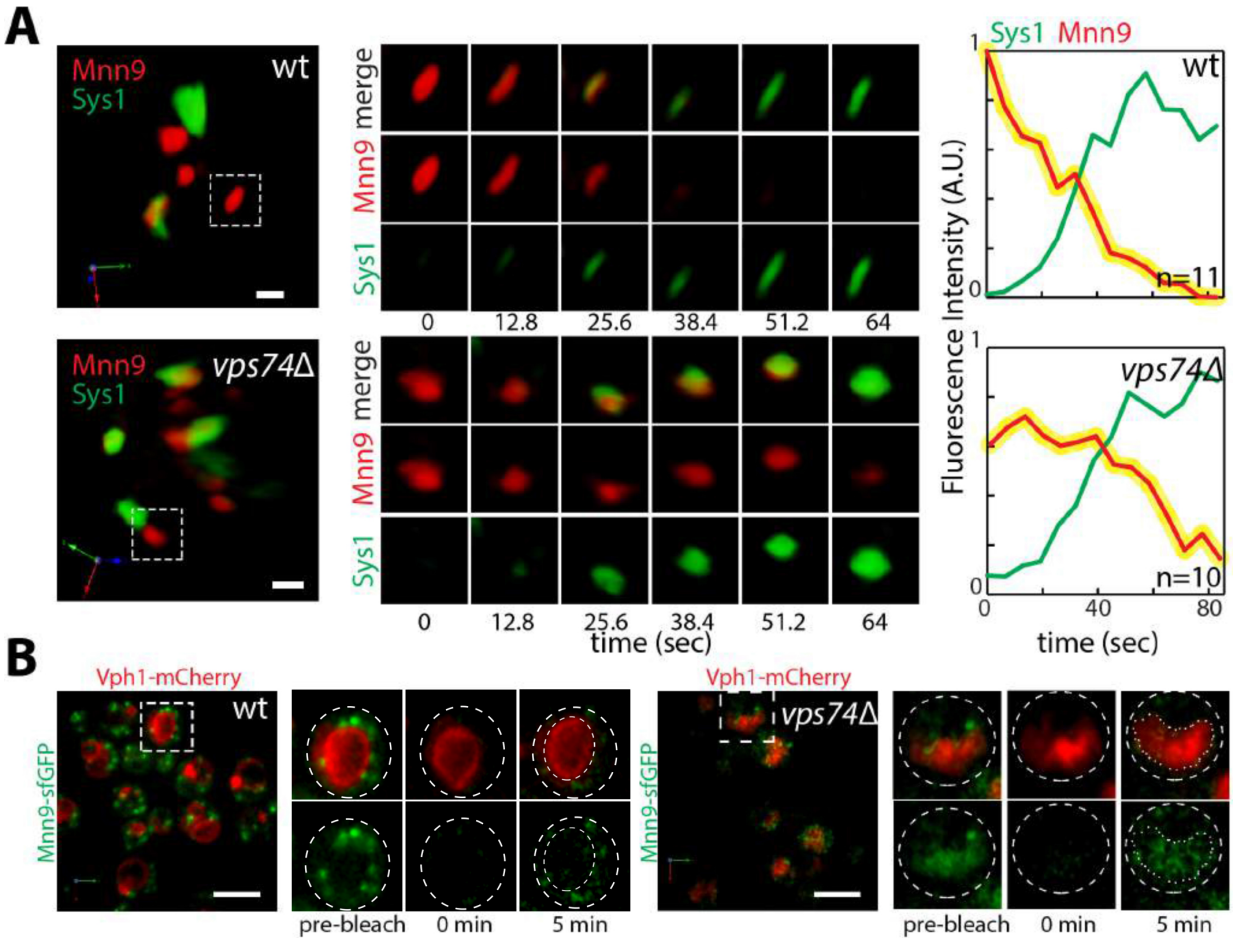
A
Mnn9
Sys1
wt
merge
Mnn9
Sys1
0
12.8
25.6
38.4
51.2
64
vps74Δ
time (sec)
Sys1 Mnn9
Fluorescence Intensity (A.U.)
n=11
n=10
0
40
80
B
Vph1-mCherry
Mnn9-sfGFP
pre-bleach
0 min
5 min

Figure 4

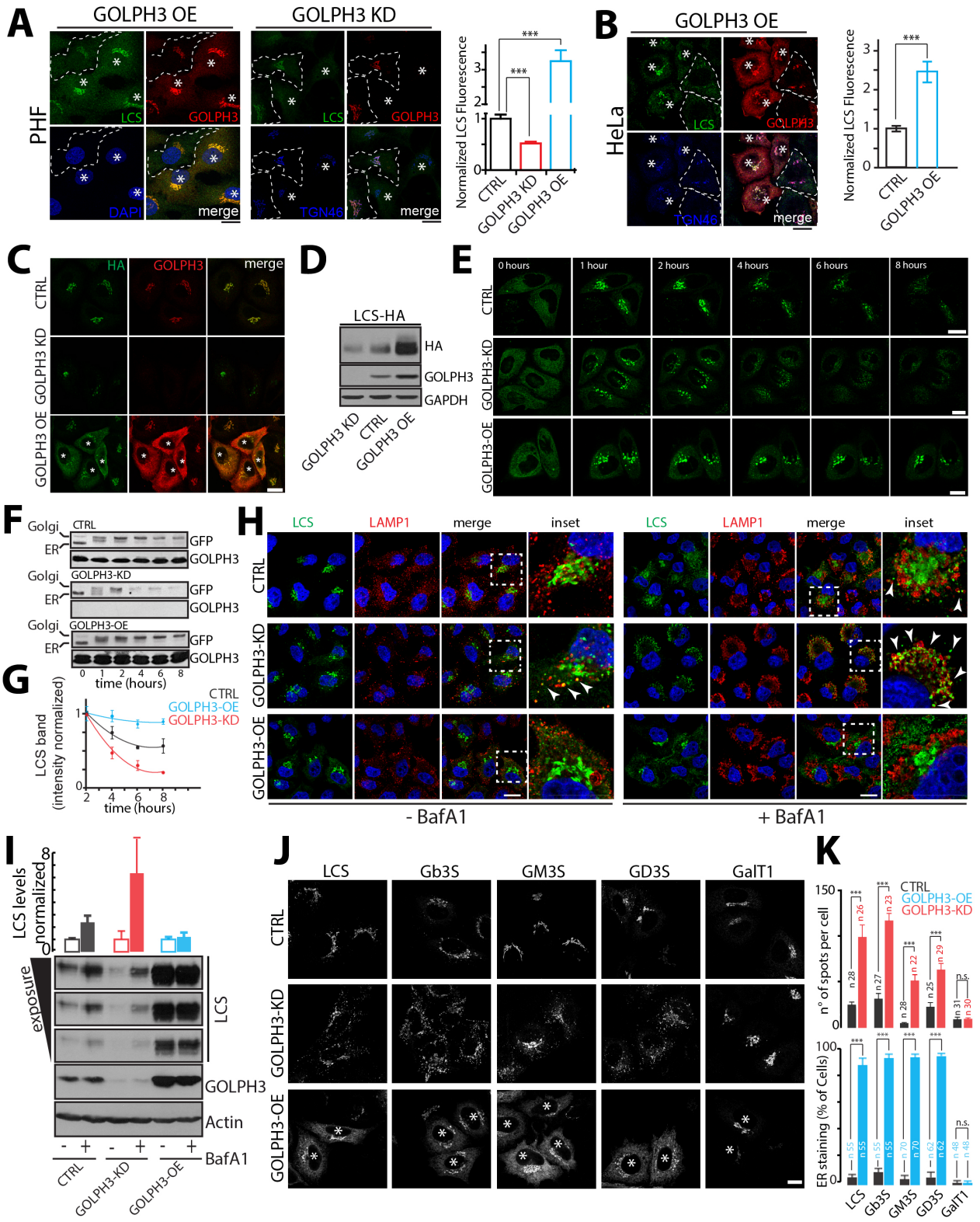
A
GOLPH3 OE
GOLPH3 KD
PHF
LCS
GOLPH3
DAPI
merge
TGN46
Normalized LCS Fluorescence
CTRL
GOLPH3 KD
GOLPH3 OE
B
HeLa
C
HA
D
LCS-HA
GAPDH
E
0 hours
1 hour
2 hours
4 hours
6 hours
8 hours
GOLPH3-KD
GOLPH3-OE
F
Golgi
ER
GFP
time (hours)
G
LCS band (intensity normalized)
H
LAMP1
inset
- BafA1
+ BafA1
I
LCS levels normalized
exposure
BafA1
J
Gb3S
GM3S
GD3S
GalT1
K
n° of spots per cell
ER staining (% of Cells)
n.s.

Figure 5

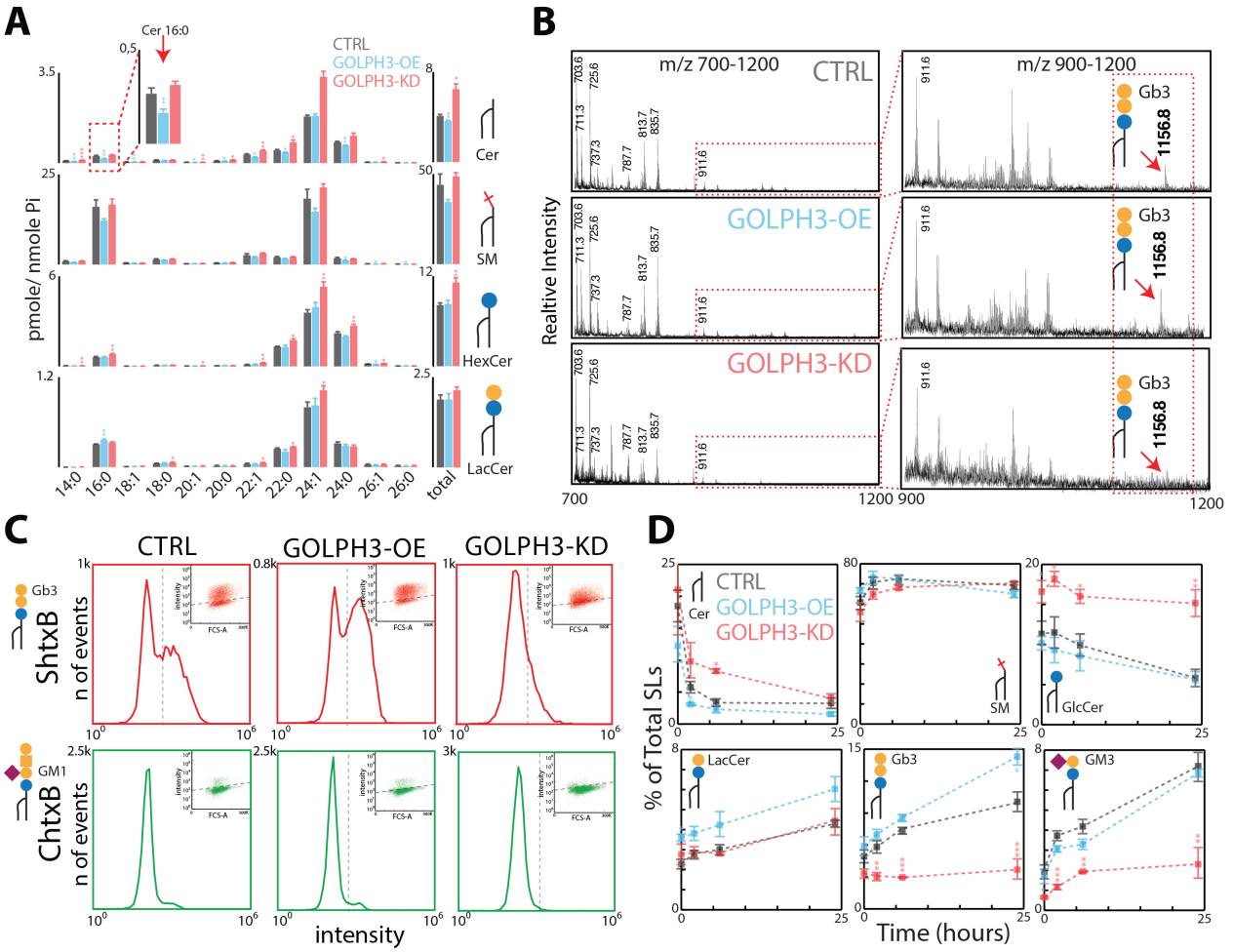
A
Cer 16:0
CTRL
GOLPH3-OE
GOLPH3-KD
pmole/ nmole Pi
Cer
SM
HexCer
LacCer
14:0
16:0
18:1
18:0
20:1
20:0
22:1
22:0
24:1
24:0
26:1
26:0
total
B
m/z 700-1200
m/z 900-1200
CTRL
GOLPH3-OE
GOLPH3-KD
Realtive Intensity
Gb3
1156.8
C
CTRL
GOLPH3-OE
GOLPH3-KD
Gb3
ShtxB
GM1
ChtxB
n of events
intensity
D
CTRL
GOLPH3-OE
GOLPH3-KD
Cer
SM
GlcCer
LacCer
Gb3
GM3
% of Total SLs
Time (hours)

Figure6

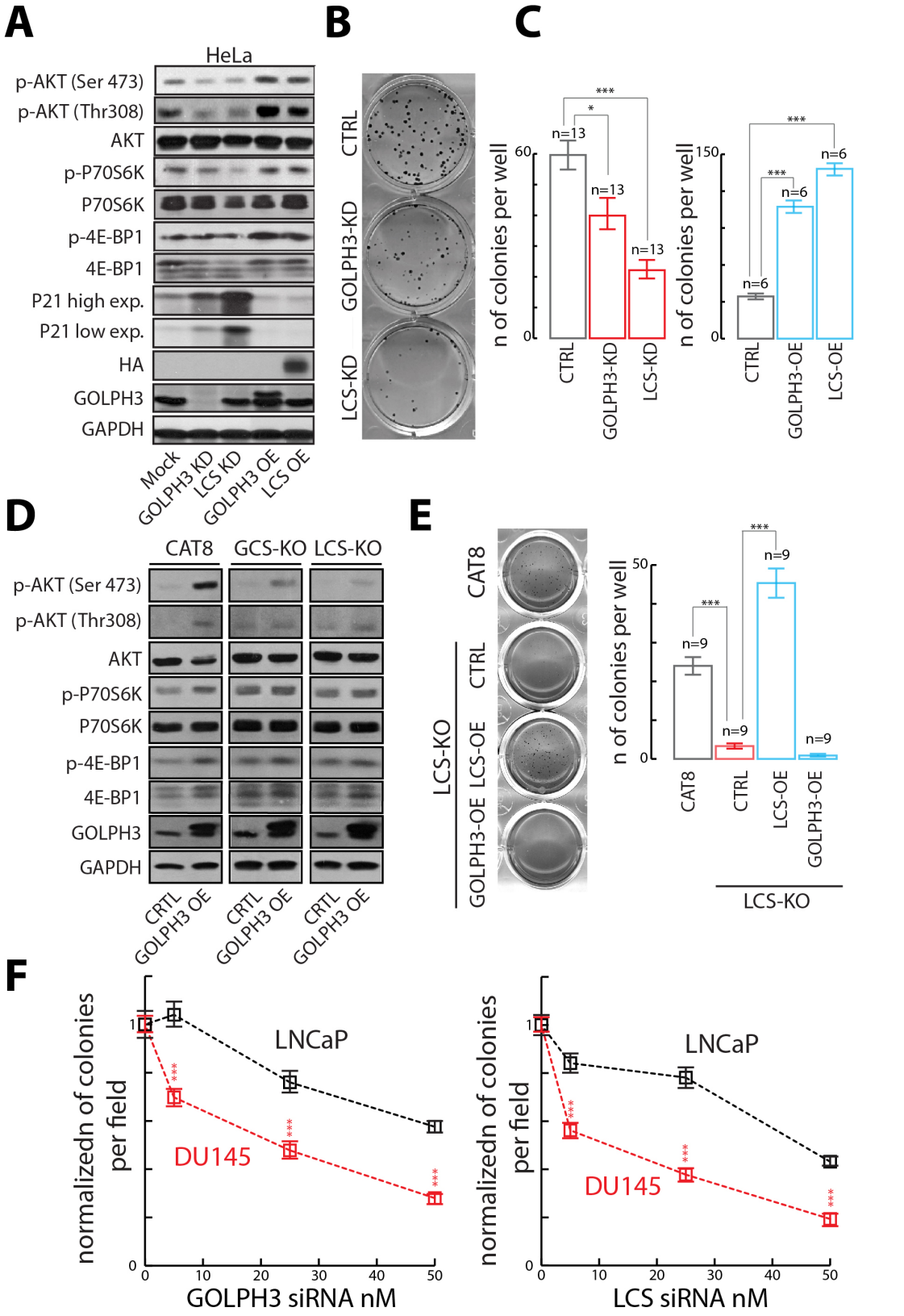
A
HeLa
p-AKT (Ser 473)
p-AKT (Thr308)
AKT
p-P70S6K
P70S6K
p-4E-BP1
4E-BP1
P21 high exp.
P21 low exp.
HA
GOLPH3
GAPDH
Mock
GOLPH3 KD
LCS KD
GOLPH3 OE
LCS OE
B
CTRL
GOLPH3-KD
LCS-KD
C
n of colonies per well
n=13
n=13
n=13
CTRL
GOLPH3-KD
LCS-KD
n=6
n=6
n=6
GOLPH3-OE
LCS-OE
D
CAT8
GCS-KO
LCS-KO
CRTL
GOLPH3 OE
E
CAT8
CTRL
LCS-KO
LCS-OE
GOLPH3-OE
n=9
n=9
n=9
n=9
F
normalizedn of colonies per field
LNCaP
DU145
GOLPH3 siRNA nM
LCS siRNA nM

Figure 7

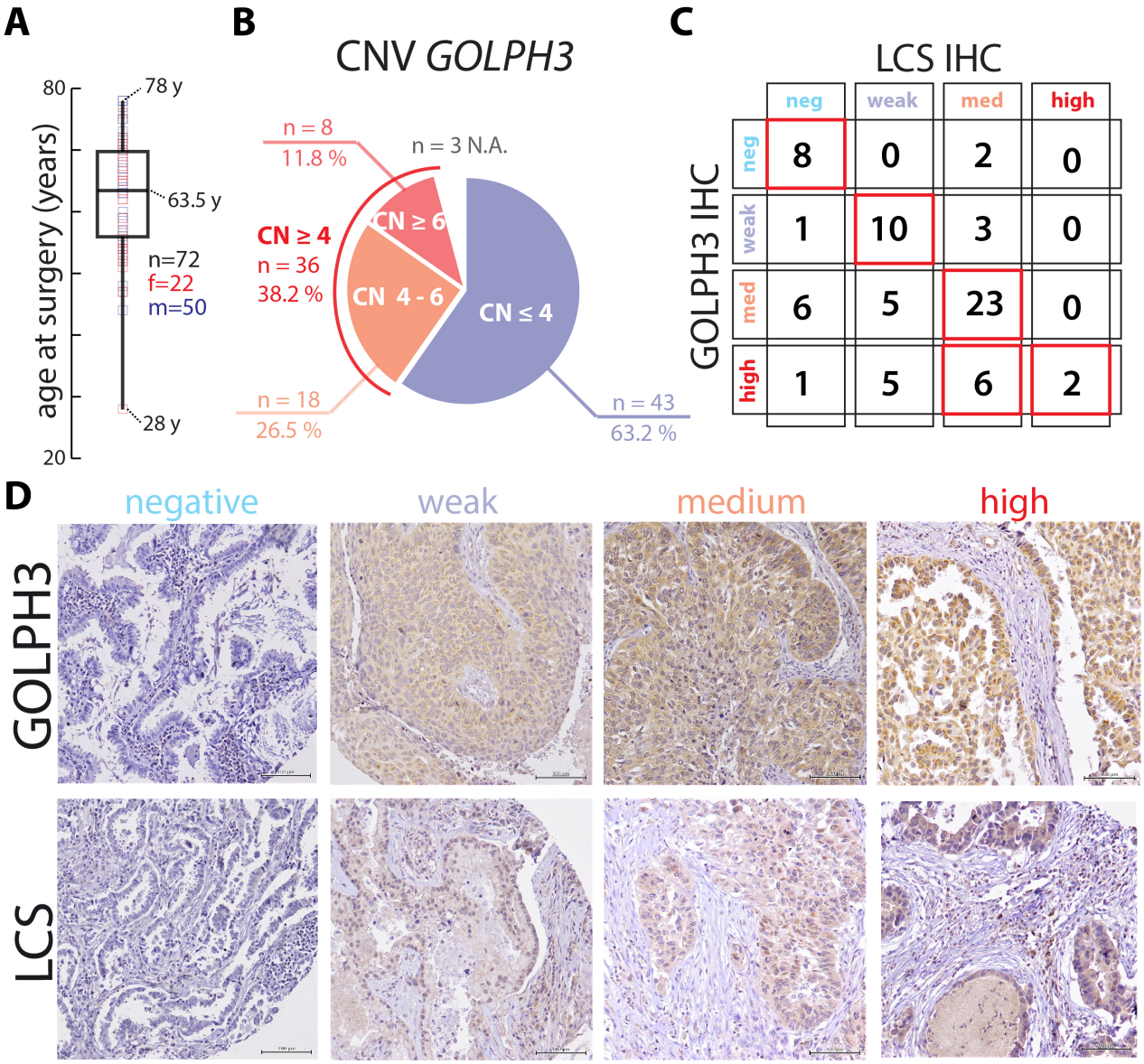
A
80
20
age at surgery (years)
78 y
63.5 y
28 y
n=72
f=22
m=50
B
CNV GOLPH3
n = 8
11.8 %
n = 3 N.A.
CN ≥ 4
n = 36
38.2 %
CN ≥ 6
CN 4 - 6
CN ≤ 4
n = 18
26.5 %
n = 43
63.2 %
C
LCS IHC
neg
weak
med
high
GOLPH3 IHC
neg 8 0 2 0
weak 1 10 3 0
med 6 5 23 0
high 1 5 6 2
D
negative
weak
medium
high
GOLPH3
LCS

Supplementary Material

Methods

Contact for Reagents and Resource Sharing

Further information and requests for resources and reagents should be directed to and will be fulfilled by the Lead Contacts: Alberto Luini (a.luini@ibp.cnr.it) and Giovanni D'Angelo (giovanni.dangelo@epfl.ch).

Cell lines and culture conditions.

HeLa-M (human cervical cancer cells, female origin) were obtained from the ATCC. DU145 (prostate cancer cells, human male origin) were a kind gift from Carmen Valente from the Institute of Biochemistry and Cell Biology, CNR, Naples. LNCaP cells (prostate cancer cells, human male origin) were a kind gift from Alfredo Budillon from the Istituto Nazionale Tumori "Fondazione Pascale". HeLa-M, DU145 and LNCaP cells were cultured in RPMI-1640 medium containing 4.5 g/L glucose, 2 mM L-glutamine, 10% fetal calf serum (FCS), and 100 U/mL penicillin and streptomycin. Primary human fibroblasts (PHFs) (normal cells, male origin) were obtained from the Telethon Biobank. The HeLa-mCAT#8 (including TALEN UGCG-KO, and LCS-KO) cell lines (human cervical cancer cells, female origin) were kind gifts from Kentaro Hanada ((*67*)). Primary human fibroblasts, HeLa-mCAT#8, UGCG-KO, and LCS-KO were cultured in DMEM containing 4.5 g/L glucose, 2 mM L-glutamine, 10% FCS, and 100 U/mL penicillin and streptomycin. Cells were grown under controlled temperature and atmosphere.

METHOD DETAILS

Plasmids and siRNA transfection.

HeLa cells and PHFs were transfected with Mirus or Lipofectamine® LTX transfection reagents following the manufacturer's instructions (1% FCS in HF medium). Oligofectamine was used for siRNA transfection and performed according to manufacturer's instructions (used at concentrations between 5 and 50 nM for the target gene). Each individual siRNA in the pool was also tested in localization and signaling experiments. The list of siRNA sequences can be found in **Table S2**.

Biotinylated peptides

The C-terminally biotinylated peptides corresponding to the tails of Golgi enzymes, were synthetized by Dr. Petra Henkein, Charité - Universitätsmedizin Berlin. Their list and sequences can be found in **Table S3**.

Generation of constructs and mutants.

The GOLPH3 siRNA-resistant construct was generated by site-directed mutagenesis. The oligonucleotide primers used for the mutagenesis reaction were: F5′-gggcctcaaggaccgagagggatacacttcattttggaatgac-3′ and R5′-gtcattccaaaatgaagtgtatccctctcggtccttgaggccc-3′. The oligos were ordered for creating siRNA-1# resistant GOLPH3 by changing the nucleotide sequence, but not the codon sequence. The primers were chosen with melting points above 78 °C, and were self-complementary and PAGE-purified. The GOLPH3 cDNA was cloned in pCMV6-XL5 vector (Origene). Pfu Turbo DNA polymerase was used to insert and amplify the 3-point-mutagenized GOLPH3 sequence, amplifying for 18 cycles at 56 °C and extending the mutagenized DNA 16 min at 68 °C at each cycle. The parent strand was digested with DpnI treatment for 60 min at 37 °C. The final product was precipitated, resuspended in 10 mM Tris, pH 8.0, used to transform TOP10 competent cells, and selected on LB + Amp agar. Minipreps were prepared (QIAprep spin miniprep kit, Qiagen) and the sequence was confirmed with internally designed primers: GF: 5′-atgacctcgctgacccag-3′ and GR: 5′-cttggtgaacgccgccac-3′. The GOLPH3 binding pocket single point mutant R90L was generated by site-directed mutagenesis. The oligonucleotide primers used for the mutagenesis reaction were: R90LF5′-ctgtatatcatctggattacttggctgtatgttaattgaattagc-3′ and R90LR:5′-gctaattcaattaacatacagccaagtaatccagatgatatacag-3′. The oligos were ordered for creating a single point mutant in the binding pocket of GOLPH3. The primers were chosen with melting points above 78 °C, and were self- complementary and PAGE-purified. Mutagenesis, minipreps, and sequencing were performed as described above.

The B4GALT5-Myc (a kind gift from Antonella De Matteis) was used as a template to generate B4GALT5-HA (LCS-HA) cDNA using F5′-gcgcgcgaattcatgcgcgcccgccg-3′ and R5′-cgcgcgctcgag ttaagcgtaatctggaacatcgtatgggtagtactcgttcacctgagccag-3′ primers. Oligos forward and reverse (incorporating a 3′ HA tag) were used for amplifying 50 ng *B4GALT5* cDNA with 1U Phusion polymerase (NEB) in GC Buffer for 30 cycles on an MJ REsearch Peltier Thermal Cycler, annealing at 70 °C to maintain specificity. The PCR fragment was cleaned using the QIAquick PCR purification kit (Qiagen) and cut with EcoRI/XhoI, re-cleaned with the QIAquick PCR purification kit, ligated into EcoRI/XhoI-cut pcDNA4b for 2 hr at room temperature, and plated on LB + amp agar. Minipreps were prepared (QIAprep spin miniprep kit) and sequence confirmed using T7 and BGH rev primers by PRIMM.

RNA extraction and real-time qPCR.

After treatment, total RNA was isolated from cells using RNeasy Mini kits (Qiagen) following the manufacturer's instructions. The quality and quantity of RNA was determined by NanoDrop 2000c spectrophotometer (Thermo Scientific) and TAE agarose gel electrophoresis, respectively. Total RNA was reverse-transcribed to cDNA using the QuantiTect Reverse Transcription Kit (Qiagen) and subjected to real-time qPCR using specific primers for the target genes of interest in the presence of LightCycler® 480 SYBR Green I Master Mix (Roche) on a LightCycler® 480 II detection system (Roche). Hypoxanthine phosphoribosyltransferase 1 (HPRT1) was used as the reference gene and the variations in the expression levels of target

genes were determined and expressed as fold changes respect to the control, using the comparative CT method (ΔΔCT Method). The list and sequences primers used in this study can be found in **Table S4.**

Western blotting.

After treatment, the cells were washed three times with PBS and lysed in RIPA buffer (150 mM NaCl, 1% Triton X-100, 0.5% deoxycholic acid, 0.1% SDS, 20 mM Tris-HCl, pH 7.4), supplemented with protease and phosphatase cocktail inhibitor (Roche). The lysates were clarified by centrifugation, quantified using a BCA Protein Assay kit (Pierce), and resolved by SDS-PAGE and immunoblot. Blots were incubated with ECL for 3 min and exposed to x-ray films, which were then scanned. The intensity of the bands was quantitated using ImageJ.

Immunoprecipitation and peptide pull down assay.

For co-immunoprecipitation experiments, HeLa cells were transfected with LCS-HA, cultured for 24 hr and then lysed on ice with immunoprecipitation buffer (150 mM NaCl, 1% Igepal, 20 mM Tris-HCl, pH 7.4, protease inhibitors). The lysate was cleared and quantitated using the BCA Protein Assay kit (Pierce). Equal amounts of proteins were incubated with magnetic beads conjugated with anti-HA antibody (Sigma) overnight at 4 C. Then, the samples were washed extensively with immunoprecipitation buffer, eluted with HA peptide (Sigma), and analyzed by SDS-PAGE and immunoblotting with anti-HA and anti-GOLPH3 antibodies (see **Table S5**).
Biotinylated N-terminal amino acid tails of Golgi enzymes were resuspended in 150 mM NaCl and 20 mM Tris pH 7.4. For each sample, between 1 and 5 µg of peptide was incubated with 40 µL of pre-washed monomeric avidin beads (Pierce) and incubated 1 hr at 4 °C. Beads functionalized with CTs were mixed with 500 µg of HeLa cell lysate (lysis buffer contains 150 mM NaCl, 20 mM Tris HCl pH 7.4, 0.1 % triton X-100, 1 mM DTT, protease and phosphatase inhibitors, and 5 mM EDTA) or 5 µg of purified ΔGOLPH3-His and incubated overnight at 4 °C. Then, the samples were washed extensively with lysis buffer and analyzed by SDS-PAGE and immunoblotting with anti-His or anti-GOLPH3 antibody (see **Table S5**).

GAG Secretion assay

After treatment Hela cells were washed with Tyrode's solution (Tyrode: 125 mM NaCl, 5 mM KCl, 5.6 mM glucose, and 20 mM HepesNaOH, pH 7.2) containing 1.8 mM each CaCl2 and MgCl2 (Tyrode/ Ca1Mg) and incubated 15 min at 37 °C in 1 ml of the same buffer with or without 1 mM xyloside to label free glycosaminoglycan chains (GAG) or proteoglycans, respectively. The buffer was then substituted with 0.6 ml of Tyrode/Ca1Mg containing 80 –150 mCi/ml [35S] sulfate, and the incubation continued for 5 min at 37 °C. Cells were washed with serum free RPMI and then incubated in 0.6 ml of the same medium for 30 minutes. Released media were collected and centrifuged (12,000g for 10 min), and the supernatant was recovered. Cell monolayers were extracted with 0.5 ml of 0.1 M NaOH for at least 30 min at 37 °C. Cell supernatants and extracts (0.5ml) were precipitated overnight at room temperature by the addition of chondroitin sulfate (0.6% final concentration) and cetylpyridinium chloride (1%

final concentration). Precipitates were collected by centrifugation (2600 g for 10 min) and washed twice with 1% cetylpyridinium chloride in 20 mM NaCl. Finally, pellets were dissolved in 2 M NaCl at 37 °C and radioactivity measured in a scintillation counter using Beckman Ultima Gold XR. Total counts were normalized to total amount of proteins.

Immunofluorescence and confocal microscopy.

Cells grown on coverslips were fixed with 4% paraformaldehyde and permeabilized with 0.2% saponin (as described in (*12*)). Samples were then incubated with selected antibodies against the antigen of interest at 4 °C overnight followed by second antibodies labeled with Alexa Fluor dyes (Invitrogen). The coverslips were then mounted and analyzed under a confocal microscope (LSM700; Carl Zeiss; 40x or 63× oil-immersion objective (1.4 NA)). Images were processed using Metamorph 7.7.3.0 (Universal Imaging) and ImageJ software. Excel and GraphPad Prism version 5.0 software were used for data analyses and graphing. Adobe Photoshop CS3 was used to adjust the contrast of the images (for presentation only), whereas Adobe Illustrator CC 2014 (Adobe Systems) was used to illustrate figures and draw models.

Live cell imaging.

For live cell imaging, HeLa-M cells transiently expressing LCS-GFP_RUSH or PH-Akt-GFP, which were grown on glass-bottomed 35-mm dishes which were then mounted on a Zeiss LSM700 laser scanning microscope under controlled temperature and CO_2. The images were acquired at regular interval (488 for excitation; PMT: 510–550 nm; 512×512 pixels; frame average, 4).

Immuno-electron microscopy

The samples were fixed and processed as described previously (Rizzo et al., 2013). In brief, HeLa cells were fixed with 4% paraformaldehyde and 0.05% gluteraldehyde for 30 min at room temperature, then washed with PBS/0.02 M glycine and embedded in 12% gelatin in PBS. Small blocks (1 mm) were obtained and infiltrated with 2.3 M sucrose at 4 °C. Ultrathin cryosections (50–70 nm) were prepared using a UC7 Leica cryo-ultramicrotome and incubated with indicated antibodies of interest followed by protein A gold. Random sampling of Golgi stacks was performed using a Tecnai-12; FEI transmission electron microscope, and pictures were acquired using a Veletta CCD digital camera. Morphological (clathrin at the TGN) and compositional (cis Golgi marker GM130) criteria were used to define the polarity of the Golgi stacks. For quantitation (performed with iTEM image acquisition software), cis, medial, or trans Golgi were defined as previously described (*46*). Cis indicated the cis-most cisterna in the case of a stack with three or four cisternae, and the two cis-most cisternae in the case of a stack with five cisternae (here, the LD was the mean of the two). Trans was the last (trans) cisterna. Medial was the remaining one or two central cisternae. Vesicles were round profiles of 50–80 nm in diameter, present within 200 nm of the rims of the stack. The distribution of LCS-HA, GalT1 and GOLPH3 within the Golgi stacks was expressed as linear density (LD), which represents the number of gold particles/µm.

GOLPH3 cloning into pT-7.7 and pCDNA4B.

To clone GOLPH3 into the pT-7.7 expression vector, residues 1–57 were substituted with a 6xHis-tag and the fragment was amplified using vector/GOLPH3 as a template, recombinant Taq DNA polymerase High Fidelity (Vent DNA polymerase; NEB, UK), and oligonucleodides 5′-GOLPH3His (5′-actttaagaaggagatatacatatgcatcatcatcatcatcataccaggctgaccctga-3′) and 3′-GOLPH3Stop (5′-caggtcgactctagaggatccttacttggtgaacgccgc-3′), as forward and reverse primer (over-lapping ends with the destination vector indicated in bold), in a 35-cycle PCR (95 ℃; 30 sec, 48 ℃; 30 sec, 72 ℃; 1 min). Primers were designed to clone GOLPH3 in-frame with the expression elements of the vector. z, the PCR product was used as a mega-primer in a second PCR for gene cloning. The RF reactions were as follows: a single denaturation step (95 ℃, 5 min) was performed followed by 20 cycles PCR (95 °C, 1 min; 50 °C, 30 s; 72 °C, 5 min), and a final elongation step of 10 min at 72 ℃. RF reactions were performed in a final volume of 50 µL including the following components: 50 ng of target DNA, 500 ng of PCR product (mega-primers), 200 µM of each dNTP, 1x Pfu buffer, and 5U Pfu Turbo Cxhotstart DNA polymerase (Agilent). A 30 µL aliquot of each PCR mix was digested using 20 U DpnI (NEB, UK) (37 ℃, 1 hr), to digest the parental plasmid DNA, and 20 µL of each aliquot was used to transform Escherichia coli Top10 strain (Invitrogen). The same procedure was used to clone GOLPH3-℃℃57 into pCDNA4B, with forward and reverse oligonucleotides 5′-GOLPH3pCDNA4B (5′-GCTTGGTACCGAGCTCGGATCCATGACCAGGCTGACCCTGATGGAGGAAG-3′) and 3′-GOLPH3pCDNA4B (5′-ACTGTGCTGGATATCTGCAGAATTCTTACTTGGTGAACGCCGCCACCA-3′), respectively (ends overlapping with the destination vector in bold). Colony PCR screening was used to search positive clones. The cloned fragments were completely sequenced to verify that during the amplification procedure undesired mutations had not been introduced.

GOLPH3 over-expression and purification.

Protein expression was performed in 2 L LB medium containing 100 µg/mL ampicillin at 37 ℃; when the cell culture reached the optical density (OD) of 0.6 (at 600 nm) protein expression was induced by IPTG (0.5 mM). After 2 hr, cells were harvested by centrifugation (3,000 x g, 4 ℃, 10 min). All subsequent procedures were carried out at room temperature, unless otherwise indicated. Wet frozen cells (10 g) were thawed and dissolved in 50 mL buffer containing 20 mM phosphate pH 7.5; 50 mM NaCl; and protease inhibitor cocktail (Sigma-Aldrich). Cell disruption was obtained by ultrasound apparatus (Branson), using 5 cycles at 40 % power for 30 sec. Cell debris was removed by centrifuging (30,000 x g, 4 ℃, 20 min). Then, 2 mL of Ni-NTA resin (Qiagen) was added to the soluble fraction and incubated for 16 hr at 4 ℃ under gentle stirring. To reduce non-specifically bound proteins to the resin, imidazole was added at final concentration of 10 mM. The resin was loaded onto a column (20 mL), then washed with 20 mL phosphate buffer containing NaCl and imidazole (10 mM); two additional wash steps were performed by using phosphate buffer containing imidazole at 20 and 50 mM and eluted with phosphate buffer containing 200 mM imidazole; the sample was recovered in fractions of 1 mL. Fractions were pooled (about 10 mL total volume), concentrated by ultrafiltration onto a 10,000 cut-off cellulose membrane (Amicon) to 4 mL, divided in 2 mL

aliquots, and loaded onto a Hi- Load 16/60 Superdex 75 column (GE Healthcare). The column was equilibrated and eluted with 20 mM phosphate buffer containing 50 mM NaCl and 5 mM imidazole. The flow rate was 0.5 mL/min. The presence of Golgh3 was monitored by SDS-PAGE; fractions containing the protein were pooled and concentrated by ultrafiltration up to 2 mL; 2 mg pure enzyme was purified from 10 g of frozen cells.

Electrophoretic analysis.

SDS-PAGE analysis (12.5%) was performed as described by (*111*), at room temperature. The "10 kDa-250 kDa Precision plus protein standard" (Bio Rad) was used as a molecular weight standard.

Soft agar assay.

Soft-agar assays were performed on 12-well plates in triplicate. For each well, 1 x 104 cells were mixed thoroughly in cell growth medium containing 0.3% agarose (Invitrogen, 16500-500) in DMEM plus 10% FCS, 1% penicillin/streptomycin, and 0.5 mM sodium pyruvate, followed by plating onto bottom agarose prepared with 0.6% agarose in DMEM and 10% FCS. The wells were allowed to solidify and 200 µL of growth medium was added on top and refreshed every 4 or 5 days to avoid agar drying. After 10–30 days, depending on the cell line, colonies were stained with nitrotetrazolium blue chloride (Sigma N6876), scanned, and counted using ImageJ.

Flow cytometric analysis.

After treatment, HeLa cells were subjected to trypsin digestion, fixed with 4% paraformaldehyde, washed, and resuspended with PBS. To visualize cell-surface-specific carbohydrates, cells were incubated with bacterial toxins or lectins for 1 hr at 4 °C. Then, cells were extensively washed with PBS and incubated with fluorescence-labeled secondary antibodies when required, or directly analyzed by BD FACS ARIAIII cell sorter (BD Biosciences). Cells incubated with secondary antibody alone, or unlabeled cells, were used as a negative control. The cell-surface expression of sugars and GSLs of selected cells were further analyzed in the gated region. Antibodies, lectins and toxins used are described in (**Table S5**).

Yeast strains, plasmids and culture conditions

Yeast strains and primers used in this study are listed in the tables. Yeast Strains expressing Mnn9-mCherry, Mnn9-sfGFP, Vph1-sfGFP, Vph1-mCherry were constructed by a PCR-based method using pFA6a plasmids as a template (*112*) (primers 5'-atttggcttaccaaactatttggtttatcacatagaggaagagaaccatcggatccccgggttaattaa-3' and 5'-attatctttcaataacgctatagcttctgtatgctttttgctcagttgcgaattcgagctcgtttaaac-3' for Mnn9-mCherry and Mnn9-sfGFP and primers 5'-ataaagacatggaagtcgctgttgctagtgcaagctcttccgcttcaagccggatccccgggttaattaa-3' and 5'-tatttaatgaagtacttaaatgtttcgctttttttaaaagtcctcaaaatgaattcgagctcgtttaaac-3' for Vph1-mCherry

and Vph1-sfGFP). Sys1-GFP and Sec7-GFP were expressed under the control of the *ADH1* promoter on the low-copy plasmid pRS316 (*112*).

Live cell imaging of yeast

Yeast cells were grown in MCD medium [0.67% yeast nitrogen base without amino acids (Difco Laboratories Inc.), 0.5% casamino acids (Difco Laboratories Inc.), and 2% glucose] with appropriate supplements. For live imaging, cells were grown to a mid-log phase at 24°C. Cells were immobilized on glass slides using concanavalin A and imaged by super-resolution confocal microscopy (SCLIM). SCLIM was developed by combining Olympus model IX-71 inverted fluorescence microscope with a UPlanSApo 100 X NA 1.4 oil objective lens (Olympus, Japan), a high-speed and high-signal-to noise-ratio spinning-disk confocal scanner (Yokogawa Electric, Japan; (*113*), a custom-made spectroscopic unit, image intensifiers (Hamamatsu Photonics, Japan) equipped with a custom-made cooling system, magnification lens system for giving 266.7 X final magnification, three CW lasers (473 nm, 561 nm and 671 nm), and three EM-CCD cameras (Hamamatsu Photonics, Japan) for green, red, and infrared observation. Image acquisition was executed by a custom-made software (Yokogawa Electric, Japan).

For 3D and 4D live imaging, we collected optical sections spaced 100 nm or 200 nm apart in stacks by oscillating the objective lens vertically with a custom-made piezo actuator. Z stack images were converted to 3D voxel data and processed by deconvolution with Volocity (Perkin Elmer, MA) using the theoretical point-spread function for spinning-disk confocal microscopy. For the photobleaching analysis, sfGFP tagged proteins in whole area was photobleached with 473 nm CW laser at 90% of the laser power. Before and after photobleaching, we took 3D images of sfGFP tagged proteins with 473 nm CW laser 10 % of laser power at indicated time. MetaMorph software (Molecular Devices, CA) was used for presenting time-lapse images and analyzing fluorescence signal changes for cisternal conversion and quantifying fluorescence intensities in selected cells before and after photobleaching. For FRAP analysis, we conducted 2D time-lapse observation at every 2 minutes before and after photobleaching and analyzed fluorescence intensities in selected cells after background subtraction by MetaMorph software.

Experimental conditions for LCS-GFP_RUSH traffic assay

i) GOLPH3-KD HeLa cells were transiently transfected with LCS-GFP_RUSH at 37 ℃ in absence of biotin. Cells were then treated with nocodazole (33 µM) and cycloheximide (50 mg/mL) for 3 hours prior to shifting the temperature to 10 ℃ for 60 min in the presence of biotin (40 µM). Then, cells were re-shifted to 37 ℃ for the indicated times (**Table S6**), fixed and subjected to IF. See **Table S6** for a scheme of the synchronization protocol.

ii)GOLPH3-KD HeLa cells were transiently transfected with LCS-GFP_RUSH and culture at 37 ℃ in the absence of biotin for 24 hours. Cells were then infected with VSV-G and cultured at 40°C for 3 hours in presence of nocodazole (33 µM), prior to shifting the temperature to 10 ℃ for 60 min in presence of biotin (40 µM) and cycloheximide (50 mg/mL). Then, cells were re-shifted

to 32 °C for the indicated time, fixed and subjected to IF. See **Table S6** for a scheme of the synchronization protocol.

Lipid Analysis

(Glyco)sphingolipid measurements:

HPLC-Mass Spectrometry:
Glycophingolipids were analyzed by liquid chromatography tandem mass spectrometry (LC-MS/MS) as described earlier (*114*). Briefly, extracts were analyzed with a Quantum Ultra triple quadrupole mass spectrometer connected to an Accela HPLC and Accela autosampler using a solvent gradient. Ceramides identity was achieved through MRM analysis with soft fragmentation. Quantitative analysis is based on calibration curves generated for each lipid. Levels of SLs were normalized to inorganic phosphate (Pi) released from total phospholipids.

HPTLC:
Cells were pulse-labelled with 0,1 µCi/mL (≈ 5nM) ^{3}H-D-erythro-Sphingosine for 2 hours and chased for the indicated times. Subsequently, cells were harvested and processed for lipid extractions. Lipids were spotted on silica-gel high performance-TLC (HPTLC) plates (Merck, Germany), and resolved with a mixture of chloroform: methanol: water (65:25:4 v/v/v). To visualize the unlabelled standards (i.e., Cer, GlcCer, LacCer, Gb3, GM3 and SM) the TLC plates were placed in a sealed tank saturated with iodine vapours, while the radiolabelled lipids were analysed using a RITA® TLC Analyser (Raytest, Germany), and quantified using GINA® (Raytest, Germany) software analysis. The percentage of total C.P.M. associated with each sphingolipid are reported as percentage of total sphingolipids.

MALDI MS:
Lipid extraction
Total lipid extracts were prepared using a standard MTBE protocol followed by a methylamine treatment for sphingo- and glycosphingolipids analysis by mass spectrometry. Briefly, cell pellet was resuspended in 100 µl H2O. 360 µl methanol and 1.2 ml of MTBE were added and samples were placed for 10 min on a vortexer at 4°C followed by incubation for 1 h at room temperature (RT) on a shaker. Phase separation was induced by addition of 200 µl of H2O. After 10 min at RT samples were centrifuged at 1000 g for 10 min. The upper (organic) phase was transferred into a glass tube and the lower phase was re-extracted with 400 µl artificial upper phase [MTBE/methanol/H2O (10:3:1.5, v/v/v)]. The combined organic phases were dried in a vacuum concentrator. Lipids where then resuspended in 500ul of CHCl3 and divided in two aliquots for a further methylamine treatment. 500ul of freshly prepared monomethylamine reagent [methylamine/H2O/n-butanol/methanol (5:3:1:4, (v/v/v/v)] was added to the dried lipid extract and then incubated at 53°C for 1 h in a water bath. Lipids were cooled to RT and then dried. The dried lipid extract was then extracted by n-butanol extraction using 300 µl water-

saturated n-butanol and 150µl H2O. The organic phase was collected, and the aqueous phase was re-extracted twice with 300µl water-saturated n- butanol. The organic phases were pooled and dried in a vacuum concentrator. Lipids were then resuspended in 500ul of CHCl3 and analyzed by MALDI-MS. 30 mg/mL 2,5-DHB was freshly prepared in acetonitrile/water solution (50:50 v/v) with 0.1% TFA. An equivalent volume of sample solution (50ul) was then mixed with matrix before deposition on the MALDI target. All mass spectrometry analysis for the identification of lipids (m/z 600-1800) were obtained using an Applied Biosystems 4800 MALDI-TOF/TOF mass spectrometer equipped with a 200 Hz tripled-frequency Nd:YAG pulsed laser with 355 nm wavelength. Measurements were performed in positive ion reflection mode at an accelerating potential of 20 kV. Each mass spectra were obtained by applying a laser energy of 4600 watts/cm2, averaging 4000 single laser shots/spectrum.

Untargeted Lipidomics:

For phospholipid analysis, lipid extracts (2 µL injection volume in CHCl3:MeOH 2:1) were separated over an 8 minute gradient at a flow rate of 200 µL/min on a HILIC Kinetex Column (2.6lm, 2.1 × 50 mm2) on a Shimadzu Prominence UFPLC xr system (Tokyo, Japan). Mobile phase A was acetonitrile:methanol 10:1 (v/v) containing 10 mM ammonium formate and 0.5% formic acid while mobile phase B was deionized water containing 10 mM ammonium formate and 0.5% formic acid. The elution of the gradient began with 5% B at a 200 ul/min flow and increased linearly to 50% B over 7 min, then the elution continued at 50% B for 1.5 min and finally the column was re-equilibrated for 2.5 min. MS data were acquired in full-scan mode at high resolution on a hybrid Orbitrap Elite (Thermo Fisher Scientific, Bremen, Germany). The system was operated at 240,000 resolution (m/z 400) with an AGC set at 1.0E6 and one microscan set at 10-ms maximum injection time. The heated electrospray source HESI II was operated in positive mode at a temperature of 90°C and a source voltage at 4.0KV. Sheath gas and auxiliary gas were set at 20 and 5 arbitrary units, respectively, while the transfer capillary temperature was set to 275°C.

Isothermal titration calorimetry (ITC)

ITC experiments were performed in a buffer containing 300 mM NaCl, 10 mM Bicine pH 8.5 and 1 mM DTT. LCS Peptides were synthesized and delivered as lyophilized powder with a biotin moiety located at the N terminus (Charite Universitaetsmedizin Berlin, Germany). The peptides were dissolved in buffer, centrifuged at 14000 x g for 10 minutes and only the supernatant was used. The dissolved peptide concentrations were calculated based upon their absorbance at 280 nm and their corresponding molar extinction coefficient. Experiments consisted of titrations of 20 injections of 2 µL of titrant (peptides) into the cell containing GOLPH3 protein at a 25-fold lower concentration. Typical concentrations for the titrant were around 2.5 mM for experiments depending on the affinity. Experiments were performed at 25°C and a stirring speed of 1000 rpm on an MicroCal PEAQ-ITC (Malvern Panalytic). All data

were processed using MicroCal PEAQ-ITC Analysis Software and fit to a one-site binding model after background buffer subtraction.

Quantification and Statistical Analysis

Error bars correspond to either standard deviation (S.D.) or standard error of the mean (S.E.M.) according to the different experiments and as indicated in the figure legends. Statistical evaluations report on Student's t test $^{*}p < 0.05$, $^{**}p < 0.01$, and $^{***}p < 0.001$ (ns, not significant).

Supplemetary Figures

Figure S1. GOLPH3 binds a compound motif in the cytosolic tail of specific GSL synthetic enzymes

(A) Cytosolic tails of glyco-enzymes bearing the LxxR motif. Red boxes indicate known GOLPH3 interactors. Colored squares indicate the pathway each enzyme is involved in: Red, GSL metabolism; Cyan, glycosaminoglycan assembly; Purple, N-glycosylation; Green O-glycosylation. (B) Flow cytometry-based lectin screening of GOLPH3-OE HeLa cells. AAL, *Aleuria aurantia* Lectin; SNA, *Sambucus nigra* Lectin; PNA, Peanut Agglutinin; RCA-I *Ricinus communis* Agglutinin I; PHA-L *Phaseolus vulgaris* Leucoagglutinin; ShTxB, Shiga toxin 1a B fragment. (C) GOLPH3-OE HeLa cells were preincubated in the presence of xyloside and pulse-labelled for 5 minutes with [^{35}S]-sulfate (see **Methods** for details). The produced glycosamminoglycans (GAGs) were measured by liquid scintillation counter and expressed as counts per minute (CPM) normalized to mg of protein for the indicated conditions (n = 4, data are means ± SEM, ns = not significant). (D) Hela cells expressing HA-LCS were lysed and HA-LCS was immunoprecipitated by anti-HA antibody. Co-immunprecipitated GOLPH3 was detected in the immunoprecipitated fraction. F.T, flow through fraction; I.P. immunoprecipitated fraction. (E) List of 22 glyco-enzymes bearing the LxxR motif (red) and at least a positively charged residue (cyan) in the 2-5 aa upstream the LxxR in their cytosolic tail. Red boxes indicate known GOLPH3 interactors, Green boxes indicate new GOLPH3 clients found in this study. The colored squares indicate the metabolic pathways each enzyme is involved in. Red, GSL metabolism; Cyan, glycosaminoglycan assembly; Purple, N-glycosylation; Green O-glycosylation. (F) Schematic representation of GSLs synthesis and of the enzymes (in red) That bear the [+]-$x_{(2-5)}$-LxxR motif. Note that LacCer is the common precursor for the synthesis of globo, ganglio, lacto and asialo GSL series.

Figure S2. GOLPH3 controls LCS sub-Golgi distribution

(A) GOLPH3-KD HeLa cells were processed for cryoimmunolabeling. Anti-GalT1 antibody (10-nm gold particles) and anti-GM130 antibody (15-nm gold particles, arrowheads) as a marker of the cis side of the Golgi stack. Quantification of the distribution (LD normalised to the *trans cisternae*) of GalT1 across the stack and peri-Golgi vesicles is shown in the graphs (right). (mean ± SEM). Bar 150 nm. (B) GOLPH3-OE (top pictures) or KD (bottom pictures) LCS-HA expressing HeLa cells were fixed and processed for cryoimmunolabeling with an anti-HA antibody (15-nm gold particles) and anti-GOLPH3 antibody (10-nm gold particles, arrowheads) or anti-GM130 antibody (10-nm gold particles, arrowheads) as indicated. Bar 250 nm. Quantification of the distribution (LD normalised to the *trans cisternae*) of LCS across the stack and in peri-Golgi vesicles is shown in the graphs (right). (n indicated in the graph; mean ± SEM. Bar 150 nm. (B, bottom pictures). (C) LCS-HA expressing HeLa cells were fixed and processed for cryoimmunolabeling with an anti-GM130 antibody (15-nm gold particles) and anti-GOLPH3 antibody (10-nm gold particles, black arrowheads), or an anti-HA antibody (15-nm gold particles) and anti-GOLPH3 antibody (5-nm gold particles, black arrowheads). Quantification of

the distribution (LD) of GOLPH3 across the stack and in peri-Golgi vesicles is shown in the graphs (right) (data are means ± SEM). Bar 150 nm.

Figure S3. Vps74p controls the sub-Golgi distribution and Golgi retention of Mnn9p

(A) Wild-type (left) and *vps74Δ* (middle) yeast cells expressing Mnn9-mCherry (red, Vps74p client) and Sys1-GFP (green, *trans*-Golgi marker) were observed. Representative 3D images are shown on the left. Magnified images of selected *cisternae* (boxed areas in the left panels) are shown on the right (inset). Arrowheads indicate *cisternae* with Mnn9-mCherry and Sys1-GFP. The fraction of positive *cisternae* (Sys1-GFP, Mnn9-mCherry, or both of them) in wild-type and *vps74Δ* yeast cells was quantified and is shown in the right box plots. (n indicated in the graph; data are means ± SEM; *p <0.05, ***p <0.001). (B) Wild-type and *vps74Δ* yeast cells expressing Mnn9-mCherry (red, Vps74p client) and Sys1-GFP (green, *trans*-Golgi marker) were treated with 500 µg/ml cycloheximide for 60 min and then observed. 2D projection images of Mnn9-mCherry and Sys1-GFP in WT (left two panels) and *vps74Δ* (right two panels) yeast cells are shown. (C) Fluorescence recovery after photobleaching (FRAP) of Mnn9-sfGFP fluorescence intensities in 15 wild-type (blue) and 15 *vps74Δ* (red) yeast cells were plotted at every 2 min during observation time in the left graph. Average fluorescence intensities (thick lines) ± SEM (thin lines) are shown). Fluorescence intensities of Mnn9-sfGFP and Vph1-sfGFP in selected yeast cells were quantified at indicated time after photobleaching. Box plots of Mnn9-sfGFP (left) and Vph1-sfGFP (right) fluorescence intensities in wild-type (blue) and *vps74Δ* (red) yeast cells are shown in the middle. (n indicated in the graph). Right panels show representative 3D images of Vph1-sfGFP in wt (top) and *vps74Δ* (bottom) yeast cells before (pre-bleach) and after (0min and 5 min) photobleaching. Fluorescence signals of Vph1-sfGFP after photobleaching are emphasized.

Figure S4. GOLPH3 controls the localization and levels of selected GSL synthetic enzymes

(A) mRNA levels of *B4GALT5* were evaluated in GOLPH3-OE or KD HeLa cells or PHFs by qRT-PCR. (n = 3; data are means ± SD). (B) LCS-GFP_RUSH expressing GOLPH3-OE or KD HeLa cells were fixed, at the indicated time points after traffic synchronization and processed for IF labeling: LCS (green), LAMP1 (red). (n = 3). Bar, 20 µm. (C) GalT1-GFP_RUSH expressing GOLPH3-OE or KD HeLa cells were lysed at the indicated time points at the indicated time points after traffic synchronization. Protein lysates were processed for SDS-PAGE and immunoblotted with the indicated antibodies (data are representative of three independent experiments). (D) GOLPH3-OE or KD HeLa cells expressing the indicated glyco-enzymes were lysed and processed for WB. (data are representative of three independent experiments). (E) GOLPH3-KD HeLa cells expressing the indicated glyco-enzymes were treated with bafilomycin A1 (BafA1, 10 nM) for 16 hr, fixed, and processed for IF labeling: HA (green), LAMP1 (red), and TGN (blue). (data are representative of at least three independent experiments). Bar, 20 µm. (F) GOLPH3-KD HeLa cells expressing the indicated glyco-enzymes were fixed and processed for IF labeling. HA (green), GOLPH3 (red) and TGN46 (blue). Bar 20 µm.

Figure S5. Effects of GOLPH3 and LCS manipulations on lipid metabolism

(A) Effects of GOLPH3 KD or OE on sphingolipid levels as assessed by LC/MS of PHF cells (n = 3; data are means ± SD; *p <0.05, **p <0.01, ***p <0.001). The dotted red box highlights the effects on C16:0 Cer. (B) Phospho-lipidomics of GOLPH3 OE and KD HeLa cells. Data are shown in a mirror-image volcano plot. Individual lipids are color-coded according to the class they belong to. The dotted lines indicate the significance thresholds (i.e., p<0.05 and log2 fold change <-1 or >1). (C) Effects of GOLPH3 KD or OE on GSL metabolism as assessed by [^{3}H]-sphingosine pulse (2 hours) and chase (indicated times), lipid extraction and HPTLC separation and radioactive counting of PHFs. (n = 3; data are means ± SD). (D) Simplified scheme of GSL metabolism representing the positions of the GOLPH3 clients (in red) in the pathway and the effects of GOLPH3 on the metabolic activities of the enzymes (arrows, with the increased activities if GOLPH3 clients in red). In HeLa cells, the conversion rates of GlcCer to LacCer by LCS and of LacCer to Gb3 by Gb3S are markedly enhanced. Thus, the levels of LacCer will increase or decrease depending on the balance between the increased activities of LCS and Gb3S. Instead, the levels of Gb3 and of downstream globo metabolites are expected to increase, and the levels of the Cer/GlcCer pool to decrease. In Hela cells the globo series is predominant, and the ganglio series is present but minor, while metabolites of the other series are undetectable. Thus, the metabolic effects of GOLPH3 is dominated by the changes in globo-series metabolism, and the effects of clients acting in the other series is not appreciable. In other cell types, the scenario may vary. Thus, while LCS is likely to have a pivotal function in all cells, the effects of GOLPH3 OE on the complex series will depend on the expression levels of the relevant enzymes. In general, the effects of GOLPH3 depend on the outcome of the 'competition' between the activities of its clients and of other enzymes, e.g., between LCS and GCS in the common axis of the pathway, which results in the increase of LacCer at the expense of GlcCer /Cer, or amongst the first enzymes in the complex GSL series synthetic pathways, which results in an increase of globosides in Hela cells, and, possibly, of gangliosides in other cells. The significance of the GOLPH3 clients within the complex series will again depend on alterations of the balance between active metabolites, but the functional outcome of these effects is difficult to decipher at the stage. (E) Effects of LCS KD or OE on sphingolipid levels as assessed by LC/MS of HeLa cells. The magnified box highlights the effects on C16:0 Cer. (n = 3; data are means ± SD; *p <0.05, **p <0.01, ***p <0.001). (F) LCS OE HeLa cells processed for ShtxB staining followed by flow cytometry analysis. Representative flow cytometry distributions and the relative scatter plots are shown for each condition. Data are representative of three independent experiments.

Figure S6. GOLPH3 impacts growth signaling through changing GSL metabolism

(A) Cell lysates from PHFs KD or OE either GOLPH3 or LCS were processed for SDS-PAGE and Western blotting with antibodies aimed at evaluating the activation status of the mTOR pathway and p21. (B) Assessment of GSL synthesis in parental HeLa, GCS-KO, LCS-KO and LCS-KO cells overexpressing LCS, [^{3}H]-sphingosine pulse (2 hours) and chase (24 hours), lipid

extraction, HPTLC separation, and radioactive counting. (n = 3, data are means ± SD). (C) Quantification of soft agar colony formation assay of HeLa LCS-KO cells overexpressing RasVal12. (n indicated in the graph; data are means ± SEM; ***p <0.001). (D) Lysates from GOLPH3-OE HeLa Gb3S-KD were processed for SDS-PAGE and Western blotting and the levels of p-Akt (Ser473 and Thr308) were evaluated. (E) Soft agar colony formation assay of the experiment in (D). (n indicated in the graph; data are means ± SEM; ***p <0.001, n.s. = not significant). (F) GOLPH3 or LCS OE HeLa cells expressing PH-Akt-GFP serum starved overnight, were treated with wortmannin (400 nM for 30 minutes) before been fixed and processed for IF. GFP (green), GOLPH3 (red) and DAPI (blue). Scale bar, 20 µm. (G) Quantification of membrane association of the PH-Akt-GFP of the experiments performed in (F) (n indicated in the graph; n.s. not significant; data are means ± SEM; ***p <0.001). (H) GOLPH3 or LCS OE HeLa cells expressing ORP5-PH-GFP or PLCd-PH-GFP, serum starved overnight were fixed and processed for IF. Quantification of membrane association of ORP5-PH-GFP and PLCd-PH-GFP is reported in the graph. (n indicated in the graph; n.s. not significant). (I) GOLPH3 or LCS OE HeLa cells expressing PH-Akt-GFP serum starved overnight, were stimulated with 200 ng/ml insulin for indicated time. Images were acquired at 60 seconds intervals. GFP (green), PHA-L (Biotinylated Phaseolus Vulgaris Leucoagglutinin, white). Scale bar, 20 µm (white arrowheads show the membrane association of PH-Akt-GFP). (J) Quantification of membrane association dynamics of the PH-Akt-GFP is reported on the right. (K) GOLPH3 or LCS OE were kept in low serum (1% FCS) for 16 hours and then treated with increasing concentrations of GDC-0941 for one hour, lysed and processed for WB. The mTOR substrates were evaluated. (L) Schematic representation of the PM's GSLs and their modulatory effects on RTKs impinging on PI3K-Akt-mTor signalling pathway. The main players of the mTor signaling cascade and the relative downstream cellular effects are reported.

Figure S7 GOLPH3 amplification correlates with high LCS protein levels and sustained GSL production

(A) Cell lysates from prostate cancer cell line, LNCaP and DU145 respectively, were processed for SDS-PAGE and Western blotting with antibodies aimed at evaluating the levels of expression of GOLPH3, LCS and the activation status of the mTOR substrates. (B) Assessment of GSL synthesis in LNCaP and DU145 cell line, by [^{3}H]-sphingosine pulse (2 hours) and chase (24 hours), lipid extraction and HPTLC separation and radioactive counting. (n = 2, data are means ± SEM). (C) RT-qPCR based assessment of GOLPH3 and LCS KD efficiencies in LNCaP and DU145. (D) The cBioportal database (http://www.cbioportal.org) for cancer genomics was interrogated for GOLPH3 gene in 32 cancer sample collections corresponding to 26731 fully sequenced cancer samples. The graph represents the alteration frequency of GOLPH3 in each sample collection.

Movie S1: LCS-GFP_RUSH synchronized transport in GOLPH3-OE or-KD HeLa cells

GOLPH3-OE or-KD HeLa cells were transfected to express LCS-GFP_RUSH. After 24 hours of expression, at time 0, DMEM containing cycloheximide (10 mg/mL) and biotin (40 nM) was added to cells. The trafficking of LCS-GFP_RUSH was monitored using confocal microscope. Images were acquired at 5 minutes intervals.

Movie S2: Dynamics of PH-Akt-GFP recruitment to the plasma membrane in response to insulin in GOLPH3-OE or LCS-OE HeLa cells.

GOLPH3-OE or LCS-OE HeLa cells were transfected to express PH-Akt-GFP and serum starved overnight. Images were acquired at 1 min intervals. At minute 5, cells were stimulated with 200 ng/ml.

Figure S1

A

LxxR

A4GALT	MSKPPDLLLRLLRGAPRQRVCT
ABO	MAEVLRTLAGKPKCHALRPMILFLIMLVLVLF
B3GALNT1	MASALWTVLPSRMSLRSLKW
B3GALT2	MLQWRRRHCCFAKMTWNAKRSLFR
B3GALT4	MQLRLFRR
B3GALT6	MKLLRRAWRRR
B3GAT3	MKLKLKN
B3GNT3	MKYLRHRRPN
B3GNT4	MLPPQPSAAHQGRGGRSGLLPKGPAMLC
B3GNT6	MAFPCRRSLTAK
B3GNT7	MSLWKK
B3GNT9	MRRRLRLRRD
B4GALNT1	MWLGRRA
B4GALNT2	MGSA... LCLELRGADPAWGPFAAHGRSRRQGSR
B4GALNT3	MGSPRAARPPLLLRPVKLLRRRFR
B4GALNT4	MPRLPVKKIRKQMKL
B4GALT3	MLRRLLERPC
B4GALT4	MGFNLTFHLSYK
B4GALT5	MRARRGLLRLPRRS
B4GALT7	MFPSRRKAAQLPWEDGRSGLLSGGLPRKCS
CHST15	MRHC... AVLEVRTEGNENWGGFLRFKKGKRC
CHST2	NKILF... AVLEVRTE... GFLRFKKG... SPLGMKVFRRK
CHST4	MLLPKKM
CSGALNACT2	MPRRGLILHTR
EXT2	MCASVKYNIRGPALIPRMKTKHRIY
FUT4	MRRL... LALAARPAR...
FUT5	MDPLGPAKPQWLWRR
GALNT15	MLLRKRYRHRP
GALNT3	MAHLKRLVKLHIKRHYHKK
GALNT6	MRLLRRRH
GCNT1	MLRTLLRRR
HS3ST5	MLFKQQAWLRQK
MAN1A1	MPVGGLLPLFSSPAGGVLGGGLGGGGGRKGSGPAALRLTEK
MAN1A2	MTTPALLPLSGRRIPPLNLGPPSFPHHRATLRLSEK
MAN1C1	MLMRKVPGFVPASPWGLRLPQK
MGAT4C	MFKFHQMKHIFEILDKMRCLRKR
NDST4	MNLIVKLRRSFRT
POMGNT1	MDDWKPSPLIKPFGARKKRSWYLTWKYKLTNQRALRR
ST3GAL1	MVTLRKRTLKVLT
ST3GAL5	MRRPSLLLKDILKV
ST6GAL1	MIHTNLKKK
ST6GALNAC3	MACILKRK
ST6GALNAC6	MAC...AGRRHLPLSRRRREMSSNKEQRS
ST8SIA1	MSPCGRARRQTSRGAMAVLAWKFPRTRLP
ST8SIA5	MRYADPSANRDLLGSRT
XYLT1	MVAAPCARRLARRSHSA
XYLT2	MVASARVQKLVRRYK

B

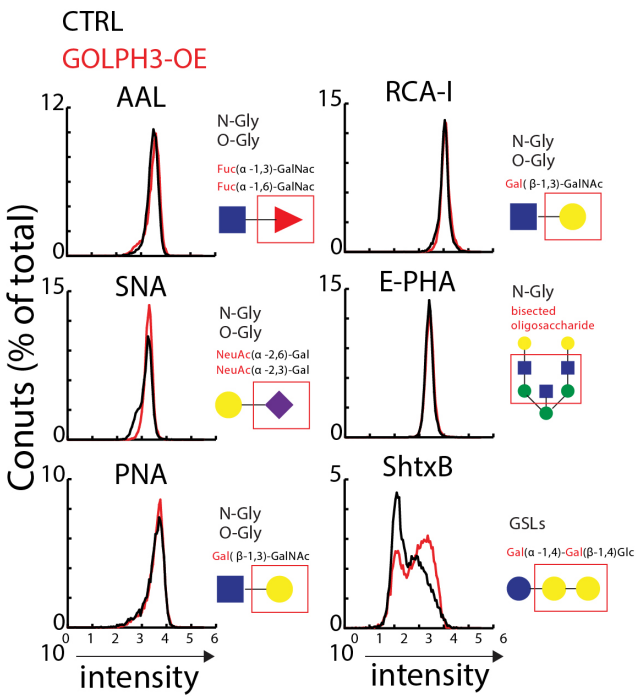

C

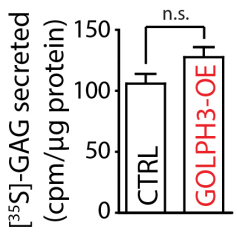

D

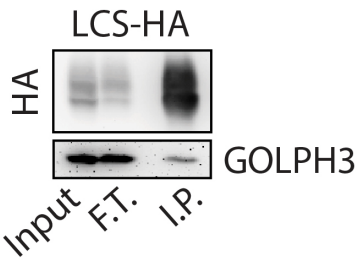

E

[+]-x$_{(2-5)}$-LxxR

A4GALT	MSKPPDLLLRLLRGAPRQRVCT
B3GNT4	MLPPQPSAAHQGRGGRSGLLPKGPAMLC
B3GNT9	MRRRLRLRRD
B4GALNT3	MGSPRAARPPLLLRPVKLLRRRFR
B4GALT5	MRARRGLLRLPRRS
CHST2	...RRWPASPLGMKVFRRK
CSGALNACT2	MPRRGLILHTR
EXT2	MCASVKYNIRGPALIPRMKTKHRIYX
FUT4	...RAVPGWASWPAHLALAARPARH...
FUT5	MDPLGPAKPQWLWRR
GALNT3	MAHLKRLVKLHIKRHYHKK
GCNT1	MLRTLLRRR
HS3ST5	MLFKQQAWLRQK
MAN1A2	MTTPALLPLSGRRIPPLNLGPPSFPHHRATLRLSEK
MGAT4C	MFKFHQMKHIFEILDKMRCLRKR
POMGNT1	MDDWKPSPLIKPFGARKKRSWYLTWKYKLTNQRALRR
ST3GAL5	MRRPSLLLKDILKV
ST6GAL1	MIHTNLKKK
ST6GALNAC6	MAC...AGRRHLPLSRRRREMSSNKEQRS
ST8SIA1	MSPCGRARRQTSRGAMAVLAWKFPRTRLP
ST8SIA5	MRYADPSANRDLLGSRT
XYLT2	MVASARVQKLVRRYK

F

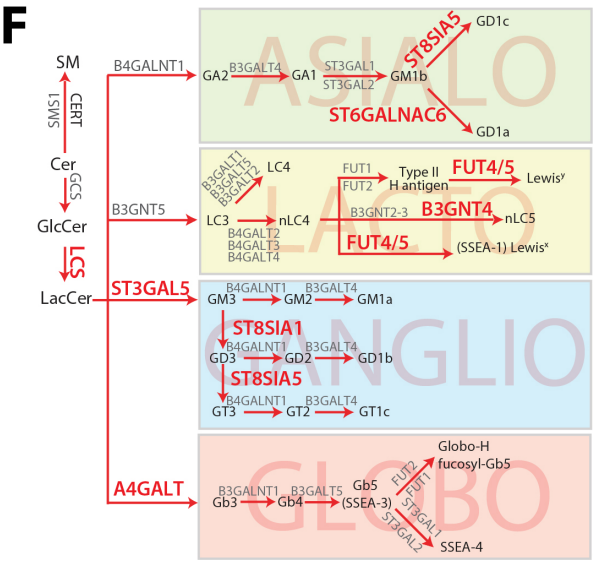

Figure S2

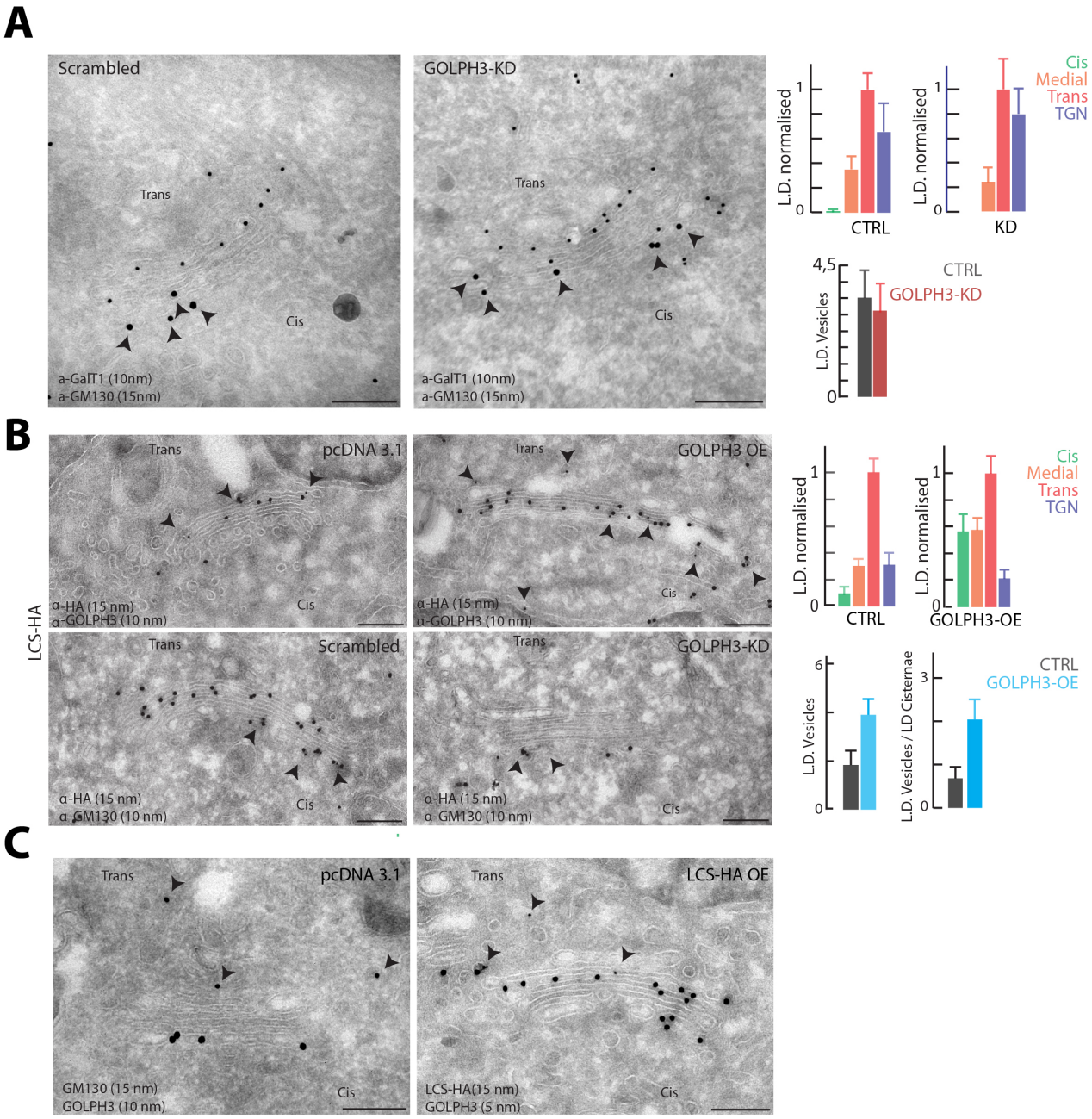
A
Scrambled
Trans
Cis
a-GalT1 (10nm)
a-GM130 (15nm)
GOLPH3-KD
Trans
Cis
a-GalT1 (10nm)
a-GM130 (15nm)
L.D. normalised
1
0
CTRL
KD
Cis
Medial
Trans
TGN
4,5
L.D. Vesicles
0
CTRL
GOLPH3-KD
B
LCS-HA
Trans
pcDNA 3.1
Cis
α-HA (15 nm)
α-GOLPH3 (10 nm)
Trans
GOLPH3 OE
Cis
α-HA (15 nm)
α-GOLPH3 (10 nm)
Trans
Scrambled
Cis
α-HA (15 nm)
α-GM130 (10 nm)
Trans
GOLPH3-KD
Cis
α-HA (15 nm)
α-GM130 (10 nm)
L.D. normalised
1
0
CTRL
GOLPH3-OE
Cis
Medial
Trans
TGN
6
L.D. Vesicles
0
3
L.D. Vesicles / LD Cisternae
0
CTRL
GOLPH3-OE
C
Trans
pcDNA 3.1
Cis
GM130 (15 nm)
GOLPH3 (10 nm)
Trans
LCS-HA OE
Cis
LCS-HA(15 nm)
GOLPH3 (5 nm)

Figure S3

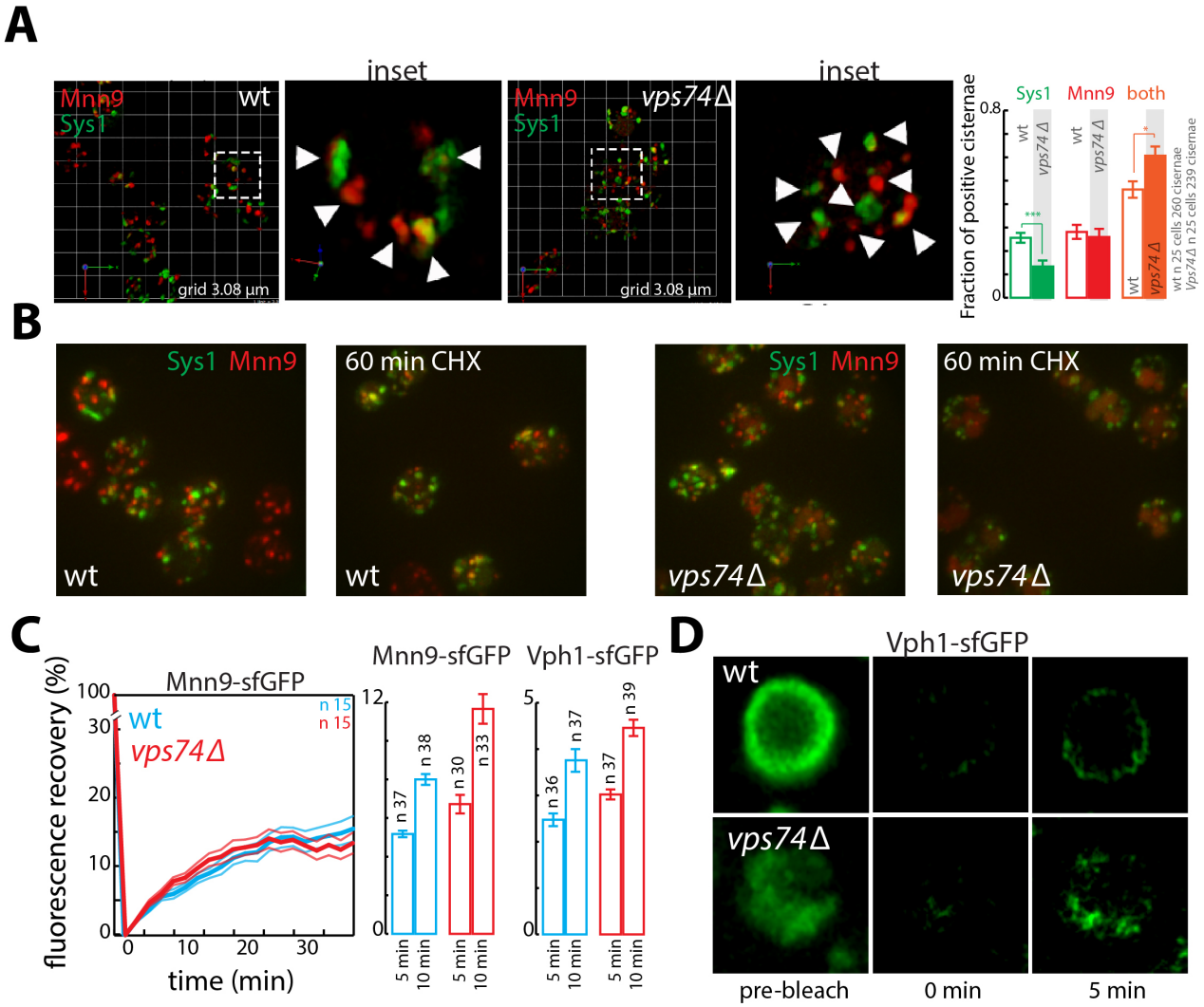
A
inset
inset
Mnn9
Sys1
wt
grid 3.08 µm
Mnn9
Sys1
vps74Δ
grid 3.08 µm
Sys1
Mnn9
both
Fraction of positive cisternae
0.8
0
wt
vps74 Δ
***
*
wt n 25 cells 260 cisernae
Vps74 Δ n 25 cells 239 cisernae
B
Sys1 Mnn9
wt
60 min CHX
wt
Sys1 Mnn9
vps74Δ
60 min CHX
vps74Δ
C
Mnn9-sfGFP
fluorescence recovery (%)
100
30
20
10
0
wt
vps74Δ
n 15
n 15
0
10
20
30
time (min)
Mnn9-sfGFP
Vph1-sfGFP
12
0
n 37
n 38
n 30
n 33
5
0
n 36
n 37
n 37
n 39
5 min
10 min
D
Vph1-sfGFP
wt
vps74Δ
pre-bleach
0 min
5 min

Figure S4

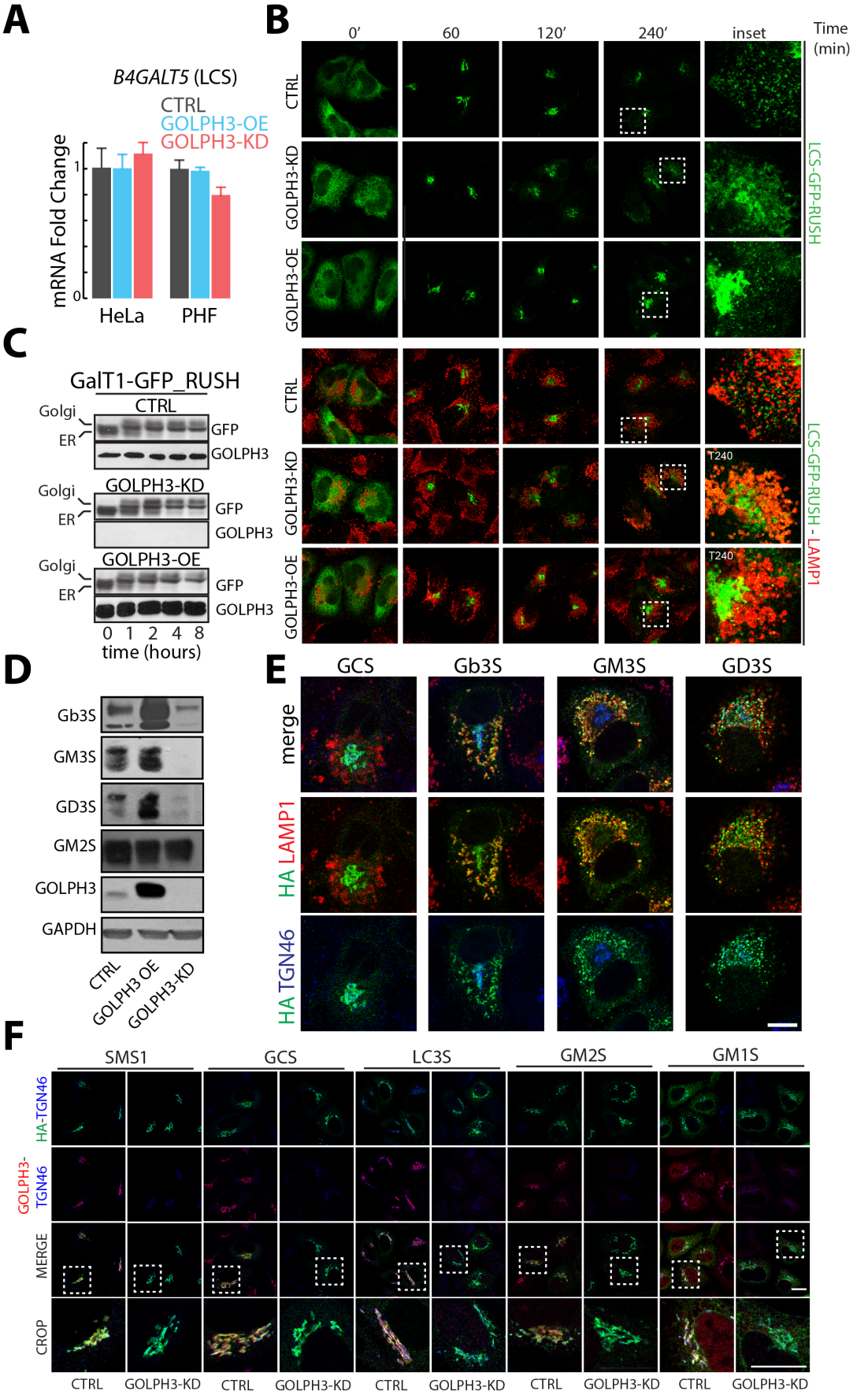
A
B4GALT5 (LCS)
CTRL
GOLPH3-OE
GOLPH3-KD
mRNA Fold Change
1
0
HeLa
PHF
B
0′
60
120′
240′
inset
Time (min)
CTRL
GOLPH3-KD
GOLPH3-OE
LCS-GFP-RUSH
T240
LCS-GFP-RUSH - LAMP1
C
GalT1-GFP_RUSH
Golgi
ER
CTRL
GFP
GOLPH3
GOLPH3-KD
GOLPH3-OE
0 1 2 4 8
time (hours)
D
Gb3S
GM3S
GD3S
GM2S
GOLPH3
GAPDH
CTRL
GOLPH3 OE
GOLPH3-KD
E
GCS
Gb3S
GM3S
GD3S
merge
HA LAMP1
HA TGN46
F
SMS1
GCS
LC3S
GM2S
GM1S
HA-TGN46
GOLPH3-TGN46
MERGE
CROP
CTRL
GOLPH3-KD

Figure S5

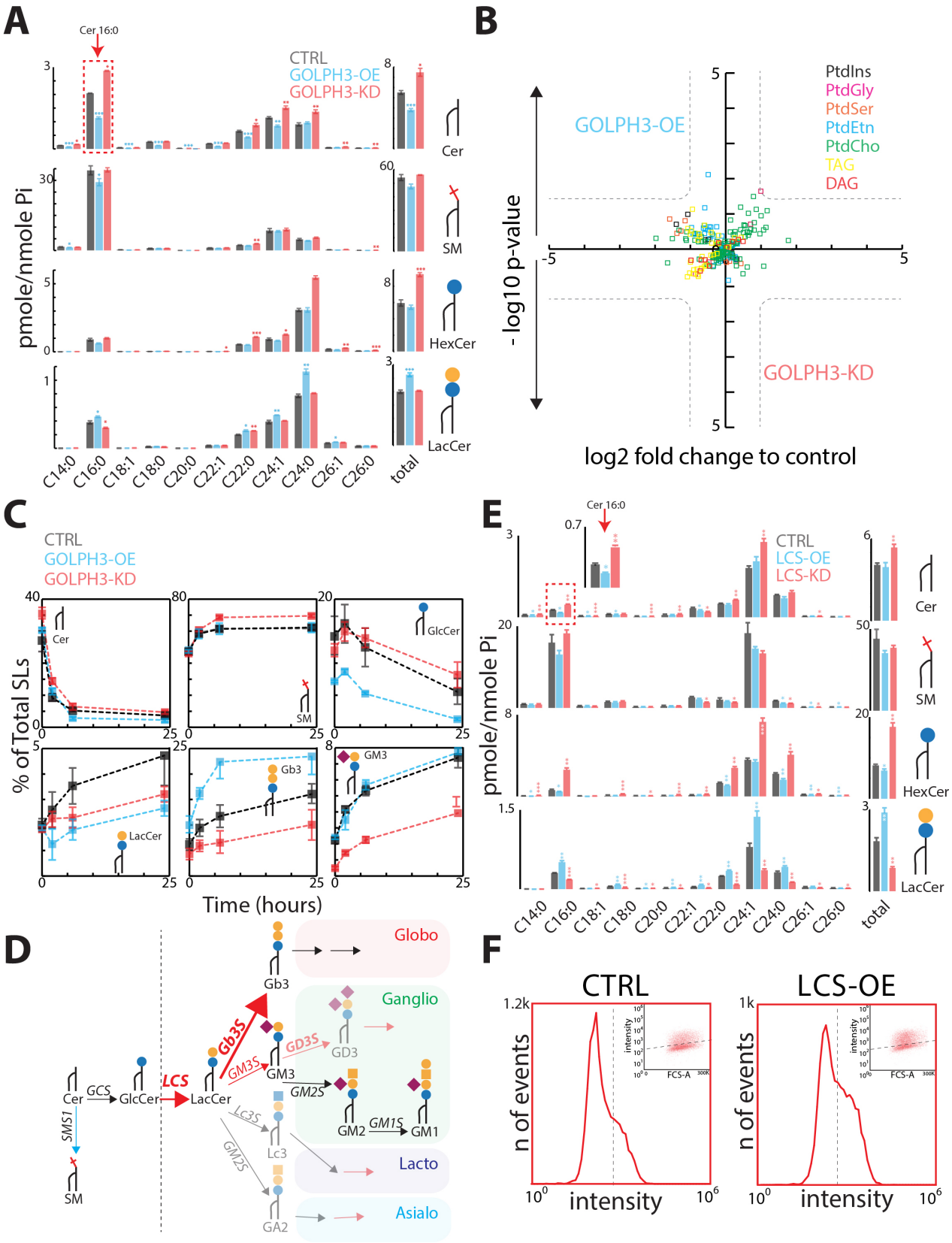
A
Cer 16:0
CTRL
GOLPH3-OE
GOLPH3-KD
pmole/nmole Pi
Cer
SM
HexCer
LacCer
C14:0
C16:0
C18:1
C18:0
C20:0
C22:1
C22:0
C24:1
C24:0
C26:1
C26:0
total
B
PtdIns
PtdGly
PtdSer
PtdEtn
PtdCho
TAG
DAG
GOLPH3-OE
GOLPH3-KD
- log10 p-value
log2 fold change to control
C
CTRL
GOLPH3-OE
GOLPH3-KD
% of Total SLs
Cer
SM
GlcCer
LacCer
Gb3
GM3
Time (hours)
E
Cer 16:0
CTRL
LCS-OE
LCS-KD
pmole/nmole Pi
Cer
SM
HexCer
LacCer
C14:0
C16:0
C18:1
C18:0
C20:0
C22:1
C22:0
C24:1
C24:0
C26:1
C26:0
total
D
Globo
Ganglio
Lacto
Asialo
Gb3
GD3
GM3
GM2
GM1
Lc3
GA2
Cer
GlcCer
LacCer
SM
GCS
SMS1
LCS
Gb3S
GM3S
GD3S
GM2S
GM1S
Lc3S
GM2S
F
CTRL
LCS-OE
n of events
intensity
FCS-A

Figure S6

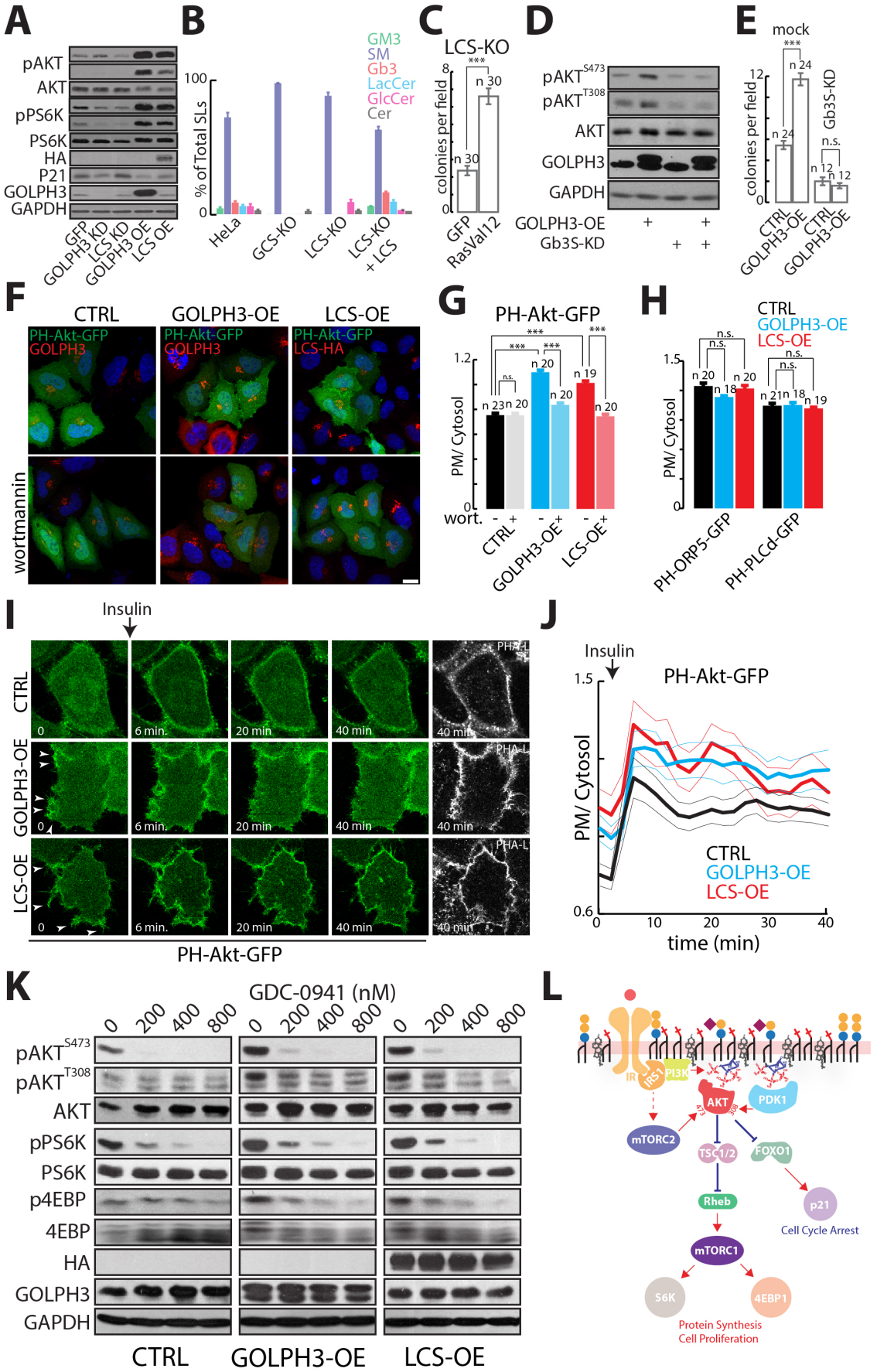
A
pAKT
AKT
pPS6K
PS6K
HA
P21
GOLPH3
GAPDH
GFP
GOLPH3 KD
LCS KD
GOLPH3 OE
LCS OE
B
GM3
SM
Gb3
LacCer
GlcCer
Cer
% of Total SLs
100
0
HeLa
GCS-KO
LCS-KO
LCS-KO + LCS
C
LCS-KO
colonies per field
8
0
***
n 30
n 30
GFP
RasVal12
D
pAKT S473
pAKT T308
AKT
GOLPH3
GAPDH
GOLPH3-OE
Gb3S-KD
E
mock
Gb3S-KD
colonies per field
12
0
***
n 24
n 24
n.s.
n 12
n 12
CTRL
GOLPH3-OE
CTRL
GOLPH3-OE
F
CTRL
GOLPH3-OE
LCS-OE
PH-Akt-GFP
GOLPH3
PH-Akt-GFP
GOLPH3
PH-Akt-GFP
LCS-HA
wortmannin
G
PH-Akt-GFP
PM/ Cytosol
1.2
0
***
***
***
***
n.s.
n 23
n 20
n 20
n 20
n 19
n 20
wort.
CTRL
GOLPH3-OE
LCS-OE
H
CTRL
GOLPH3-OE
LCS-OE
PM/ Cytosol
1.5
0
n.s.
n.s.
n.s.
n.s.
n 20
n 18
n 20
n 21
n 18
n 19
PH-ORP5-GFP
PH-PLCd-GFP
I
Insulin
CTRL
GOLPH3-OE
LCS-OE
0
6 min.
20 min
40 min
PHA-L
PH-Akt-GFP
J
Insulin
PH-Akt-GFP
PM/ Cytosol
1.5
0.6
CTRL
GOLPH3-OE
LCS-OE
0
10
20
30
40
time (min)
K
GDC-0941 (nM)
0
200
400
800
pAKT S473
pAKT T308
AKT
pPS6K
PS6K
p4EBP
4EBP
HA
GOLPH3
GAPDH
CTRL
GOLPH3-OE
LCS-OE
L
IR
IRS1
PI3K
AKT
PDK1
mTORC2
TSC1/2
FOXO1
Rheb
p21
Cell Cycle Arrest
mTORC1
S6K
4EBP1
Protein Synthesis
Cell Proliferation

Figure S7

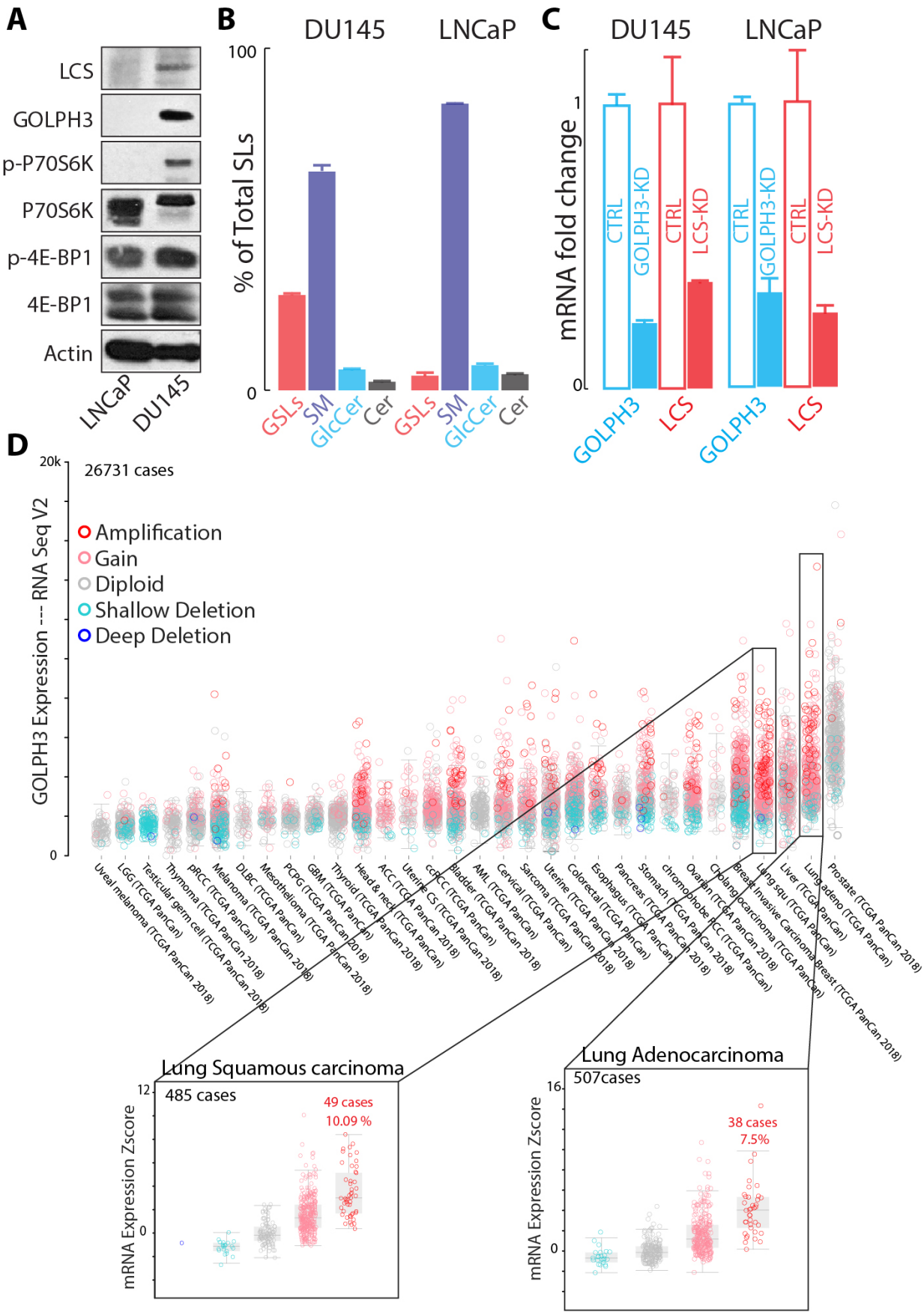
A
LCS
GOLPH3
p-P70S6K
P70S6K
p-4E-BP1
4E-BP1
Actin
LNCaP
DU145
B
DU145
LNCaP
% of Total SLs
100
0
GSLS
SM
GlcCer
Cer
C
DU145
LNCaP
mRNA fold change
1
0
CTRL
GOLPH3-KD
LCS-KD
GOLPH3
LCS
D
26731 cases
GOLPH3 Expression --- RNA Seq V2
20k
0
Amplification
Gain
Diploid
Shallow Deletion
Deep Deletion
Uveal melanoma (TCGA PanCan 2018)
LGG (TCGA PanCan)
Testicular germ cell (TCGA PanCan 2018)
Thymoma (TCGA PanCan 2018)
pRCC (TCGA PanCan)
Melanoma (TCGA PanCan)
DLBC (TCGA PanCan 2018)
Mesothelioma (TCGA PanCan 2018)
PCPG (TCGA PanCan 2018)
GBM (TCGA PanCan 2018)
Thyroid (TCGA PanCan)
Head & neck (TCGA PanCan 2018)
ACC (TCGA PanCan 2018)
Uterine CS (TCGA PanCan 2018)
ccRCC (TCGA PanCan 2018)
Bladder (TCGA PanCan 2018)
AML (TCGA PanCan)
Cervical (TCGA PanCan 2018)
Sarcoma (TCGA PanCan)
Uterine (TCGA PanCan 2018)
Colorectal (TCGA PanCan 2018)
Esophagus (TCGA PanCan)
Pancreas (TCGA PanCan)
Stomach (TCGA PanCan 2018)
chromophobe RCC (TCGA PanCan)
Ovarian (TCGA PanCan 2018)
Cholangiocarcinoma (TCGA PanCan 2018)
Breast Invasive Carcinoma (TCGA PanCan)
Lung squ (TCGA PanCan)
Liver (TCGA PanCan)
Lung adeno (TCGA PanCan)
Prostate (TCGA PanCan 2018)
Lung Squamous carcinoma
485 cases
49 cases
10.09 %
mRNA Expression Zscore
12
0
Lung Adenocarcinoma
507cases
38 cases
7.5%
mRNA Expression Zscore
16
0

Supplementary Tables.

Table S1 TMA FISH and IHC analysis. N/A, data not available; CGN, copy number gain (i.e., cases where the average of GOLPH3/cell FISH signals were >4.0 and <6.0); AMPL, amplified i.e., cases where GOLPH3/Centromere 5 ratio was ≥ 2.0 or when the average GOLPH3 FISH signals per cell were ≥6.0).

sex	age	FISHGOLPH3	GOLPH3:IHC	LCS:IHC
M	70	NO	high	weak
F	62	CNG	high	med
M	75	CNG	med	med
F	76	N/A	med	med
M	67	CNG	weak	weak
M	72	CNG	med	neg
M	44	NO	neg	neg
F	65	NO	weak	weak
M	65	NO	med	med
M	64	NO	med	neg
F	51	AMPL	neg	neg
M	48	NO	med	med
M	63	CNG	high	weak
M	57	N/A	neg	neg
F	57	NO	med	weak
M	78	AMPL	neg	neg
M	75	NO	med	med
M	54	NO	med	med
M	47	NO	med	neg
M	56	CNG	high	weak
F	54	NO	high	weak
M	58	NO	med	med
F	66	N/A	neg	neg
M	63	NO	high	weak
F	66	AMPL	med	med
F	68	NO	med	weak
M	71	NO	neg	neg
M	59	NO	med	med
M	56	CNG	med	med
M	63	NO	med	med
M	52	CNG	med	med
M	63	AMPL	weak	weak
M	78	NO	med	med
M	69	CNG	med	med
M	78	NO	high	med

M	71	AMPL	med	med
M	65	NO	med	med
M	59	NO	weak	weak
M	56	NO	neg	neg
M	59	NO	med	med
M	55	NO	med	med
M	67	NO	high	med
M	70	NO	weak	med
M	72	AMPL	weak	weak
M	55	NO	med	med
M	60	NO	med	neg
F	47	AMPL	med	neg
F	62	NO	weak	weak
F	55	NO	weak	weak
M	64	NO	weak	weak
M	68	NO	weak	med
M	54	CNG	med	med
M	77	NO	med	weak
F	71	CNG	high	high
M	63	NO	weak	weak
F	54	NO	weak	med
F	53	CNG	high	med
F	59	CNG	med	med
M	57	CNG	high	med
F	69	NO	med	med
F	72	CNG	med	weak
F	70	NO	med	weak
F	66	NO	high	neg
M	75	NO	high	med
M	53	NO	med	neg
M	67	CNG	neg	med
F	52	CNG	neg	med
M	73	NO	weak	neg
M	65	AMPL	med	med
M	71	NO	weak	weak
M	68	CNG	neg	neg
F	28	NO	high	high

Table S2 List of siRNAs used in this study

Human Gene	Accession Number	siRNA Sequence
GOLPH3	NM_022130	1# 5'-aaaugauguguaacccucgcggucc-3' 2 #5'-aauccagaugauauacagucauucc -3' 6 #5'-ggagaggaagguuacaacua-3'

		7# 5'-ucaaggaccgcgaggguua -3'
B4GALT5 (LCS)	NM_004776	1# 5'-gugaaauuggaauggauua-3' 2# 5'-gcuuaacaguggaacaauu-3' 4# 5'-ggaaagugaucgcaacuau-3' 5# 5'-gaaagacucccuuccauga-3'
SMS1	NM_147156 (from Capasso S. et al.)	1# 5'-cuacacucccaguaccugg-3' 2 #5'-cacacuauggccaaucagcaa-3'
Gb3S	NM_017436 (from Russo D. et al.)	1# 5'-agaaagggcagcucuauaauu-3' 2# 5'-ggacacggacuucauuguuuu-3' 3# 5'-ugaaagggcuuccgggugguu-3' 4# 5'-gcacucauguggaaguucguu-3'

Table S3 List of biotinylated peptides used in this study

Name	Peptide sequence
LCS-tail-WT	MRARRGLLRLPRRSLLA-Biot
LCS-tail-mut1	MRARRGLLAAAAASLLA-Biot
LCS-tail-mut2	AAAAAGLLRLPRRSLLA-Biot
GalT1-tail-wt	MRLREPLLSGSAAMPGA-Biot
Gb3S-tail	MSKPPDLLLRLLRGAPRQRVCT-Biot
GM3S-tail	MRRPSLLLKD-Biot
B4GALNT1-tail	MWLGRRA-Biot
GD3S-tail	MSPCGRARRQTSRGAMAVLAWKFPRTRLP-Biot
LC3S-tail	MRMLVSGRRVKKWQLIIQLF-Biot

Table S4 List of primers used in this study

Human	Forward Primer	Reverse Primer
GOLPH3	5'-cccaagcttatgacctcgctgacccagc-3'	5'- ggggtacccttggtgaacgccgcc-3'
GCS	5'-ttcgggttcgtcctcttc-3'	5'-gcttgctataaggctgtttgtc-3'
LCS	5'-caatcggtgctcaggtttatg-3'	5'-ggtttcactgtggttcaagtc-3'
GB3S	5'-gatccccacctctctgcaat-3'	5'-ttggacatggtatccccaga-3'
GM3S	5'-tggttattggaagcggagg-3'	5'-tctgaatatccctcaactggt-3'
FAPP2	5'-acatcaggatccgattgaga-3'	5'-atgcaccttctggatgtgtt-3'
CERT	5'-tgtggatcatgacagtgctc-3'	5'-atttcctggtttccctctgg-3'

SMS1	5'-gcatttcaactgttctccgaag-3'	5'-gatagacaagccacctccag-3'
HPRT1	5'-agcttgctggtgaaaaggac-3'	5'-gtcaagggcatatccaacaac-3'
Yeast	Forward Primer	Reverse Primer
MNN9	5'-atttggcttaccaaactatttggtttatcacatagaggaagagaaccatcggatcccgggttaattaa-3'	5'-attatctttcaataacgctatagcttctgtatgctttttgctcagttgcgaattcgagctcgtttaaac-3'
VPH1	5'-ataaagacatggaagtcgctgttgctagtgcaagctcttccgcttcaagccggatccccgggttaattaa-3'	5'-tatttaatgaagtacttaaatgtttcgctttttttaaaagtcctcaaaatgaattcgagctcgtttaaac-3'

Table S5 List of antibodies, lectins and toxins used in this study for immunofluorescence (IF), Western Blotting (WB), cryo-Electron Microscopy (cryo-EM), and FACS.

REAGENT or RESOURCE	SOURCE	IDENTIFIER
Polyclonal Rabbit GOLPH3	Abcam	Cat # ab98023 RRID: AB_10860828
Polyclonal Mouse GOLPH3	Abcam	Cat # ab69171 RRID:AB_2279272
Monoclonal Mouse GAPDH	Santa Cruz Biotechnology	Clone 6C5 Cat #sc-32233 RRID:AB_627679
Monoclonal Mouse HA-Tag	BioLegend/Covance	Clone 16B12 Cat #MMS-101P RRID:AB_10063630
Monoclonal Rabbit HA-Tag	Cell Signaling Technology	Clone C29F4 Cat #3724
Polyclonal Rabbit LAMPI	Abcam	Cat # ab24170 RRID: AB_775978
Polyclonal Rabbit B4GALT1	Sigma	Cat # HPA010807 RRID: AB_1078254
Polyclonal Sheep anti-human TGN46	BioRad/AbD-Serotec	Cat #AHP500G RRID:AB_323104
Monoclonal Mouse GM130	BD Biosciences	Clone 35 Cat # 610822 RRID: AB_398141
Monoclonal Mouse GFP	Abcam	Cat #ab6556

		RRID:AB_305564
Monoclonal Mouse GFP	Abcam	Cat #ab1218 RRID:AB_298911
Monoclonal Mouse anti-β Actin	Sigma	Clone AC-74 Cat #A2228 RRID:AB_476697
Monoclonal Mouse B4GALT5 (LCS)	Kind gift from Henrik Clausen, Denmark	Clone 6D4
Monoclonal Mouse B4GALT5 (LCS)	Kind gift from Henrik Clausen, Denmark	Clone 1E10
Polyclonal Rabbit B4GALT5 (LCS)	ThermoFisher Scientific	Cat PA5-25282 RRID:AB_2542782
Monoclonal Mouse Pentahistidine	ThermoFisher Scientific	Cat P21315 RRID:AB_1500376
Polyclonal Rabbit Phospho-Akt (Ser473)	Cell Signaling Technology	Cat #9271 RRID:AB_329825
Polyclonal Rabbit Phospho-Akt (Thr 308)	Abcam	Cat# ab66134 RRID:AB_1141017
Polyclonal Rabbit Akt	Cell Signaling Technology	RRID:AB_329827
p21 Waf1/Cip1 Rabbit monoclonal antibody	Cell Signaling Technology	Clone 12D1 Cat #2947 RRID:AB_823586
Polyclonal Rabbit p70S6K	Cell Signaling Technology	Clone 49D7 Cat#2708 RRID:AB_390722
Polyclonal Rabbit Phospho-p70S6K (Thr 389)	Cell Signaling Technology	Clone 108D2 Cat#9234 RRID:AB_2269803
Polyclonal Rabbit 4E-BP1 (53H11)	Cell Signaling Technology	Cat#9644 RRID:AB_2097841
Polyclonal Rabbit Phospho-4E-BP1 (Ser65)	Cell Signaling Technology	Clone 174A9 Cat#9456 RRID:AB_823413
Monoclonal Mouse VSV-G	Sigma	SAB4200695
ShTxB-CY3	Dr. Ludger Johannes	N/A
ChTxB-AlexaFluor 488	Invitrogen	Cat # C-22841
Anti-mouse, donkey Alexa Fluor 488	ThermoFisher Scientific	Cat #A-21202 RRID:AB_141607

Anti-mouse, donkey Alexa Fluor 568	ThermoFisher Scientific	Cat #A10037 RRID:AB_2534013
Anti-mouse, goat Alexa Fluor 633	ThermoFisher Scientific	Cat #A-21052 RRID:AB_141459
Anti-rabbit, donkey Alexa Fluor 488	ThermoFisher Scientific	Cat #A-21206 RRID:AB_141708
Anti-rabbit, donkey Alexa Fluor 568	ThermoFisher Scientific	Cat #A10042 RRID:AB_2534017
Anti-rabbit, goat Alexa Fluor 633	ThermoFisher Scientific	Cat #A-21070 RRID:AB_2535731
Anti-sheep, donkey Alexa Fluor 633	ThermoFisher Scientific	Cat #A-21100 RRID:AB_2535754
Anti-goat, donkey Alexa Fluor 568	ThermoFisher Scientific	Cat #A-11057 RRID:AB_142581
Anti-mouse, donkey DyLight 405	Jackson Laboratory	Cat # 712-475-153 RRID:AB_2340681
DyLight 549 Streptavidin	Jackson Laboratory	Cat # 016-500-084
Biotinylated Wheat Germ Agglutinin (WGA)	Vector Laboratories	Cat # B-1025
Biotinylated Aleuria aurantia Lectin (AAL)	Vector Laboratories	Cat #B-1395
Biotinylated Sambucus nigra Lectin (SNA)	Vector Laboratories	Cat #B-1305
Biotinylated Peanut Agglutinin (PNA)	Vector Laboratories	Cat #B-1075
Rhodamine labeled Ricinus communis Agglutinin I (RCA I)	Vector Laboratories	Cat #RL-1082
Rhodamine labeled Phaseolus vulgaris Leucoagglutinin (PHA-L)	Vector Laboratories	Cat # RL-1112

Table S6. Schematic representation of LCS-GFP_RUSH traffic assays

i)

Synchronization protocol					
Temperature (°C)	37 →	10 →	37 →	37 →	37
Biotin (40 µM)	- →	+ →	+ →	+ →	+
Cycloheximide (50 µg/mL)	+ →	+ →	+ →	+ →	+
Nocodazole (33 µM)	+ →	+ →	+ →	+ →	+
Time	3 hours →	60 min →	10 min →	20 min →	30 min

ii)

Synchronization protocol					
Temperature (°C)	40 →	10 →	37 →	37 →	37
Biotin (40 µM)	- →	+ →	+ →	+ →	+
Cycloheximide (50 µg/mL)	- →	+ →	+ →	+ →	+
Nocodazole (33 µM)	+ →	+ →	+ →	+ →	+
Time	3h →	60 min →	10 min →	20 min →	30 min

Table S7 List of bacterial and viral strains used in this study

REAGENT or RESOURCE	SOURCE	IDENTIFIER
Adenoviral - Type 5 (dE1/E3) of eGFP (Ad-GFP)	Vector Biolabs	Cat # 1060
Adenoviral - Type 5 (dE1/E3) of human GOLPH3 (Ad-h-GOLPH3)	Vector Biolabs	Cat # ADV-210166
Adenoviral - Type 5 (dE1/E3) of human B4GALT5 (Ad-h-B4GALT5-HA)	Vector Biolabs	Cat # ADV-201912
Temperature sensitive strain of vesicular stomatitis virus (ts045-VSV)	Kind gift from Bruno Goud, Institut Curie, France	N/A
E. coli (DH5α)	Thermo Fisher Scientific	Cat #18265017
E. coli (BL-21-DE3)	Thermo Fisher Scientific	Cat #C600003

List of chemicals used in this study

REAGENT or RESOURCE	SOURCE	IDENTIFIER
Paraformaldehyde 8%	Electron Microscopy Sciences	Cat #50-259-96
Glutaraldehyde 8%	Electron Microscopy Sciences	Cat #50-262-18
Methanol	JT Baker	Cat #9093
Cycloheximide	Sigma	Cat #01810
Protein A Sepharose CL-4B	GE Healthcare Life Sciences	Cat #17-0780-01
Anti-HA magnetic beads	ThermoFisher Scientific	Cat #88836
Bafilomycin A1 from Streptomyces griseus	Sigma	Cat # 88899-55-2
Insulin solution human	Sigma	Cat #11061-60-0

GDC-0941 (Pictilisib)	Selleckchem	Cat #1S1065
EasyTag™ EXPRESS35S Protein Labeling Mix, [35S]	Perkin Elmer	Cat #NEG772014MC
Sphingosine, [3-3H]-, D-erythro>97%	PerkinElmer	Cat #NET1072050UC
Silica-gel high performance-TLC (HPTLC) plates	Merck, Germany	Cat #1055830001
Bovine Serum Albumin Fatty acid free	Sigma	Cat #A8806
HA Peptide	Sigma	Cat #I2149
Biotin	Pierce	Cat #29129
Protein A gold 15 nm	Cell Microscopy Core, UMC Utrecht	N/A
Protein A gold 10 nm	Cell Microscopy Core, UMC Utrecht	N/A
Protein A gold 5 nm	Cell Microscopy Core, UMC Utrecht	N/A
TransIT-LT1	Mirus	Cat #MIR 2305
UltraPureTM Agarose	Invitrogen	Cat #16500-500
Lipofectamine LTX with PLUS	ThermoFisher Scientific	Cat #15338100
Oligofectamine	ThermoFisher Scientific	Cat #12252011
DMEM	Gibco/ ThermoFisher Scientific	Cat #41965
RPMI 1640	Gibco/ ThermoFisher Scientific	Cat #21875
FCS	Gibco/ ThermoFisher Scientific	Cat #10437036
DMEM w/o cysteine and methionine	Gibco/ ThermoFisher Scientific	Cat #21013
Sodium Pyruvate (100 nM)	Gibco/ ThermoFisher Scientific	Cat #11360-070
Yeast nitrogen base without amino acids	Difco Laboratories Inc	Cat # 291940
Casamino acids	Difco Laboratories Inc	Cat # 228830

Table S8 List of commercial assays and kits used in this study

REAGENT or RESOURCE	SOURCE	IDENTIFIER
RNA easy mini	Qiagen	Cat #74106
QuantiTect Reverse Transcription Kit	Qiagen	Cat #205311
SYBR™ Green PCR Master Mix	ThermoFisher Scientific	Cat #4309155

List of recombinant DNAs used in this study

REAGENT or RESOURCE	SOURCE	IDENTIFIER
GOLPH3 (untagged)-Human Golgi phosphoprotein 3	OriGene	Cat #SC112810
B4GALT1-HA	Kind gift from Hans Bakker, Germany	N/A
B4GALNT1-HA	GenScript	N/A
ST8SIA1-HA (or GD3S-HA)	GenScript	N/A
B3GNT5-HA	GenScript	N/A
B4GALT4-HA	GenScript	N/A
SMS1-HA	Kind gift from Giovanni D'Angelo	N/A
GCS-HA	Kind gift from Giovanni D'Angelo	N/A
Gb3S-HA	Kind gift from Antonella De Matteis	N/A
GM3S-HA	Kind gift from Antonella De Matteis	N/A
LCS-HA	This study	N/A
LCS-Myc	Kind gift from Antonella De Matteis	N/A
Str-KDEL_B4GALT5-SBP-EGFP (referred as LCS-GFP_RUSH)	This study. Gaelle Boncompain	N/A
Str-KDEL_GalTfl-SBP-EGFP (referred as B4GALT1-GFP_RUSH	Kind gift from Gaelle Boncompain (*Boncompain et al Nat Methods. 2012*)	N/A
Sucrose-Isomaltase (eferred as SI)	Kind gift from Stuart Kornfeld	N/A

B4GALT5_Met-7Ala_MutSI(TM) (referred as LCS-SI)	GenScript	N/A
B4GALT5_RARR_Mut-MutSI(TM) (referred as LCS-SI-RxR)	GenScript	N/A
B4GALT5_LXX(R/K)_Mut-SI(TM) (referred as LCS-SI-LxxR	GenScript	N/A
PH-Akt-GFP	Addgene	Cat #51465
ORP5-PH-GFP	Kind gift from Pietro De Camilli	N/A
PLCd-PH-GFP	Kind gift from Roman Polishchuk	N/A

Table S9 List of software used in this study

REAGENT or RESOURCE	SOURCE	IDENTIFIER
ImageJ	NIH	https://imagej.nih.gov/ij/
MetaMorph	Molecular Devices	https://www.moleculardevices.com/systems/metamorph-research-imaging
Prism	Graphpad	https://www.graphpad.com/scientific-software/prism/
Adobe Illustrator	Adobe	www.adobe.com/products/illustrator/free-trial-download.htm
Adobe Photoshop	Adobe	www.adobe.com/products/photoshop.html
Soft Imaging service (Electron microscope)	Olympus	www.olympus-sis.com/corp/2256.htm
iTEM	EMSIS GmbH	https://www.emsis.eu/products/software/item/
Volocity	Perkin Elmer	https://www.perkinelmer.com/lab-products-and-services/cellular-imaging/volocity-3d-visualization.html

Table S10 List of cell lines used in this study

REAGENT or RESOURCE	SOURCE	IDENTIFIER
HeLa-M	ATCC	RRID:CVCL_R965
Primary Human Fibroblasts	This study; Telethon Biobank ((http://www.telethon.it/en/funding-research/funded-projects/details/telethon-network-of-genetic-biobanks_0)	N/A
LNCaP	ATCC	RRID:CVCL_0395
DU-145	ATCC	RRID:CVCL_0105
HeLa-mCAT#8	Kind gift from Kentaro Hanada	N/A
TALEN UGCG-KO	Kind gift from Kentaro Hanada	N/A
TALEN LCS-KO	Kind gift from Kentaro Hanada	N/A

Table S11 List of yeast strains used in this study (see (*115*))

Strain	Genotype	Source
YPH499	*MAT a ura3-52 lys2-801 ade2-101 trp1-Δ63 his3-Δ200 leu2-Δ1*	1
YMO132	*YPH499ADE2::pRS402 MNN9-mCherry::natNT2*	2
YMI125	*YPH499 ADE2::pRS402 vps74::kanMX4 MNN9-mCherry::natNT2*	This study
YKK935	*YPH499 ADE2::pRS402 MNN9-sfGFP::HIS3MX6*	This study
YKK937	*YPH499 ADE2::pRS402 vps74::kanMX4 MNN9-sfGFP::HIS3MX6*	This study
YKK987	*YPH499 ADE2::pRS402 MNN9-sfGFP::HIS3MX6 VPH1-mCherry::natNT2*	This study
YKK989	*YPH499 ADE2::pRS402 vps74::kanMX4 MNN9-sfGFP::HIS3MX6 VPH1-mCherry::natNT2*	This study
YKK990	*YPH499 ADE2::pRS402 VPH1-sfGFP::HIS3MX6*	This study
YKK992	*YPH499 ADE2::pRS402 vps74::kanMX4 VPH1-sfGFP::HIS3MX6*	This study